Development of a multi-pixel photon sensor with single-photon sensitivity

Motohiro Suyama

DOCTOR OF PHILOSOPHY

Department of Particle and Nuclear Physics,
School of Mathematical and Physical Science,
The Graduate University for Advanced Studies

2002

Abstract

In particle physics experiments, photon sensors play key roles in detecting and measuring particle's kinetic parameters. Photons produced by a particle in a detector possess essential information on the particle's properties. They are utilized for particle identification in Cherenkov counters and TOF counters, for particle tracking in scintillating fiber detectors and for energy measurement in calorimeters. An interesting and attractive photon sensor is a hybrid photo-detector (HPD) equipped with a multi-pixel avalanche diode. An HPD can be realized based on vacuum-tube technology and the rapidly evolving semiconductor technology. The latter is the key element for multi-pixel readout with single-photon sensitivity.

We have investigated various types of avalanche diodes (AD) appropriate for electron multiplication, and have successfully developed an HPD equipped with the most practical AD. The developed HPD has an effective area of 16×16 mm^2 with 8×8 pixels of 2×2 mm^2 each. The gain is 5×10^4, sufficiently high to detect single photons with a timing resolution better than 100 ps. Photoelectrons from 1 to 5 can be clearly identified in a pulse-height spectrum as distinct peaks, thanks to the low noise characteristics of the HPD. In addition, it has been proved that the HPD can be operated with good performance in a magnetic field of up to 1.5 T. A superb feature of this HPD as a particle tracker has been demonstrated by a measurement of muon tracks in cosmic-rays with a detector system consisting of a bundle of scintillating fibers and an HPD.

In this way, the developed HPD has successfully functioned as a multi-pixel photon sensor. This is the first HPD having all desirable features, such as high granularity, single-photon sensitivity, fast timing capability and operability under high magnetic fields, which are essential requirements in applications for high-energy physics experiments.

Contents

Chapter 1

Introduction

Particle physics aims to reveal the fundamental constituents of matter and their interactions, and ultimately to understand the creation of universe. The result of experimental and theoretical efforts over several decades gave birth to the standard model, which explains almost all of the particle phenomena observed so far. However, it is a common understanding that unknown physics laws rule at deeper levels beyond the standard model.

The next-generation experiments being planned in quest for such laws need better particle detector systems that can operate at accelerators of significantly higher luminosity or higher energies. The modern detectors always rely heavily on the state-of-the-art technologies at that time. In that sense, it is not an exaggeration to say that any break-through in particle physics comes from a new technology being applied to a new class of detectors. This work was focused on the development of a new hybrid photo-detector (HPD), the most promising photon sensor to be used in new particle physics experiments. An advanced technology for photon sensing will no doubt also contribute to many other fields of science and engineering.

1.1 Particle detection

We now know that high-energy particle reactions result from collisions of elementary particles. For example, proton-proton collisions are ascribed to two-body scatterings among the constituents of protons, which are quarks, antiquarks and gluons. High-energy electron-positron collisions produce copious quark and antiquark pairs. In contrast to the simplicity of such elementary processes, what one actually observes are productions of a large number of particles. This is primarily due to the nature of quarks and, in part, to the decays of heavy particles. Particle physics experiments aim to understand elementary processes through measurements of the produced

particles. The key issue is the experimental capabilities in measuring the charge, momentum and energy, as well as the direction and to identify the type of each particle in the presence of many of them.

In passing through a detector material, charged particles, such as protons and charged pions, ionize and excite atoms and molecules. The resulting free electrons and photons are the source of information concerning these particles. Under specific conditions, the detector material responds to the passage of a charged particle by emitting radiation: Cherenkov radiation or transition radiation. In the case of neutral particles, such as neutrons and gamma-rays, secondary charged particles resulting from nuclear or atomic interactions of the parent particles are detected by going though the same processes in the detector.

One of the widely used detectors for charged particles is a scintillation counter, particularly a combination of plastic scintillators and photon sensors. Facing an increasingly harsh experimental environment where the counting rate is high and the number of produced particles per reaction is large, many layers of scintillating fiber sheets have started to play an important role as a fast particle tracker [1]. For particle energy and position measurements in a similar situation, a sampling calorimeter made of a sandwich of metal plates and plastic scintillator plates is a choice in many cases. Scintillation photons from individual scintillator plates are wavelength-shifted by special fibers embedded in the plates, and collected through optical fibers to photon sensors [2]. For the purpose of maximizing the information available for incident particles, and also for engineering reasons, recent work has been focused on the development of such calorimeters with a fiber readout. In these advanced detectors, the number of readout channels becomes huge, with each receiving only a few to several photons, because of the fine segmentation and significant photon attenuation. Accordingly, highly sensitive photon sensors with fine granularity are required.

Another important element of the experimental apparatus is the Cherenkov detector. Cherenkov light is emitted to an angle θ (Cherenkov angle) with respect to the particle direction when a charged particle goes through a transparent material at a velocity v larger than the velocity of light in the medium,

$$v > \frac{c}{n}, \tag{1.1}$$

$$\cos\theta = \frac{1}{n \times (v/c)}, \tag{1.2}$$

where c is the velocity of light in a vacuum and n is the refractive index of the radiator. The number of photons (N) is given by a

$$\frac{dN}{d\lambda} = \frac{2 \times \pi \times \alpha}{\lambda^2} \times L \times \sin^2\theta, \tag{1.3}$$

where λ [nm] is the wavelength of the Cherenkov photon, α is the fine-structure constant and L is

the length of the material. In practical cases, this is a small number, and photon sensors with single-photon sensitivity are necessary. This radiation is used for particle identification in three ways: in combination with a momentum measurement as a threshold counter, a differential counter and a ring-imaging counter in the order of increasing sophistication. The third case extracts the maximum information by measuring the position of each Cherenkov photon. There are proposals involving large-scale applications, such as [3]. In this case, photon sensors with fine segmentation are required for imaging. In addition, a new type of counter, a Time-Of-Propagation (TOP) counter, is under development [4]. The TOP counter measures both the position and timing of Cherenkov photons that propagate along a long radiator bar with resolutions of 1 mm and 100 ps, respectively, in a magnetic field higher than 1 T. In addition to fine segmentation and high sensitivity, therefore, the photon sensor is required to provide a very fast response and to be operated in a very high magnetic field. Such sensors are yet to be developed.

1.2 Photon sensors in particle physics experiments

As mentioned in the previous section, a variety of information on incident particles is carried by photons emitted in the detector material. Photon sensors equipped with such detectors are thus one of the key elements of experiments. They detect photons by converting them to electrons, which are then multiplied in number to generate a sufficiently large electric signal for a measurement.

A photo-ionization detector is a photon sensor using a photosensitive gas, such as tri-ethyl-amine (TEA) and tetrakisdi-methl-amino-ethylene (TMAE), which converts UV photons to photoelectrons in a conversion (C) gap, as shown in Fig. 1.1 [5]. The number of photoelectrons is multiplied in a pre-amplification (PA) gap, and the multiplied electrons are transferred to a multi-wire proportional counter (MWPC) though a transfer (T) gap. The number of photoelectrons is further multiplied by the MWPC. The total gain is as high as 10^6, sufficient to detect single photons. In addition, the photo-ionization detector has a position sensitivity owing to the MWPC. Because of the nature of the gaseous detector, a large photosensitive area can be easily covered at a reasonable cost. Furthermore, it can be operated in high magnetic field. These features enable the detector to be applied to a ring imaging Cherenkov counter (RICH). Recently, a gas electron multiplier (GEM) has been studied extensively for the pre-amplification of photoelectrons in conjunction with a photo-ionization detector [6]. The GEM is a thin insulating polymer mesh with electrodes on both the input and the output surfaces. With an applied voltage of 200 V between the electrodes, an electric field of 40 kV/cm is created in a channel for the pre-amplification of photoelectrons. The GEM realizes an additional gain as well as a reduction of photon feedback from the MWPC to the conversion gap. One shortcoming of a photo-ionization detector is its poor, or no, sensitivity in the

wavelength range of visible light due to the nature of the photosensitive gas.

A photomultiplier tube (PMT) [7] is the most popular photon sensor made of a vacuum tube containing a photocathode, a dynode chain and an anode. The configuration of the typical head-on type PMT is shown in Fig. 1.2. The photocathode is a thin layer of alkali materials, such as potassium or cesium. It is fabricated on the vacuum side of the input faceplate, and emits electrons to a vacuum in response to the incidence of photons. By applying a voltage of about 1 kV to the PMT, electrons from the photocathode are directed to, and amplified, by a factor of 10^7 through an eight-to-ten stage dynode chain. As a result, a single photon can be efficiently detected with a response time on the order of one nano-second. PMTs thus offer a single-photon detection capability with a high gain, a fast response, and a large effective area. They have been an essential part of basic particle detectors, such as scintillation counters and Cherenkov counters. It is generally difficult to have a finely segmented structure, or to operate in a strong magnetic field.

An image intensifier tube (IIT) is another type of vacuum tube consisting of a photocathode and a phosphor screen. Photoelectrons from the photocathode are accelerated and focused onto a phosphor screen by an electrostatic focusing lens formed inside the vacuum. Since photoelectrons are accelerated up to 20 to 30 keV, each photoelectron generates a few tens of photons on the phosphor screen. Thus, an intensified image can be observed at the screen of the IIT. One example using IIT in a particle physics experiment is shown in Fig. 1.3 [1], where two stages of IITs are connected in a cascade. The first stage intensifies, but demagnifies, the input images by a factor of 4 in its size. The second stage has a micro-channel plate (MCP), which further intensifies the image, where the MCP is a thin glass plate with plenty of hollows to multiply the electrons by a factor of a thousand while preserving their position. Finally, a CCD camera converts an output light image to electrical signals in finely segmented pixels. This system is used for a scintillating fiber readout with high granularity. Since the readout frequency of this kind of system is limited to approximately 30 ms by the CCD camera, it is not suitable for high-rate applications.

A photodiode (PD) [8] is a photosensitive semiconductor device, usually made of silicon. As shown in Fig. 1.4, a p-type impurity, such as boron, is diffused into an n-type substrate to form a pn-junction. With a reverse bias voltage is applied to the pn-junction, the substrate becomes fully depleted. This reduces both the capacitance of the diode and the transit time of the carriers. When incident photons having energy greater than the band-gap energy are absorbed, electron-hole pairs are generated and drift in a depletion region to induce an output current. The nice features of the PD are its excellent quantum efficiency (QE: the conversion efficiency from photons to electrons) of more than 90% and a fast response on the order of one nano-second. However, since the thickness is 0.5 mm at most, the response time is limited by its capacitance if the effective area is large. A typical application is to measure photons generated in a scintillating crystal calorimeter where a large number of photons are available.

An avalanche photodiode (APD) [8] is also used as a sensor based on the pn-junction of a semiconductor, as shown in Fig. 1.5. It differs from PD in the impurity concentration around the pn-junction, which is carefully adjusted to generate a sufficiently high electric field for an avalanche multiplication of carriers. In the case of Si, since the ionization coefficient of the electron is much larger than that of holes, electrons generated in the p-type region are used for avalanche multiplication. APD thus adds an avalanche gain of 50 to 100 to the high QE and a fast response time of the PD, although it is still not high enough for single-photon detection.

A visible light photon counter (VLPC) [9] is another type of semiconductor photon sensor having an avalanche gain. As shown in Fig. 1.6 (a) [9], the VLPC consists of an infrared-active layer (IRL) made of arsenic-doped silicon, an undoped blocking layer (BL) and a transparent contact (TC) layer. If a bias voltage is applied to the VLPC under operating temperature of 6 – 10 K, an electric field is generated, as shown in Fig. 1.6 (b), and an avalanche multiplication of photoelectrons would appear in the high-electric field region. Since a highly doped IRL acts as an intrinsic semiconductor with a band gap energy equal to the impurity ionization energy (50 mV) at a sufficiently low temperature, impurity-band avalanche multiplication occurs with a much lower electric field than the APD. The gain with an applied voltage of 7 V is on the order of 10^4, and is sufficiently high to detect single photons. As many as five photoelectrons can be discriminated thanks to a local saturation of the multiplication. The QE is typically 60%. VLPC is becoming more popular in particle physics experiments for a scintillating fiber readout [10]. The requirement for operation at a quite low temperature of 6 to 10 K and its relatively high dark count rate even under the condition make its wider application difficult.

A hybrid photo-detector (HPD) [11] is a vacuum tube, that incorporates a photocathode and a semiconductor device as a photoelectron detector. Its sectional view is schematically shown in Fig. 1.7. A photocathode is the same as that of the photomultiplier tube, and the diode is similar to a PD with some modifications made to deal with electron irradiation. This is called HPD, because of the combination of vacuum tube technology and semiconductor technology. Electrons emitted from the photocathode are accelerated and focused onto the diode by an electric field in the vacuum. When accelerated electrons enter the diode, they lose their kinetic energy and generate thousands of electron-hole pairs. This is called the electron-bombarded gain (m_{EB}). Since an electron-hole pair is generated on average by the energy loss of every 3.6 eV in Si, the gain is 2800 at an electron energy of 10 keV in an ideal condition. This gain is much larger than that of an APD. When compared to a PMT, this gain plays a role similar to the first dynode, but is two orders of magnitude larger. Because of this high gain at the first stage, the signal-to-noise ratio after electron multiplication is so excellent that very clean photon counting is possible. To detect single photons, a gain on the order of 1,000 is not sufficient when a fast amplifier with an inherently large noise is used for the readout. In this case, an avalanche diode (AD) can be used instead of a diode [12].

Then, an additional gain of 50 to 100 can realize a total gain as high as 1×10^5.

1.3 Goal of this study

Among the various photon sensors used in particle physics experiments, an HPD equipped with a multi-pixel AD has high potential to be used in future experiments. A combination of m_{EB} and the avalanche gain leads to single-photon detection with a fast response time. A proximity focused structure, where the photocathode and the AD are located close to each other, makes it possible to operate in a high magnetic field. Fine segmentation is accomplished with an AD having a multi-pixel configuration. Accordingly, the HPD covers the weak points of current photon sensors. For example, most PMTs can not be used in a high magnetic field, and have some limitations in segmentation for multi-pixel operation. The general semiconductor photo-sensor can not detect a single photon due to the small gain. Therefore, the HPD can be widely used in particle physics experiments, such as a scintillating fiber readout and Cherenkov counters.

However, HPD with a multi-pixel AD has not yet been available, lacking a suitable multi-pixel AD for electron multiplication. The goal of this study is to develop a prototype, and evaluate the capabilities of such an HPD. In the first step, the AD is investigated to develop the most suitable one for electron multiplication. In the second step, the AD is assembled in a vacuum tube to realize the HPD. Finally, performance of the newly developed HPD is evaluated in detail.

1.4 Outline of the following chapters

In this report, the development and evaluation of a proximity focused HPD with a multi-pixel AD is described. In chapter 2, the history and current developments of HPDs are reviewed. In chapter 3, a conceptual design and operation of the HPD to be developed is discussed. In chapter 4, the multi-pixel AD, which is one of the most important components, is discussed in detail to realize a suitable structure for electron multiplication. In chapter 5, issues in designing and manufacturing process of the HPD are described. The developed HPD is evaluated in detail, and the results are described in chapter 6, where the performance, such as the gain, time response, pulse-height spectrum for a single photon, uniformity and cross talk are shown. The result of a practical test to observe cosmic-rays is described as well. In chapter 7, the study is concluded, and the prospects for the future are discussed.

[REFERENCES]

[1] A.Suzuki et al, “Design, Construction, and Operation of SciFi Tracking Detector for K2K Experiment”, Nucl. Instr. and Meth. A453, pp.165-176, 2001

[2] E. Mazzoni, “The hadronic calorimeter of the ATLAS experiment at the LHC”, Nucl. Instr. and Meth. A461, pp. 351-354, 2001

[3] The LHCb Collaboration, “LHCb Technical Proposal”, CERN/LHCC 98-4, LHCC/P4, 1998

[4] M. Akatsu et al., “Time-of-Propagation Cherenkov counter for particle identification”, Nucl. Instr. and Meth. A440, pp.124-135, 2000

[5] J. Seguinot et al., “Imaging Cherenkov detector: Photo-ionization of tri-ethyl-amine”, Nucl. Instr. and Meth. 173, pp.283-298, 1980

[6] F. Sauli, “GEM: A new concept for electron amplification in gas detectors”, Nucl. Instr. and Meth. A386, pp.531-534, 1997

[7] Catalogue of Hamamatsu Photonics K.K., Electron Tube Center, “Photomultiplier Tubes“, April 2000

[8] Catalogue of Hamamatsu Photonics K.K., Solid State Division, “Si Photodiode”, January 2002

[9] M. D. Petroff et al., “Detection of individual 0.4-28 μm wavelength photons via impurity-impact ionization in a solid-state photomultiplier”, Appl. Phys. Lett. 51 (6), pp.406-408, 1987

[10] D. Adams et al., “First large sample study of visible light photon counters (VLPC’s)”, Nucl. Phys. B 44, pp.340-348, 1995

[11] R. DeSalvo, “Why people like the Hybrid PhotoDiode”, Nucl. Insr. and Meth. A387, pp.92-96, 1997

[12] M. Suyama et al., “A Compact Hybrid Photodetector”, IEEE Trans. Nucl. Sci. NS-44, No.3, pp.985-989, 1997

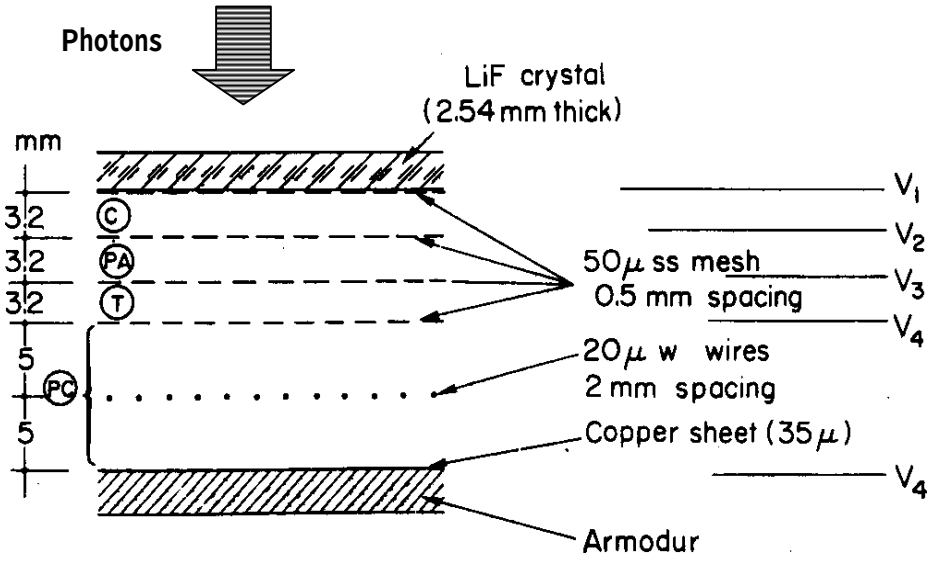

Fig. 1.1: Schematic drawing of a photo-ionization detector [5].

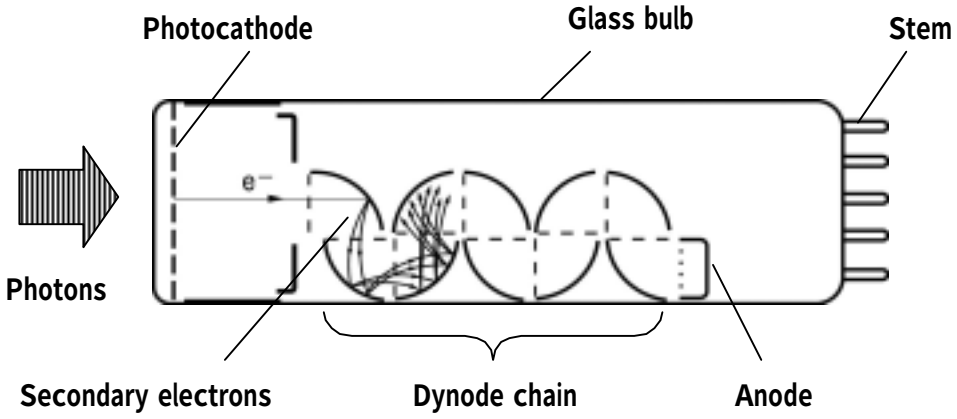

Fig. 1.2: Sectional view of a photomultiplier tube (PMT) [7].

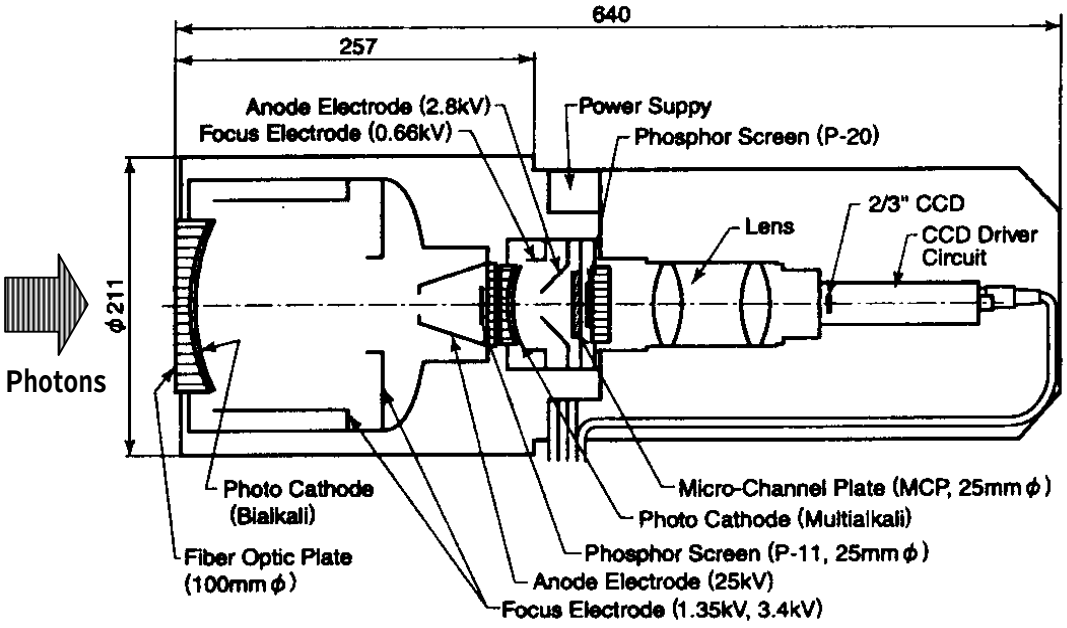

Fig. 1.3: Schematic drawing of a detection system using two IITs and a CCD camera [1].

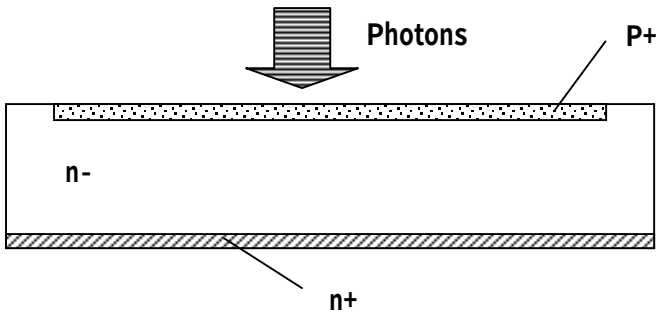

Fig. 1.4: Sectional view of a photodiode (PD).

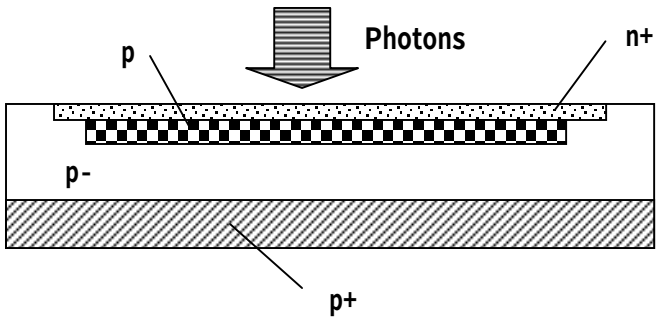

Fig. 1.5: Sectional view of an avalanche photodiode (APD).

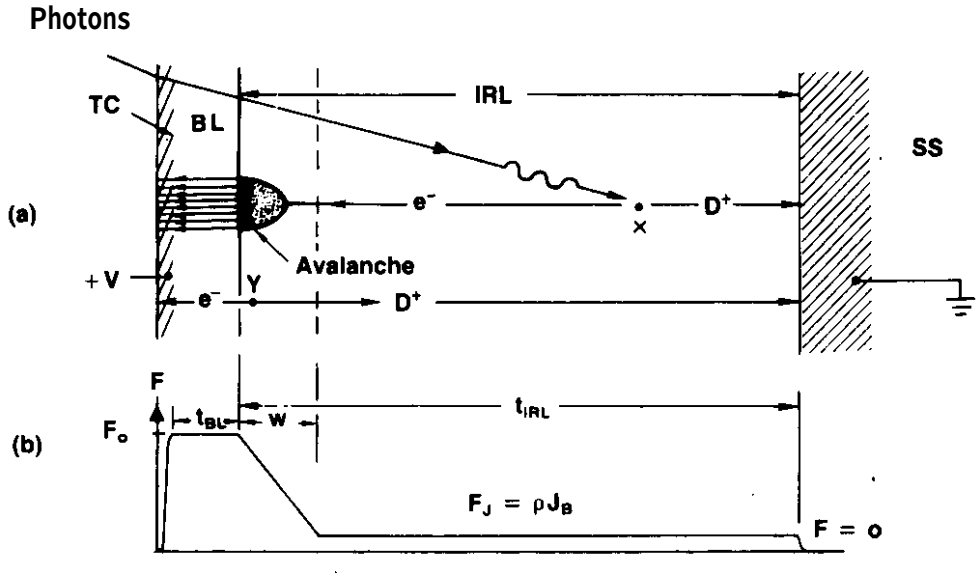

Fig. 1.6: Layer configuration (a) and electric field profile (b) of a VLPC [9].

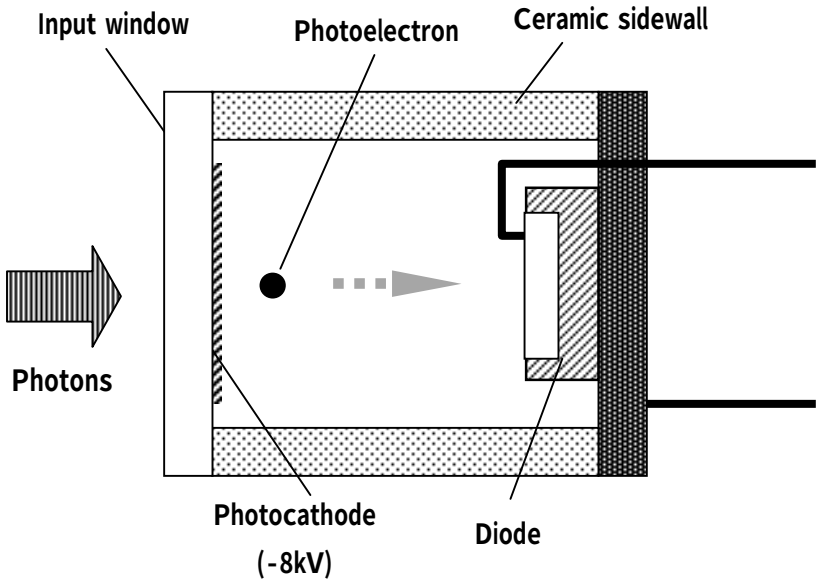

Fig. 1.7: Sectional view of a hybrid photo-detector (HPD).

Chapter 2

Current status of hybrid photo-detectors

The development of hybrid photo-detectors (HPD) started in the 1960's immediately after the advent of semiconductor particle detectors. The principal aim was to detect photons in the UV or visible range more accurately than possible with conventional photomultiplier tubes. In 1987, R. DeSalvo proposed an HPD for particle physics experiments. Since then, many attempts have been made toward the development of HPDs. The history of HPD development as well as recent work is reviewed.

2.1 Brief history of hybrid photo-detectors

In the early 1960's, it was found that semiconductor devices are sensitive to ionizing particles. These particles deposit their kinetic energies in devices by ionization, while generating electron-hole pairs. The yield and position of the generated electron-hole pairs are the source of important information on the incident particles.

When the incident particles are low-energy electrons, most of their kinetic energies are deposited in the semiconductor device, and electron-hole pairs are generated corresponding to the energy of the incident electrons. This is effectively a multiplication process of electrons, where the ratio of the generated electrons and the incident electrons is called the electron-bombarded gain (m_{EB}). Using this gain mechanism, F. A. White and J. C. Sheffield proposed a triode-type current-amplifier tube in 1962 [1], and described the possibility of a photon sensor made from the combination of a photocathode and a semiconductor device. This type of photon sensor is called a "Hybrid photo-detector (HPD)" these days.

The first HPD was realized by R. Kalibjian in 1965 [2]. The structure of the tube [3] is shown in Fig. 2.1. A high voltage of -5 kV was applied to a photocathode of 50 mm in diameter. Electrons

from the photocathode were accelerated and focused onto a semiconductor device of 9.5 mm in diameter by a built-in electrostatically focusing lens. The semiconductor device was a Si diode with a pn junction. The gain was 1200. The main objective of the HPD in those days was a large dynamic-range operation using multiplication in the Si diode. To achieve this, a reverse bias voltage of 500 V or higher was applied to the diode, and an output current larger then 1 A was obtained. This kind of operation was impossible for PMTs, because of the space-charge effect in a vacuum. Since the quality of the diode was poor and the leakage current was on the order of 1 μA in those days, research was not focused on the detection of a single photon [4][5]. Among other studies carried out in the early days, P. Chevalier focused on single-photon detection with an HPD in 1967 [6]. The output signal corresponding to 1 to 3 electrons from the photocathode was clearly distinguished. The pulse-height resolution (FWHM) for single electrons was 30% at quite high photocathode voltages of -20 kV to -40 kV.

Four years later, an HPD with a multi-pixel diode was reported by E. A. Beaver and C. E. McIlwain in 1971 [7] and 1972 [8]. The Si diode had 38 liner arrays of 8×0.1 mm^2. To make imaging as well as to apply a high voltage, the HPD [9] had a unique structure, as shown in Fig. 2.2, of which the sidewall was a stacked structure of 11 layers of glass and disk-like electrodes to produce a constant gradient potential throughout the vacuum. A high voltage of -15 kV to -30 kV was applied to the photocathode, and the solenoid coil magnetically focused electrons from the photocathode onto the Si diode. The gain was 7,000 at a photocathode voltage of -30 kV. The peak corresponding to a single-photon was clearly observed in the pulse-height spectrum [7]. The resolution for single electrons was 16%. This kind of HPD, which had a stacked-structured sidewall and a focusing magnet, was called “Digicon”. A Digicon with fine segmentation and self-scanned readout was reported by R. G. Tull et al. in 1975 [9]. The electron-multiplication-detection part was a monolithic self-scanned diode with linear pixels of 1024, and the output signal from each pixel was sequentially read out. Since the readout noise was 300 e rms, a single photon could be detected. Adding a cooling function to the tube, the Digicon was applied for high-resolution astronomical spectroscopy [10]. In spite of its excellent performance, the Digicon has not been widely used, probably because the system was complicated and bulky due to the solenoid coil and the extremely high photocathode voltage.

The potential of HPD was not seriously considered for nearly ten years, but R. DeSalvo reinvented the HPD in 1987 [11] to use as a photon sensor for particle physics experiments. L. K. Greest and K. W. Stoop developed an electrostatically focused HPD using modern image intensifier technology in 1991 [12], shown in Fig. 2.3. Electrons from a multi-alkali photocathode were electrostatically focused onto the Si diode of 1 or 2 mm in diameter. The gain was 3300 at the photocathode voltage of -15 kV. Both the rise time and the fall time were 2 ns. A current linearity up to 20 mA was confirmed. R. DeSalvo et al. reported the results of a detailed evaluation,

including the pulse-height spectrum for a few electrons from the photocathode [13]. The target application was to measure the photon yields from bundles of scintillating fibers. The HPD met the requirements, showing high speed, good linearity, a wide dynamic-range and good stability. Since the bleeder networks commonly used for PMTs were not necessary, the power consumption was low enough to read out millions of scintillating fibers. The other feature of the HPD is a good signal-to-noise ratio in electron multiplication. C. Datema et al. obtained a clean pulse-height spectrum with an electrostatically focused HPD in 1997 [14], as shown in Fig. 2.4. Johansen and Johnson also reported an electrostatically focused HPD developed for particle physics experiments in 1993 [15], where the structures as well as the fabrication method of the HPD were described in detail. M. Suyama et al. developed a small-sized HPD [16], where an electrostatic focusing lens was applied. The small-seize, single-pixel HPDs could be packed densely in a small space to measure many signals in parallel.

Recent developments of HPDs following the history described above are primarily categorized in four topics. These are described in the next section.

An electron-bombarded gain mechanism was also applied to imaging, for example, for a low light-level imaging surveillance camera. A CCD was used for electron-hole pair generation and their detection, but electrons were irradiated from the backside. This type of detector was reported by J. B. Barton in 1975 [17], and is called an “Electron-bombarded CCD (EB-CCD)”. Commonly used front-side CCDs for photon detection couldn’t be used, because the delicate metal-oxide-semiconductor (MOS) layer was seriously damaged by electron irradiation [18]. The CCD was thinned from the backside down to 10 to 15 μm to preserve the spatial resolution and efficiency of transferring secondary electrons to a potential well on the front side. The gain of such an EB-CCD was 200 at a photocathode voltage of -12 kV [18]. An electrostatic focusing lens was used for the tube. The gain was improved to 1700 at a photocathode voltage of -15 kV in 1992 [19].

G. Williams et al. reported on a proximity focused EB-CCD with a high quantum-efficiency GaAs or GaAsP photocathode in 1995 [20][21]. Also, M. Suyama et al. reported on an EB-CCD with a similar configuration in 1997 [22]. The single-photon imaging capability of the EB-CCD was confirmed by the latter work when cooled down to -30 degrees centigrade. The output images of the resolution chart are shown in Fig. 2.5 [22]. The bright spots shown in Fig. 2.5 (a) were not from noise, but from the input single photon, because the number of bright spots increased with the exposure time, and an image of the chart was clearly observed at an exposure time of 20 s, as shown in Fig. 2.5 (b). T. Maruno et al. incorporated a frame-transfer CCD to the EB-CCD for TV rate operation [23], where the attained gain was 1000. A high quantum-efficiency GaAs or GaAsP photocathode was introduced to the EB-CCD by M. Muramatsu et al. [24]. V. W. Aebi et al. used a frame-transfer CCD with an anti-blooming drain [25]. The anti-blooming capability is desired for a

low light-level imaging surveillance camera, because some bright objects, such as a light bulb, are likely to be located in a dark field.

2.2 Recent developments

2.2.1 Hybrid photo-detector with an avalanche diode

An HPD equipped with an avalanche diode (AD) was studied, because the gain is one to two orders of magnitude higher than with a diode, and is especially useful in single-photon detection at a high speed on the order of one nano-second. The HPD has a potential to replace the PMT in terms of gain.

In 1977, A. P. Choisser suggested the merits of the AD over a diode in vacuum, and reported on the stability of an avalanche diode against electron irradiation [26]. In 1993, P. Cushman evaluated a proximity focused HPD with an AD [27]. In this case, a single-pixel AD was a specially processed beveled-edge type, and its effective diameter was 16 mm. An avalanche gain of up to 1000 led to a total gain of 1×10^6. Furthermore, the gain uniformity was excellent. In spite of its high performance, this kind of HPD has not been widely applied, maybe because of the cost and yield of the specially manufactured beveled-edge AD. The mass production of a multi-pixel AD with such a structure seems to be a distant possibility.

In 1997, M. Suyama et al. reported on a practical HPD with a single-pixel AD [16]. The effective diameter of the multi-alkali photocathode was 8 mm, while the AD was 3 mm in diameter. An electrostatically focused lens was used for demagnification. The gain was 65,000 with a photocathode voltage of -8 kV and an AD voltage of 150 V. The rise time was 1.2 ns, and the fall time was 13 ns. The fall time was determined by a capacitance of 120 pF for the AD. N. Kanaya made a detailed evaluation for this HPD [28]. An HPD with the single-pixel AD has been successfully developed in this way and, as a result, is now commercially available [29].

An HPD equipped with an AD is especially useful in single-photon detection at high speed on the order of one nano-second. A gamma-ray telescope is one of its applications, as reported by R. Mirzoyan et al. in 1997 [30] and 2000 [31]. A new type of Cherenkov ring-imaging detector, time-of-propagation (TOP) counter [32], requires a time resolution of better than 100 ps in a high magnetic field of 1.5 T. S. Matsui et al. concluded from their experiments that an HPD with an AD has a potential to be used for a TOP counter [33].

2.2.2 Hybrid photo-detector with a high quantum-efficiency photocathode

The photocathode is the key to a photo-detector, since its photon-to-electron conversion efficiency (quantum efficiency, QE) determines the over-all performance. Accordingly, photocathode, itself, has also been studied extensively.

Aiming for a high QE, single-crystal semiconductor-based photocathodes have been developed. A GaAs photocathode, of which the QE is higher than 30% from the red to the near infrared region, was extensively developed in the field of low light-level imaging [34]. P. Cushman et al. reported on a proximity focused HPD with this type of photocathode [27] in 1993. The QE was 34% at around 550 nm and 18% at 800 nm, though it had no sensitivity below 480 nm. M. Suyama et al. also reported on an HPD with a GaAs photocathode in 1998 [35].

A GaAsP photocathode, of which the QE was highest in the visible region, was originally developed in the field of low light-level imaging as well [36]; however, it was not broadly used due to the limited efficiency in the near-infrared region. For surveillance, the sensitivity in the near-infrared region is very important. S. M. Bradbury et al. reported on an electrostatically focused HPD with a GaAsP photocathode [30][31]. The quantum efficiency was close to 50% from 450 nm to 600 nm. The spectral response of the GaAsP photocathode is best suited for some scintillators commonly used in particle physics experiments.

2.2.3 Electrostatically focused hybrid photo-detector

Modern particle physics experiments require large photosensitive areas with high granularity and a single-photon detection capability. One example is ring-imaging Cherenkov (RICH) counters for the LHCb experiment at CERN [37]. In this case, the electrostatically focused HPD is suitable, having a large photocathode, demagnified electron optics and a multi-pixel Si device connected to the front-end electronics. A large photocathode is preferable from the viewpoint of cost per area, because the cost of the photocathode is generally independent of its size. Actually, the cost per area of the photocathode is cheaper than a semiconductor detector for a large effective area. A small Si device is preferable from the viewpoint of cost as well as performance, such as the leakage current and response time. This is the reason that an electrostatically focused HPD is being investigated. Note that the efficiency of the demagnified electron optics is 100%, which is much higher than that of an optical lens or a tapered fiber-optic plate (FOP). The maximum efficiency of the optical means is proportional to the inverse square of the demagnification factor. Two types of electrostatically focused HPD are under development for LHCb. They are a pixel HPD [38] and a pad HPD [39].

The pixel HPD has an effective diameter of 75 mm, covering 82% of the overall diameter of 83

mm. Because it has an electrostatic focusing configuration with a demagnification factor of 5, the pixel size of 0.5×0.5 mm^2 corresponds to 2.5×2.5 mm^2 on the photocathode. Each pixel is bump-bonded to the front-end electronics. A full-scale prototype was manufactured and was confirmed to meet the experimental requirements.

The pad HPD has a fountain-focusing electron optics, as shown in Fig. 2.6 [39]. Electrons emitted from an effective diameter of 114 mm are just demagnified by a factor of 2.5 onto a Si sensor of 50 mm in diameter, while still preserving the spatial information. This was accomplished by introducing bleeder electrodes. The size of the individual pads is 1×1 mm^2 on the sensor, and is thus equivalent to 2.5×2.5 mm^2 on the photocathode. 2048 pads are read out by specially developed multiplexed analogue electronics incorporated in the vacuum.

2.2.4 Proximity focused hybrid photo-detector

One of the big advantages of a proximity focused HPD is operation in a high magnetic field. This HPD is composed of a closely placed photocathode and a Si device, and the direction of the electric field is parallel to the tube axis when a high voltage is applied. Then, the electron trajectory is not disturbed by a magnetic field, if the magnetic field is parallel to the tube axis. In current collider experiments, there are strong demands to use photon sensors in high magnetic fields. In this environment, few photon sensors, except for a proximity focused HPD, can detect a single photon efficiently.

A proximity focused HPD was reported by S. Basa et al. in 1993 to be used in a high magnetic field [40]. The gap between the photocathode and the semiconductor device was 1.8 mm. The gain was 1800 at a photocathode voltage of -10 kV, and the pulse-height spectrum for single photons was obtained. The capability of the tube in a magnetic field up to 4 T was confirmed by H. Arnaudon et al. [41]. The diode at that time had a single pixel, and was a precursor of a multi-pixel HPD.

Recently, a multi-pixel HPD was developed and tested for an application to a hadron calorimeter of a CMS experiment at LHC [42][43]. The structure of the HPD [44] is shown in Fig. 2.7. Two types of pixel arrangement, 19 pixels and 73 pixels, were developed. The input window is made of a fiber-optic plate (FOP) to directly connect fiber bundles to the photocathode. The photocathode is a multi-alkali type. The gap between the photocathode and the multi-pixel diode is 3.3 mm. By applying 12 kV between the gap, a gain of 3000 is obtained. A multi-pixel diode is bonded to a ceramic stem through bumps. Due to a reduction in the thickness of the diode from 0.3 mm to 0.2 mm, a sufficiently fast response of less than 20 ns in full width is obtained. The HPD will be used in a magnetic field of 4 T.

[REFERENCES]

[1] F. A. White and J. C. Sheffield, “Reversed-Biased P-N Junctions in Electron Tubes”, Proc. IRE, Vol.50, No.6, pp.1523-1524, 1962

[2] R. Kalibjian, “A phototube using a diode as a multiplier element”, IEEE Trans. Nucl. Sci. NS-12, No.4, pp.367-369, 1965

[3] R. Kalibjian, “A phototube using a semiconductor diode as the multiplier element”, IEEE Trans. Nucl. Sci. NS-13, No.3, pp.54-62, 1966

[4] J. Fertin et al., “Reverse epitaxial silicon diode for hybrid photomultiplier tube”, IEEE Trans. Nucl. Sci. NS-15, pp.179-189, 1968

[5] J. M. Abraham et al., “Application of Solid-state Elements to Photoemissive Devices”, Adv. Electron. Electron Phys., Vol.22B, pp.671-682, 1966

[6] P. Chevalier, “Photomultiplicatuer a haute resolution utilisant un multiplicateur semiconducteur”, Nucl. Instr. and Meth. Vol.50, pp.346-348, 1967

[7] E. A. Beaver and C. E. McIlwain, “A Digital Multichannel Photometer”, Rev. Sci. Instrum. Vol.42, pp.1321-1324, 1971

[8] E. A. Beaver and C. E. McIlwain, “Counting Image Tube Photoelectrons with Semiconductor Diodes”, Adv. Electron. Electron Phys., Vol.33B, pp.863-871, 1972

[9] R. G. Tull et al., “ Self-Scanned Digicon: a Digital Image Tube for Astronomical Spectroscopy”, Applied Optics, Vol.14, No.5, pp.1182-1189, 1975

[10] R. O. Ginaven et al., “Solid State Imagers for Astronomy”, Proc. SPIE, Vol.290, pp.81-89, 1981

[11] R. DeSalvo, “Hybrid Photo Diode tube”, CLNS 87-92, Cornell University, Ithaca NY 14853, 1987

[12] L. K. van Greest and K. W. J. Stoop, “Hybrid phototube with Si target”, Nucl. Instr. and Meth. A310, pp.261-266, 1991

[13] R. DeSalvo et al., “First results on the hybrid photodiode tube”, Nucl. Instr. and Meth. A315, pp.375-384, 1992

[14] C. Datema et al., “Hybrid photodiodes in scintillation counter application”, Nucl. Instr. and Meth. A387, pp.100-103, 1997

[15] G. A. Johansen and C. B. Johnson, “Operational characteristics of an electron-bombarded silicon-diode photomultiplier tube”, Nucl. Instr. and Meth A326, pp.295-298, 1993

[16] M. Suyama et al., “ A Compact Hybrid Photodetector”, IEEE Trans. Nucl. Sci. NS-44, No.3, pp.985-989, 1997

[17] J. B. Barton et al., “Performance analysis of EBS-CCD imaging tubes / Status of ICCD development“, Proc. Int. Conf. on the Application of CCD, pp.133-145, 1975

[18] M. Lemonier et al., “Thinned Backside-Bombarded RGS-CCD for Electron Imaging”, Adv. Electron. Electron Phys. Vol.64A, pp.257-256, 1985
[19] J.C. Richard and M. Vittot, “Recent developments and applications on electron-bombarded CCDs in image intensifier tubes”, Nucl. Instr. and Meth. A315, pp.368-374, 1992
[20] G. Williams et al., “Electron-bombarded back-illuminated CCD sensors for low light level imaging application”, Proc. of SPIE Vol.2415, pp.211-235, 1995
[21] G. M. Williams et al., “Back-illuminated and electron-bombarded CCD low light level imaging system performance”, Proc. of SPIE Vol.2551, pp.208-223, 1995
[22] M. Suyama et al., “An Electron bombardment CCD tube”, Proc. of SPIE Vol.3173, pp.422-429, 1997
[23] T. Maruno et al., “Newly improved very high sensitive Electron Bombardment CCD sensor and camera”, Proc. of SPIE Vol.3965, pp.223-229, 2000
[24] M. Muramatsu and M. Suyama, “Special CCD image sensors (in Japanese)”, O plus E Vol.23, No.4, pp.455-461, 2001
[25] V. W. Aebi et al., “Gallium Arsenide Electron Bombarded CCD Technology”, Proc. of SPIE Vol.3434A, pp.37-44, 1998
[26] J. P. Choisser, “Detecting Photoelectron Images with Semiconductor Arrays for Multichannel Photon Counting”, Optical Engineering Vol.16, No.3, pp.262-266, 1977
[27] P. Cushman, “A photomultiplier tube incorporating an avalanche Photodiode”, Nucl. Instr. and Meth. A333, pp.381-390, 1993
[28] N. Kanaya, “HPD for linear colliders”, Nucl. Instr. and Meth. A442, pp.295-299, 2000
[29] Catalogue of Hamamatsu Photonics K.K., Electron Tube Center, “Compact Hybrid Photo-detector”, September 2000
[30] S. M. Bradbury et al., “Test of the new hybrid INTEVAC intensified photocell for the use in air Cherenkov telescope”, Nucl. Instr. and Meth. A387, pp.45-49, 1997
[31] R. Mirzoyan, “An evaluation of the new compact hybrid photodiodes R7110U-07/40 from Hamamatsu in high-speed light detection mode”, Nucl. Instr. and Meth. A422, pp.140-145, 2000
[32] M. Akatsu et al., “Time-of-Propagation Cherenkov counter for particle identification”, Nucl. Instr. and Meth. A440, pp.124-135, 2000
[33] S. Matsui et al., “HAPD time-resolution study under single-photon irradiation”, Nucl. Instr. and Meth. A463, pp.220-226, 2001
[34] K. A. Costello et al., “Imaging GaAs photodiode with 40% quantum efficiency at 530 nm”, Proc. of SPIE Vol.1243, pp.99-106, 1990
[35] M. Suyama et al., “A hybrid photodetector with a III-V photocathode”, IEEE Trans. Nucl. Sci., NS-45, No.3, pp.572-575, 1998
[36] J. P. Edgecumbe et al., “A GaAsP Photocathode with 40% QE at 550 nm”, Proc. of SPIE

Vol.1655, pp.204-210, 1992
[37] The LHCb Collaboration, “LHCb Technical Proposal”, CERN/LHCC 98-4, LHCC/P4, 1998
[38] T. Gys, “The pixel hybrid photon detectors for the LHCb-rich project”, Nucl. Instr. and Meth. A465, pp.240-246, 2001
[39] A Braem et al., “Highly segmented large-area hybrid photodiodes with bialkali photocathodes and enclosed VLSI readout electronics”, Nulc. Instr. and Meth. A442, pp.128-135, 2000
[40] S. Basa et al., “Test results of the first Proximity Focused Hybrid Photodiode Detector prototype”, Nucl. Instr. and Meth. A330, pp.93-99, 1993
[41] H. Arnaudon et al., “Proximity focused hybrid photo diode characteristics evaluations”, Nucl. Instr. and Meth. A342, pp. 558-570, 1994
[42] P. Cushman, “Multi-pixel hybrid photodiode tubes for the CMS hadron calorimeter”, Nucl. Instr. and Meth. A387, pp.107-112, 1997
[43] P. Cushman et al., “Custom HPD readout for the CMS HCAL”, Nucl. Instr. and Meth. A442, pp.289-294, 2000
[44] C. P. Datema et al., “Results obtained using 61-pixel Hybrid Photodiode scintillation camera”, Nucl. Instr. and Meth. A422, pp.656-600, 1999

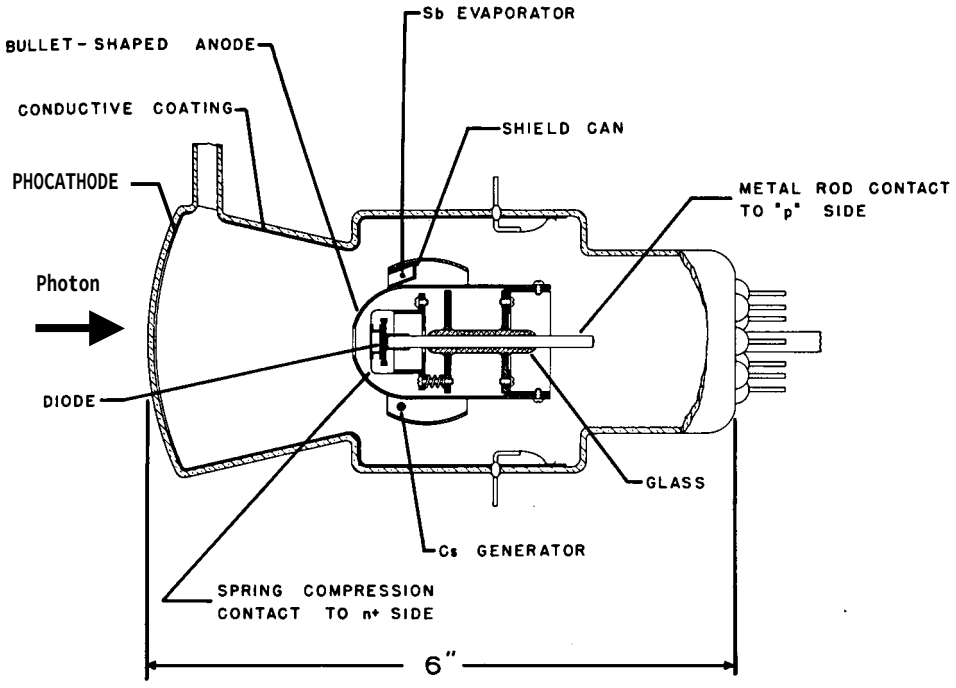

Fig. 2.1: Structure of an HPD in its early development [3].

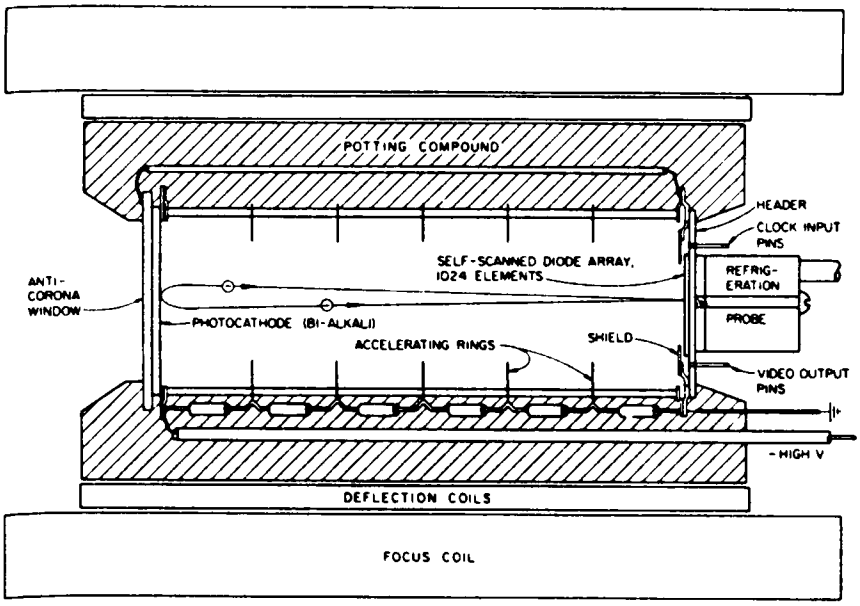

Fig. 2.2: Structure of a Digicon tube [9].

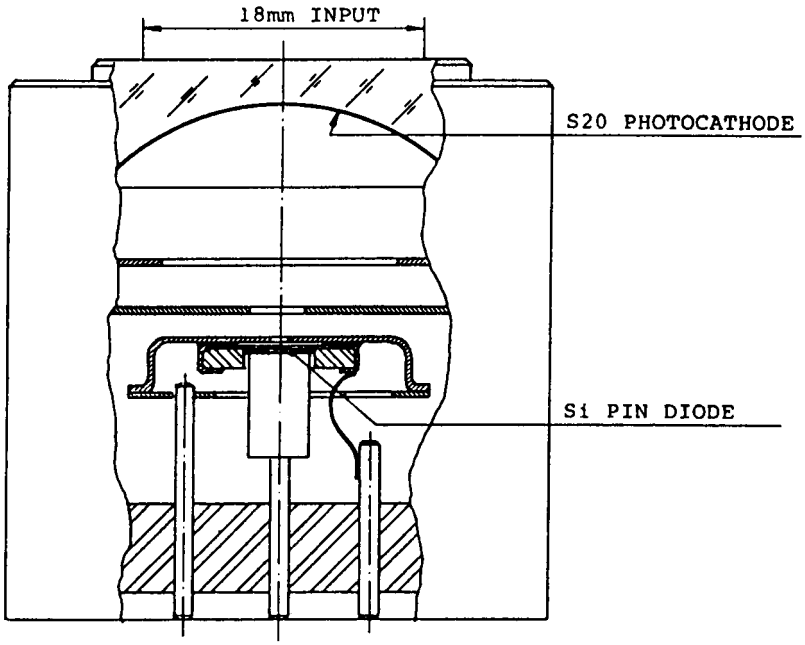

Fig. 2.3: Structure of an electrostatically focused HPD [12].

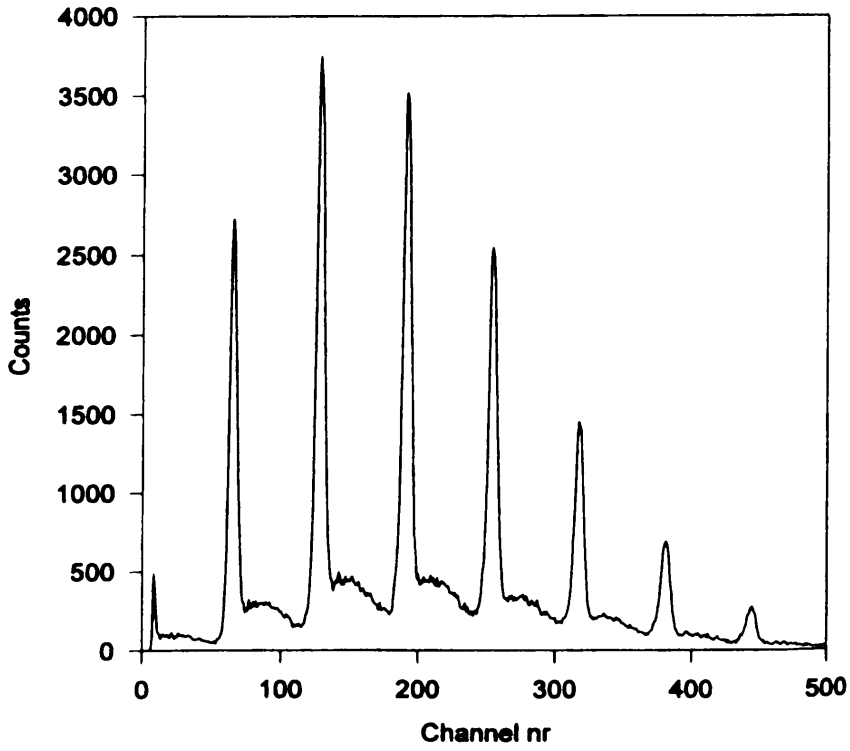

Fig. 2.4: Pulse-height spectrum measured by an electrostatically focused HPD [14].

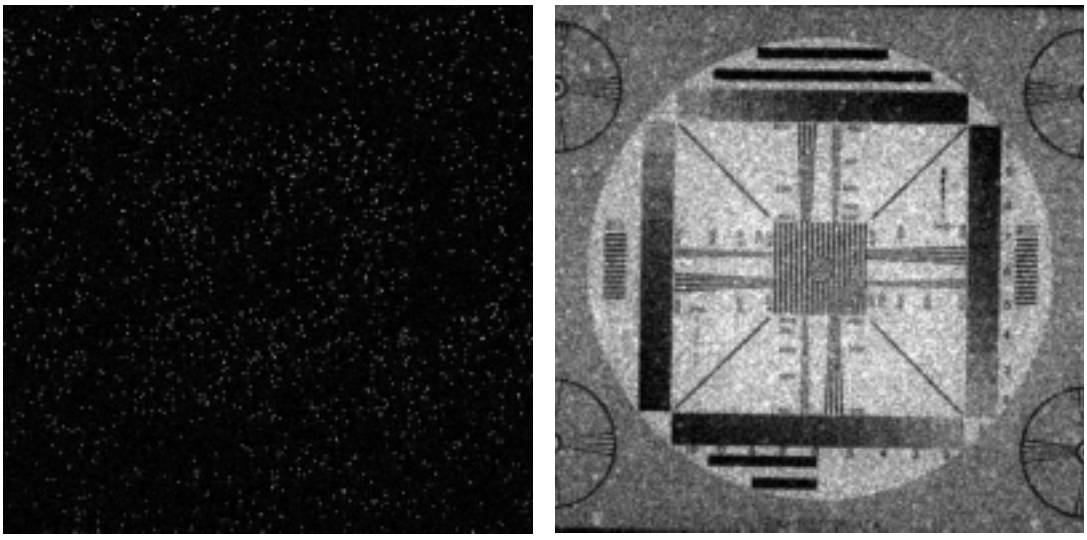

(a) Exposure time of 20ms **(b) Exposure time of 20s.**

Fig. 2.5: Chart image by EB-CCD showing the single-photon imaging capability [22].

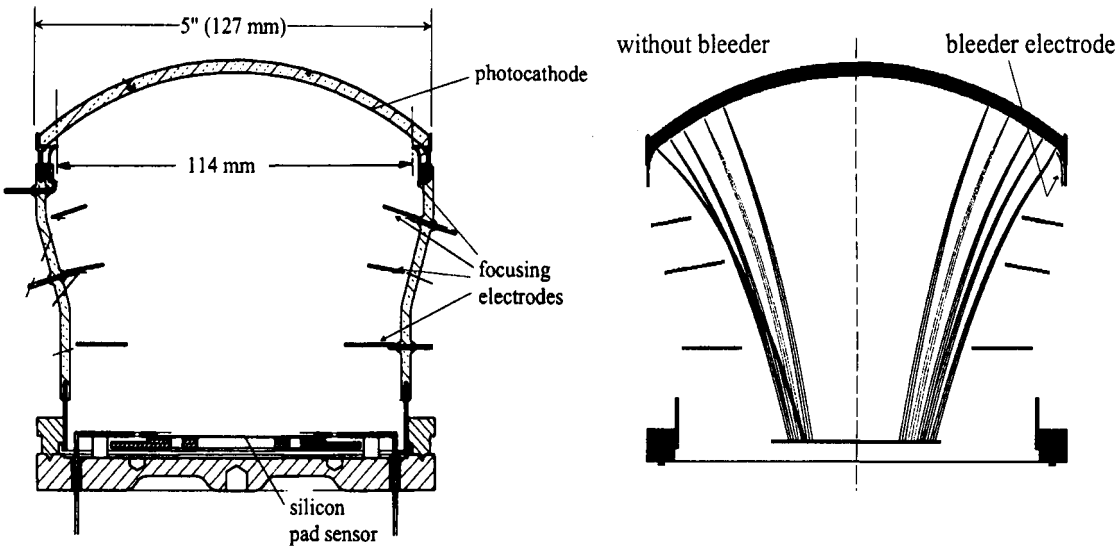

(a) Tube structure **(b) Electron trajectory.**

Fig. 2.6: Structure of a pad HPD [40].

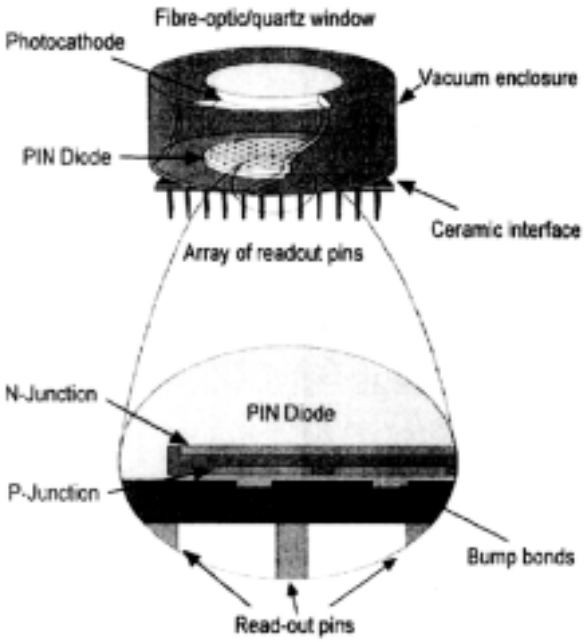

Fig. 2.7: Structure of a proximity focused HPD [44].

Chapter 3

Design concept of
a multi-pixel hybrid photo-detector

3.1 Conceptual design

In spite of many technical advantages, no attempt has been made to develop a hybrid photo-detector (HPD) with a multi-pixel avalanche diode. The HPD, which we plan to develop in this study, is required to have following features:

Detection of a single photon with a time response on the order of one nano-second;
A good signal-to-noise ratio to discriminate between one and two photoelectrons;
A multi-pixel structure with a pixel size on the order of 1 mm^2; and
Operability in a magnetic field higher than 1 T.

The conceptual design of an HPD is given below.

A photocathode with a high photon-to-electron conversion efficiency (quantum efficiency, QE) is essential for a high-performance photo-detector. From the viewpoint of QE, a GaAsP photocathode [1] is attractive, because of its high QE, typically better than 50% for visible light. For the purpose of evaluating a prototype HPD, it is more preferable to adopt a photocathode, which is widely used and easily handled. Therefore, we chose a multi-alkali photocathode for this prototype HPD. A photocathode of 25mm in diameter was chosen because of availability.

The photocathode and the avalanche diode (AD) should be facing each other with a small distance to minimize the effect of any magnetic field. This proximity focused structure is essential for vacuum tubes to be used in a high magnetic field. The distance between the photocathode and the AD is determined by the voltage applied between them and the required spatial resolution.

For the detection of a single photon with a time response on the order of one nano-second, the gain should be higher than 10^4, taking the typical noise of a high-speed amplifier into consideration. Then, an electron-bombarded gain (m_{EB}) higher than 1000 and an avalanche gain higher than 10 become target numbers to be achieved in this study. To attain an m_{EB} of 1000, the applied voltage between the photocathode and the AD should be higher than 6 kV. The voltage between them determines the kinetic energy of electrons entering the AD, thus determines m_{EB}.

The AD is pixellated for multi-pixel operation. The actual pixel size is to be determined, while taking account of the capacitance to achieve a time response of less than 1 ns. An individual pixel area on the order of 1 mm^2 is preferable to realize reasonable granularity with an effective area of 25 mm in diameter. The number of output pins, which can be housed on the stem, should also be considered. The shape of the AD is required to be rectangle, because of the dicing process. The AD must be stable under electron irradiation with an avalanche gain higher than 10. Since there did not exist such an AD which satisfied all of these requirements, we had to develop an AD for this HPD.

3.2 Design goal

The dimensions and design goal of the HPD to be developed are listed in Table 3.1. The selected multi-alkali photocathode has a QE of 20% typically at a wavelength of 400 nm. -8 kV is applied to the photocathode for m_{EB} to be approximately 1200. The AD which we use had an effective area of 16×16 mm^2, which has a good matching to the effective area of a circular photocathode. A pixel size of 2×2 mm^2 gives a capacitance of less than 9 pF. This guarantees for this HPD to have the time response of less than 1 ns. Then, the number of pixels is 64 pixels (8×8 pixels). The target avalanche gain of 30 leads to a total gain of 3.6×10^4. This high gain enables the detection of a single photon, even with a high-speed amplifier. The HPD can discriminate between one and two photoelectrons because of its high gain in the first multiplication stage, and can be used in a high magnetic field due to the proximity focused structure.

Parameter		Description / Value	Unit
Photocathode	Material	Multi-alkali	
	Quantum efficiency	20 (at 400 nm)	%
	Effective diameter	ϕ 25	mm
	Applied voltage	-8	kV
Avalanche diode	Pixel size	2 ×2	mm^2
	Pixel number	8 × 8	
	Effective area	16 × 16	mm^2
	Capacitance (per pixel)	9	pF
Gain	Avalanche Gain	30	
	Electron-bombarded gain	1200	
	Total gain	3.6×10^4	
Time response	Rise time	1.0	ns
	Decay time	1.0	ns
Others	Discrimination between one and two photoelectrons		
	Operability in a magnetic field of higher than 1 T		

Table 3.1: Dimensions and design goal of a multi-pixel HPD.

3.3 Operation

The structure of a multi-pixel HPD is schematically shown in Fig. 3.1. Electron multiplication proceeds according to the following three steps: 1) Electrons are emitted from the photocathode to the vacuum in response to incident photons, and are accelerated by an electric field, whose direction is parallel to the tube axis with a proximity focused configuration. 2) When the electrons bombard the AD, each electron creates a few thousand electron-hole pairs in it. 3) The number of electrons is further amplified by the avalanche multiplication by a factor of ten to hundred in the AD, and the signal comes out of the output pins of the HPD. Each step of this process is described in the following section in detail.

3.3.1 Photoelectric effect

Incident photons, which pass through the input window, are absorbed by the photocathode. Then, electrons in the photocathode are excited to the conduction band, and the excited electrons diffuse to the boundary between the photocathode and the vacuum. Some electrons are emitted to the vacuum by a quantum-mechanical tunneling effect, if they have a higher energy than the electron affinity, which is defined as the potential-energy difference between the vacuum level and the

conduction band of the photocathode. The QE is determined by three steps: 1) the absorption of photons, 2) the carrier recombination during drift, and 3) the emission probability of electrons to the vacuum. In the case of a multi-alkali photocathode, since the lifetime of electrons to be in the excited states is short, the photocathode should be thin (the order of 10 nm) so as to avoid recombination during drifting. Due to the low probability of the absorption of the visible to near infrared photons in the thin layer, the photocathode has a low QE of 10% or less for longer wavelengths.

In this photon-to-electron conversion process, the hit position is preserved to within 1 μm, because the photocathode is sufficiently thin for a multi-alkali photocathode. In addition, the time information is preserved to better than 1 ps [2]. Both the position and time characteristics are much better than those of the AD used in the prototype HPD.

3.3.2 Electron-bombarded gain in Si

When -8 kV is applied to the photocathode, emitted electrons enter the AD at an energy of 8 keV, which is deposited in the AD through an ionization process, resulting in the generation of electron-hole pairs. This is the principle of m_{EB}. The average energy to generate one electron-hole pair depends upon the material, and is 3.6 eV for Si [3]. The value of m_{EB} for an electron energy of 8 keV is then 2200 in an ideal condition. However, it is not realized for two reasons. One is back-scattered electrons, which are reflected back to the vacuum due to an interaction with Si. The other is the energy loss of electrons in the surface dead layer. A surface dead layer is developed at the entrance of the AD, even with a careful treatment, and electron-hole pairs generated there tend to recombine immediately and not to contribute to the output signal. Since electrons deposit their kinetic energy within 1 μm from the surface (see Appendix 1), even a thin dead layer can not be ignored.

The behavior of electrons entering Si can be studied by using a simulation code, PENELOPE, which was developed by F. Salvat et. al. [4]. According to a simulation, m_{EB} depends on the thickness of the surface dead layer, such as 1840, 1680 and 910 for the thickness of 50 nm, 100 nm and 300 nm, respectively, with an electron energy of 8 keV. The details of the m_{EB} value are given in Appendix 1.

3.3.3 Avalanche multiplication in an avalanche diode

As mentioned above, electron-hole pairs are generated by incident electrons within 1 μm from the input surface of an AD. Ionized electrons drift toward the pn junction due to an electric field generated by a reverse bias voltage. Then, the number of electrons is multiplied in the avalanche

multiplication region around the pn junction, where the electric field is sufficiently high. The avalanche gain is 10 to 100, depending on the reverse bias voltage. If m_{EB} is 1000, the total gain of the HPD is 1×10^4 or higher. Since the pn junction of the AD is divided into pixels, the multiplied electrons can be read out though the pixels. Although the noise factor of the APD for photon detection is generally large, the noise factor of the HPD encapsulating the AD is small due to a large m_{EB} that precedes the avalanche process.

[REFERENCES]

[1] M. Muramatsu and M. Suyama, “Special CCD image sensors (in Japanese)”, O plus E Vol.23, No.4, pp.455-461, 2001

[2] K. Kinoshita, et al., “Femtosecond streak tube”, Rev. Sci. Instrum., 58 (6), pp.932-938, 1987

[3] J. R. Fiebiger and R. S. Muller, “Pair-Production Energies in Silicon and Germanium Bombarded with Low-Energy Electrons”, J. Appl. Phys., Vol.43, pp.3202-3207, 1972

[4] F. Salvat et al., “PENELOPE – A Code System for Monte Carlo Simulation of Electron and Photon Transport”, NEA/NSC/DOC Vol. 19, 2001

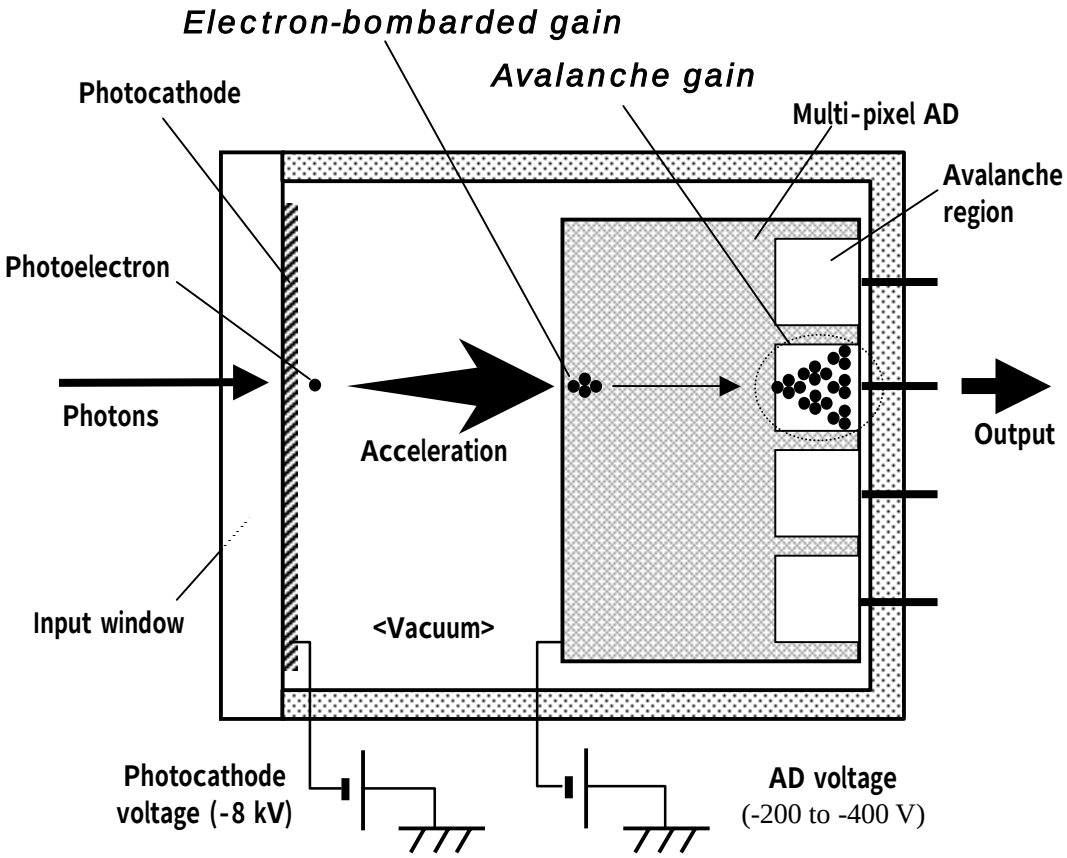

Fig. 3.1: Schematic drawing of an HPD

Chapter 4

Multi-pixel avalanche diode for electron multiplication

A multi-pixel avalanche diode with a large sensitive area is one of the key components of a multi-pixel hybrid photo-detector (HPD). There exist several kinds of avalanche photodiodes (APD) that can be used for photon detection, but they are not necessarily suited for receiving electrons in the HPD. There are many technical issues in developing a multi-pixel avalanche diode suitable for the HPD. Incident electrons might cause serious damage and charge-up, considerably degrading the performance. An unavoidable dead area between pixels should be minimized when designing a multi-pixel structure. A stable and reliable operation in a vacuum tube for a long time is also necessary.

4.1 Operational principle of an avalanche diode

An avalanche diode (AD) is a device having an avalanche multiplication region for signal carriers. A sketch of an AD is shown in Fig. 4.1. When the reverse bias voltage is applied to the AD, the depletion layer extends from the boundary of the pn junction. Since the impurity densities determine the maximum electric field around the junction, the impurity densities in the p and n regions are carefully controlled so as to build a sufficiently high electric field for avalanche multiplication at the boundary.

Under this condition, electrons excited to the conduction band in the p layer, for example by photon irradiation, drift toward the pn junction under an electric field. In the drift process, the acceleration of electrons by an electric field and deceleration by an interaction with the lattice is repeated. Some of these electrons can generate another electron-hole pair if the electric field is high. To make this happen in Si, an electric field higher than 2×10^5 V/cm is necessary [1]. This process of generating an additional electron-hole pair is called “Impact ionization”. Around the pn

junction, impact ionization is repeated, and the number of electrons is multiplied. This cascade process is called “Avalanche multiplication”. The multiplied charges are read out by electronics connected to the AD.

4.2 Design concept of an avalanche diode for low-energy electron multiplication

4.2.1 Material

There are several semiconductor materials, such as Si, Ge, InGaAs, in which an avalanche multiplication process has been observed [2]. Among these, material with a smaller atomic number (Z) and smaller band-gap energy is preferred from the viewpoint of the electron-bombarded gain (m_{EB}). In a low-Z material, the backscattering coefficient is small [3], and electrons tend to deposit larger energies in the material, thus generating a larger number of electron-hole pairs. The smaller is the band-gap energy, the larger is the number of electron-hole pairs that results from the same energy deposit. In addition, the cost for the material and its processing should be low so as to reduce the cost of the HPD. Taking these factors into consideration, Si was selected as the most suitable material for electron multiplication. Si has an atomic number of 14, which is the second smallest next to diamond as a semiconductor material. The band gap energy is 1.1 eV.

4.2.2. Consideration on the diode structure

An avalanche photodiode (APD) is a device used to detect photons. The APD has a long history, and has been widely used in variety of fields, such as optical communication, laser ranging, optical time domain reflectometry (OTDR), high-energy physics and x-ray detection. There exist several types of APDs with different structures: a reach-through-type APD (called “APD-1” hereafter) [4], an epi-type APD (APD-2) [5], a reverse reach-through-type APD (APD-3) [6], a beveled-type APD (APD-4) [7][8] and a reach-through APD with back illumination type (APD-5) [9]. The structures and electric fields of these APDs are schematically shown in Figs. 4.2 (a) to (e). Among these options, the most suitable APD for a multi-pixel HPD should be selected. The points for selections are: A) avalanche gain under electron irradiation, B) endurance for electron irradiation, C) capability of multi-pixel operation, D) width of the inter-pixel dead area, and E) suitability for mass production. The results are summarized in Table 4.1.

APD-1 (Reach-through type) is widely used for optical communication, laser ranging and OTDR for 800 to 850 nm, because of the simple planar semiconductor process. APD-1 is made on a p-type substrate, and has the structure of n+/p/p-/p+ from the light input side, as shown in Fig. 4.2 (a),

where "+" means a high impurity density on the order of 10^{19} cm^{-3}, and "-" means a low impurity on the order of 10^{13} cm^{-3} or less. Some photons penetrating the n+/p junction generate electron-hole pairs in the p- layer, and the generated electrons there drift toward the n+/p junction, where the avalanche region is built to multiply the number of electrons. Thus, APD-1 is designed for infrared photons penetrating the n+/p junction. In the case of electron irradiation, electrons are absorbed in the n+ layer located at the surface, and generated holes drift to the avalanche region. However, sufficient avalanche gain can not be obtained due to the low ionization coefficient of the holes. Therefore, APD-1 is not suitable for the detection of electrons.

APD-2 (Epi type), which has been developed for a scintillation detector and for spectroscopy, adopts a high-quality epitaxial p layer on an n+ substrate, and has the structure of p+/p/n/n+, as shown in Fig. 4.2 (b). The photons entering the thin p+ layer are absorbed in the p layer. Accordingly, this APD has a high sensitivity in the blue and UV regions, which are absorbed rapidly. The generated electrons drift to the avalanche region at the p/n junction, and the number of electrons is multiplied. APD-2 detects electrons in the same way, and can be used as a single pixel device. However, a large dead area between the pixels is unavoidable for multi-pixel design. The dead area is used for wiring to connect pixels and bonding pads located in an area surrounding the pixels. It becomes a serious problem if the size of pixel is small and the number of pixels is large. The dead area between pixels is estimated to be 0.25 mm for a device with 8×8 pixels. In addition, the leakage current is likely to increase during operation, because a part of the pn junction is exposed to electrons.

APD-3 (Reverse reach-through type) has the structure of p+/p/n/p-/n+, as shown in Fig. 4.2 (c). It is designed to detect photons of the blue and UV regions like scintillation light, which is absorbed in the thin p layer for a scintillation detector. With this structure, APD-3 detects electrons as well. However, there are some difficulties in fabricating a pixel structure. The p+/p/n junction is processed from the light input side on a p- bulk wafer, and the n+ layer is processed from the opposite side. Thus, a minimum thickness of 300 μm seems to be necessary for this double-sided process [10], though it is too thick to have a reasonable full depletion voltage. If it is assumed that the resistivity of the substrate is 4 kΩcm, the thickness of the p layer plus the n layer should be 25 μm, and the maximum electric field should be 3×10^5 V/cm [6]; then, the total voltage for full depletion turns out to be 400 V, 476 V and 603 V for thicknesses of 100 μm, 200 μm and 300 μm, respectively, as described in Appendix 2. For practical use, an operation voltage higher than 400 V on the surface of the APD is not realistic.

APD-4 (Beveled type), shown in Fig. 4.2 (d), which has a large sensitive area to be used for x-ray detection and the replacement of low gain PMTs, adopts a mesa process, contouring the pn junction so as to reduce the surface electric field. With this structure, a reverse bias voltage of up to 2500 V can be applied to a substrate of thicker than 200 μm, and the avalanche gain reaches 1000. A large

sensitive area, low capacitance and high gain are features of APD-4. The structure is simply p+/n/n+, and applicable for electron multiplication. However, the mesa process of this type is special and can not be processed in a standard Si manufacturing process line. Furthermore, since the AD is divided into pixels mechanically by grooves [11], the inter-pixel dead area is large. The pixel formation, itself, seems to be extremely difficult for mass production. An HPD with a single-pixel beveled-type AD had been developed [12], but it was not widely used, probably because of the cost and yield of a specially manufactured beveled-type APD.

APD-5 (Reach-through APD with back illumination) is an upside-down version of APD-1, and was developed to enhance the sensitivity in the blue and UV regions of APD-1 for spectroscopy. APD-5 has the structure of p+/p-/p/n+, as shown in Fig. 4.2 (e), and photons enter the p+ layer. It is applicable for electron multiplication. For the same reason as APD-3, thinning of the wafer is necessary for full depletion; however, no photolithography process is necessary for the back surface, and the process can be possible. In all, there are no major drawbacks from the viewpoint of the APD structure. There are some worries to use the APD, because this type of APD with a large effective area (16×16 mm^2) is not widely used due to the complicated thinning process, and has never been applied to electron multiplication. Therefore, good designing is the key issue to make an actually working HPD.

As discussed above, APD-2 to APD-5 might be used for electron multiplication, but APD-2 to APD-4 have some difficulties for a multi-pixel structure, stable operation or mass production. As a result, APD-5 was selected for a multi-pixel HPD.

Type	Reach-through APD (APD-1)	Epi APD (APD-2)	Reverse reach-through APD (APD-3)	Beveled APD (APD-4)	Reach-through APD with back illumination (APD-5)
Avalanche gain under electron irradiation	Very low	High	High	High	High
Endurance for electron irradiation	Poor	Poor	Good	Good	Good
Divided into pixel	Possible	Possible	Very difficult	Difficult	Possible
Dead area between pixels	Fair	Large	Fair	Large	Fair
Mass Production	Possible	Possible	Possible	Difficult	Possible

Table 4.1: Comparison of several avalanche photodiodes for a multi-pixel HPD.

4.2.3 Design of an avalanche diode

A sectional drawing of the AD designed for the multi-pixel structure is shown in Fig. 4.3. Multiple pn junctions are fabricated on the front surface, and electrons are irradiated from the back surface. Since this device is not used for photon detection (APD), but is used for electron multiplication in this work, it is hereafter called simply "Avalanche diode (AD)".

With such a structure, the substrate should be fully depleted, so that the generated signal electrons can reach the avalanche region before recombination. The voltage (V) needed to fully deplete the substrate can be expressed using the thickness of the depletion layer (W), the resistivity (R_s), the mobility of the carrier (μ), the charge of the electron (e) and the dielectric constant (ε) , as

$$V = \frac{W^2}{2 \times \varepsilon \times \mu \times R_s}. \tag{4.1}$$

For a reasonable operational voltage, the substrate is thinned to be 50 μm to 100 μm. In addition, a substrate of approximately 4 kΩcm is used [6] as the highest obtainable resistivity.

The impurity density of the deeply diffused p layer facing the n+ layer is carefully controlled, because it determines the electric field at the pn junction, where avalanche multiplication occurs. For an avalanche gain of 30 at a reverse bias voltage of 300V, a simulation showed that the p type impurity was 1.8×10^{16} cm^{-3} at the pn junction for a substrate thickness of 100 μm. Then, the calculated maximum electric field was 3.8×10^{5} V/cm at the pn junction.

Both the deeply diffused p layer and the n+ layer are divided into pixels at the front surface for multi-pixel operation. At the pn junction, the area of a deeply diffused p layer should be smaller than that of the n+ layer so as to avoid edge breakdown. Since the electric field at the edge is much stronger than the planar part of the pn junction, an avalanche breakdown at the edge is likely to occur at much smaller voltages than the design value.

The backside surface is a highly doped p+ layer, of which the impurity density is at a level to make an ohmic contact. This layer stops an extension of the depletion layer. If the depletion layer were to reach the backside surface, the leakage current would increase drastically. The p+ layer should be thick so as to make the leakage current low, while it should be thin to have a high m_{EB}. Since low-energy electrons, such as 8 keV, lose their kinetic energy within a micron (see Appendix 1), a thick p+ layer acts as a thick surface dead layer, where electron hole pairs recombine immediately and don't contribute the output signal. To reduce the dead layer, a so-called "Shallow junction" is preferable, which is high in density, but thin in thickness. The highly doped p+ layer is also useful for stable operation. Having low resistivity, it prevents charge-up due to electron irradiation. Since the pn junction is located at the front side, which is opposite to the entrance of electrons, there is no damage on it by irradiated electrons.

4.3 Operation of a multi-pixel avalanche diode

By applying a reverse bias voltage, the depletion layer is extended from the pn junction to the backside surface, and the electric field is highest around the pn junction. When electrons from the photocathode enter the backside surface of the AD, they lose their kinetic energy near the surface and generate secondary electron-hole pairs. Among them, electrons drift toward the avalanche multiplication region across the substrate. In the avalanche region, electrons obtain enough kinetic energy to generate additional electron-hole pairs by interactions with the lattice of Si, and thus avalanche multiplication occurs. The drift of the charges induces a current in the n+ region. In the AD, holes generated in the avalanche multiplication region primarily contribute to the output current, when they drift toward the p+ layer across the substrate. Since the n+ layer is divided into several pixels, the induced current is read out through each n+ pixel, and thus multi-pixel operation is accomplished.

The avalanche gain can be calculated using the one-dimensional model depicted in Fig.4.1, where the impurity density is varied in the *x* direction and is assumed to be uniform in the *y-z* plane. The ionization coefficients of electrons (α [/cm]) and holes (β [/cm]) for Si at an electric field of *E* [V/cm] are given by [13]

$$\alpha = 2300 \times \exp\left[-6.78 \times \left(\frac{2 \times 10^5}{E} - 1 \right) \right] \quad \text{and} \tag{4.2}$$

$$\beta = 13 \times \exp\left[-13.2 \times \left(\frac{2 \times 10^5}{E} - 1 \right) \right]. \tag{4.3}$$

Since α is much larger than β, the electron should be used as a carrier to be multiplied. The ratio of β and α ($\beta/\alpha=k$) should be as low as possible from the viewpoint of multiplication noise. The α, β and *k* factor are shown in Fig. 4.4 as a function of the electric field.

Based on the operational principle, the electron current (*In*) and the hole current (*Ip*) in the AD are written by ionization coefficients α and β as a function of the position *x* as follows:

$$\frac{dIn}{dx} = \alpha(x) \times In(x) + \beta(x) \times Ip(x) = -\frac{dIp}{dx} \quad \text{and} \tag{4.4}$$

$$In(x) + Ip(x) = I\,, \tag{4.5}$$

where a steady state is assumed [14][15]. Equation 4.4 shows that the increment of *In* is determined by both *In* and *Ip*, and that their relative contributions are α and β, respectively. Note that the total current (*I*), which is the sum of *In* and *Ip*, is constant throughout the diode, and equal to the output current. Equations 4.4 and 4.5 are rewritten as

$$\frac{dIn}{dx} = \{\alpha(x) - \beta(x)\} \times In(x) + I \times \beta(x) \quad \text{and} \tag{4.6}$$

$$\frac{dIp}{dx} = -\{\alpha(x) - \beta(x)\} \times Ip(x) - I \times \alpha(x), \tag{4.7}$$

thus leading to

$$In(x) = \frac{1}{\gamma(x)} \times \left[\int_0^x I \times \beta(x') \times \gamma(x') dx' + In(0) \right], \tag{4.8}$$

$$Ip(x) = \frac{1}{\gamma(x)} \times \left[\int_x^w \left(I \times \alpha(x') \times \gamma(x') \right) dx' \right], \text{ and} \tag{4.9}$$

$$\gamma(x) = \exp\left[- \int_0^x \left(\alpha(x') - \beta(x') \right) dx' \right]. \tag{4.10}$$

If equation 4.5 is used again at x=0, then equations 4.8 and 4.9 can be written as

$$In(0) + \left[\int_0^w \left(I \times \alpha(x') \times \gamma(x') \right) dx' \right] = I \,. \tag{4.11}$$

Since I is the output current and $In(0)$ is the input current, the avalanche multiplication gain (m_{AD}) can be written as

$$m_{AD} = \frac{I}{In(0)} = \frac{1}{1 - \int_0^w \left(\alpha(x') \times \gamma(x') \right) dx'} \,. \tag{4.12}$$

As shown in equation 4.12, the avalanche gain (m_{AD}) is a function of $\alpha(x)$ and $\beta(x)$, and can be determined by a given electric field distribution.

4.4 Evaluation of an avalanche diode

Prior to fabricating a practical AD for a multi-pixel HPD (8×8 pixels), a preliminary test was performed by manufacturing an AD of 2×2 pixels, of which the pixel size was the same as that of the final one (2×2 mm^2). The main purpose is to confirm the performance and to determine the preferable design parameters.

4.4.1 Test sample

The structure of the test sample is shown in Fig. 4.5. The impurity density of a deeply diffused p layer was varied in 3 levels (“Level A”, “Level B” and “Level C”) to establish the relation between the dose and the avalanche gain. The doses of “Level A” and “Level C” were varied by –2% and +2% from “Level B”. Two different thicknesses of the substrate (p- layer), 50 μm and 90 μm, were

tried in order to evaluate effects of the thickness on the performance. The pixel-gap was varied over 30 μm, 50 μm and 90 μm to check the width of the low-gain zone between pixels. The resistivity of the substrate was approximately 4 kΩcm. Except for these, the process parameters were chosen by the manufacturer [16] based on their experience. After the semiconductor process, the chip was mounted on a stem for testing. The stem had a hole of 4 mm in diameter to irradiate photons to the back surface of the AD. Aluminum wires are used to electrically connect between the chip and the pins of the stem.

4.4.2 V-I characteristics

The leakage current against the reverse bias voltage (AD voltage) was measured to check the diode characteristic and the breakdown voltage. The result is shown in Fig. 4.6 for a 50 μm thick substrate and in Fig. 4.7 for 90 μm. The avalanche breakdown voltage represented here by the voltage at a leakage current of 1μA is summarized in Table 4.2. It is observed that the breakdown voltage decreases from the lightly doped p layer "Level A" to the heavily doped "Level C". This is because the electric field increases with the impurity density of the p layer. It is also seen that a low breakdown voltage results with a thin substrate, simply because of the higher electric field [V/mm] at the same bias voltage [V].

Sample No.	Thickness	Impurity level	Breakdown voltage
1	53 μm	A	340 V
2	52 μm	B	251 V
3	50 μm	C	246 V
4	93 μm	A	524 V
5	95 μm	B	360 V

Table 4.2: Breakdown voltages for various thicknesses and dose of the p layer.

4.4.3 C-V characteristics

In order to confirm the development of a depletion layer, the C-V characteristics of ADs were measured. An AD voltage was applied to the p+ layer, and the capacitance between a pixel (n+) and the p+ layer was measured by a C-V meter (M1319A, Sanwa-musen-sokki K.K). The results for a wafer thickness of 50 μm and 90 μm are shown in Fig. 4.8. The capacitance decreases with the AD voltage, because the depletion layer extends deeper with the voltage. The kink seen around 100 V corresponds to the voltage, at which point the depletion layer extends beyond the deeply

diffused p layer. Beyond this voltage, the depletion layer develops rapidly. The capacitances reach constant values of 10 pF and 6.7 pF at 120 V and 140 V for thicknesses of 50 μm and 90 μm, respectively. At these voltages, the depletion layer reaches the backside surface.

When the edge effect is ignored, the capacitance (C_j) can be calculated from the area (S_p) and the thickness (W) as

$$C_j = \varepsilon \times \frac{S_p}{W}, \tag{4. 13}$$

where ε is the dielectric constant of Si. The calculated values for thicknesses of 50 μm and 90 μm are 8.4 pF and 4.6 pF, respectively. Any differences from the measured value are likely to be caused by the lateral capacitance between pixels.

4.4.4 Avalanche gain

Under a constant illumination of light on the backside surface, the output current from the AD was measured by changing the AD voltage. Then, the avalanche gain was deduced by assuming that the avalanche gain at 1 V is unity. The results for the impurity density of “Level A” to “Level C” for a thickness of 50 μm are shown in Fig. 4.9, and those for a thickness of 90 μm are shown in Fig. 4.10. The AD voltage necessary to obtain an avalanche gain of 30 is listed in Table 4.3 for each device. Since an operation voltage larger than 400 V is not preferable for stable operation, the impurity “Level A” for a 90 μm thickness is not suitable for the HPD. The others look good from the viewpoint of the avalanche gain.

The uniformity of the avalanche gain was studied by scanning the backside of the AD in 100 μm steps with a light spot of 100 μm in diameter, which is the projected image of an aperture by a lens. In this measurement, the output currents from four pixels were added. The sample was chosen from the category of “Level B” with a 90 μm thickness. An AD voltage of 300 V was applied with an avalanche gain of 45. The result is shown in Fig. 4.11. A circular response is due to the circular aperture used in front of the AD. Low-gain zones are observed as corresponding well to the pixel boundaries. The standard deviation of the gain over the effective area is 1.6%, when the average gain is normalized to 100%. The average gains of four pixels are 100%, 97%, 98% and 99%, when the maximum gain is normalized to 100%. Clearly, the gain uniformity is satisfactorily high over the whole measured area.

Sample No.	Thickness	Impurity level	Voltage at gain 30
1	53 μm	A	256 V
2	52 μm	B	215 V
3	50 μm	C	193 V
4	93 μm	A	417 V
5	95 μm	B	254 V

Table 4.3: AD voltages at an avalanche gain of 30.

4.4.5 Time response

The time response, which was another important feature, was measured by irradiating the backside of the AD with pulsed light from a laser diode, where the wavelength was 780 nm. Since the pulse width was approximately 50 ps, the pulsed light was considered to be an impulse for the AD. The output pulse from the AD was measured by an oscilloscope (Infiniium, Agilent), the bandwidth of which was 1.5 GHz and the input impedance was 50 Ω. The rise and the decay times for substrate thicknesses of 50 μm and 90 μm were measured at various AD voltages. The results are plotted in Figs. 4.12 and 4.13. The output waveform at 200 V is shown in Fig. 4.14. The rise and decay times become short with the AD voltage. Since rise and decay times of less than 1 ns are desired, the AD voltage should be higher than 150 V for thicknesses of 50 μm and 250 V for 90 μm.

The factors affecting the time response are the transit time of the carriers and the CR constant, which is determined by the product of the junction capacitance (C_j) and the input impedance of the circuit (R_{in}). The decay time (T_d) determined by the CR constant can be expressed as

$$f_T = \frac{1}{2 \times \pi \times C_j \times R_{in}} \quad \text{and} \tag{4.14}$$

$$T_d = \frac{0.35}{f_T}, \tag{4.15}$$

where f_T is the cutoff frequency. Using the measured capacitances of 6.7 pF and 10 pF, and an R_{in} of 50 Ω, T_d is calculated to be 0.74 ns for a substrate thickness of 90 μm, and 1.1 ns for 50 μm. They are close to the measured decay time at the maximum bias voltage. The transit time of the carrier is primarily determined by the period for holes generated in the avalanche multiplication region to reach the p+ layer, and roughly proportional to the thickness of the substrate and inversely proportional to the strength of the electric field. Under a given condition, the transit time is calculated to be 0.76 ns for a thickness of 50 μm and 1.9 ns for 90 μm at an AD voltage of 200 V. The transit time of the carrier affects the width of the output pulse, if it is much larger than the CR constant.

4.4.6 Low-gain zone between pixels

The width of the low-gain zone was measured by scanning with a 30 μm light spot in 50 μm steps. Test samples had pixel-gap widths of 30 μm, 50 μm and 90 μm. These samples had an impurity dose of "Level A" with a substrate thickness of 50 μm. An AD voltage of 250 V was applied, providing a gain of 28. As expected from geometrical reasons, the results shown in Fig. 4.15 exhibit the gap width to increase with the distance between pixels. The minimum output is approximately 55% of that observed in the normal area.

The observed low-gain zone being wider than the gap between the pixels can be explained by an edge effect of the electric field between the pixels. This effect is schematically shown in Fig. 4.16. Because of the high impurity dose of the p layer facing the n+ layer, the electric field is high compared to the gap between the pixels, and thus the equipotential lines are bent. As a result, the electrons generated around the gap of the pixels are lead to the gap region.

4.5 Avalanche diode applied to a multi-pixel hybrid photo-detector

It is concluded that Si with the structure of a reach-through APD with back illumination (denoted as "APD-5") is most suitable for a multi-pixel HPD. A test sample AD with this structure has shown promising results, thus providing us with useful information on the AD design. To achieve a fast response better than 1 ns, an AD voltage higher than 150 V is necessary. On the other hand, an avalanche gain of 30 should be realized with an AD voltage smaller than 400 V; the impurity density of "Level A" for 90 μm thickness is excluded. In addition, fabrication of the test samples has shown that a thickness of 50 μm was the minimum for an effective area of 4×4 mm^2 from the viewpoint of handling; we had difficulty to apply it to an AD of 16×16 mm^2. Taking these results into consideration, a substrate thickness of 75 μm was chosen. The impurity dose of "Level A" was selected for the deeply diffused p layer in order to obtain an avalanche gain of 30 and a time response of less than 1 ns. The gap width between pixels was chosen to be 30 μm to minimize the low-gain zone between the pixels. With these parameters, ADs of 8×8 pixels and 16×2 pixels were designed and manufactured for an HPD. A photograph of the AD of 8×8 pixels is shown in Fig. 4.17.

[REFERENCES]

[1] Hiroo Yonezu, “Hikari Tushin Soshi Kogaku (in Japanease)”, Kogaku tosho, p.389, 1984

[2] Hiroo Yonezu, “Hikari Tushin Soshi Kogaku (in Japanease)”, Kogaku tosho, pp.415-421, 1984

[3] H. H. Hunger and H. Kuchler, “Measurements of the Electron Backscattering Coefficient for Quantitative EPMA in the Energy Range of 4 to 40 keV”, Phys. Atat. Sol., (a)56, pp. k45-k48, 1979

[4] T. Yamaoka et al., “Silicon avalanche photodiodes”, Fujitsu Sci. & Tech. J., 12, pp.87-95, 1976

[5] K. Deiters, et al., “Properties of the most recent avalanche photodiodes for the CMS electromagnetic calorimeter”, Nucl. Instr. and Meth. A442, pp.193-197, 2000

[6] R. J. McIntyre et al., “A short-wavelength selective reach-through avalanche photodiode”, IEEE Trans. Nucl. Sci., NS-43, pp.1341-1346, 1996.

[7] V. L . Gelezunas et al., “Uniform large-area high-gain silicon avalanche radiation detectors from transmutation doped silicon”, Applied Physics Letters, Vol.30, No.2, pp.118-120, 1977

[8] Advanced Photonix Inc, "Noise characteristics of Advanced Photonix avalanche diode", technical note, 1991

[9] R. J. McIntyre, “Recent developments in silicon avalanche photodiodes”, Measurement Vol.3, No.4, pp.146-152,1985

[10] V. Chabaud et al., ”The DELPHI silicon strip microvertex detector with double sided readout”, Nucl. Instr. and Meth. A368, pp.314-332, 1996

[11] E. Gramsch et al., “Fast, High Density Avalanche Photodiode Array”, IEEE Trans. Nucl. Sci., Vol.41, No.4, pp.762-766, 1994

[12] P. Cushman, “A photomultiplier tube incorporating an avalanche Photodiode”, Nucl. Instr. and Meth. A333, pp.381-390, 1993

[13] Y. Musienko et al., “A simple model of EG&G reverse reach-through APDs”, Nucl. Instr. and Meth. A441, p.179-186, 2000

[14] R. J. McIntyre, “Multiplication noise in uniform avalanche diodes”, IEEE Trans. Electron Devices, Vol.ED-13, No.1, pp.164-168, 1966

[15] P. P. Webb et al., “Properties of Avalanche Photodiodes”, RCA Review, Vol.35, pp.234-278, 1974

[16] Hamamatsu Photonics K.K., Solid state division

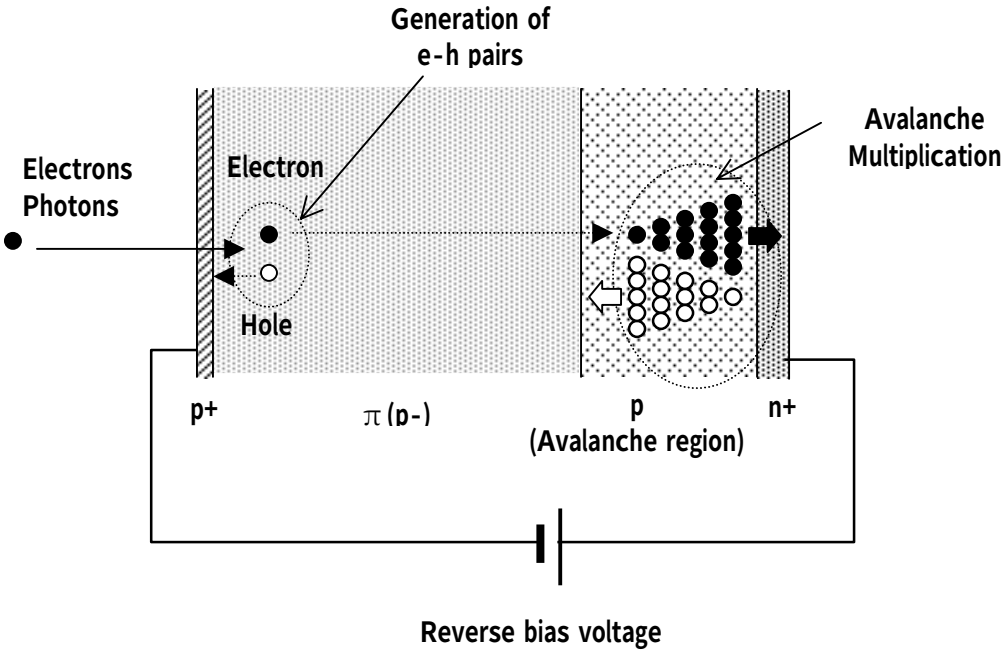

Fig. 4.1: Schematic drawing showing the operational principle of an avalanche diode.

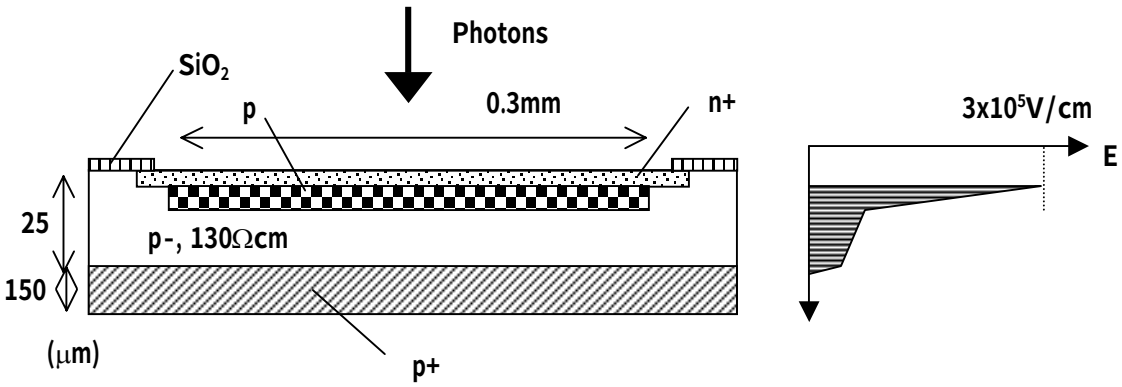

Fig. 4.2 (a): Sectional drawing of a reach-through APD (APD-1) [4].

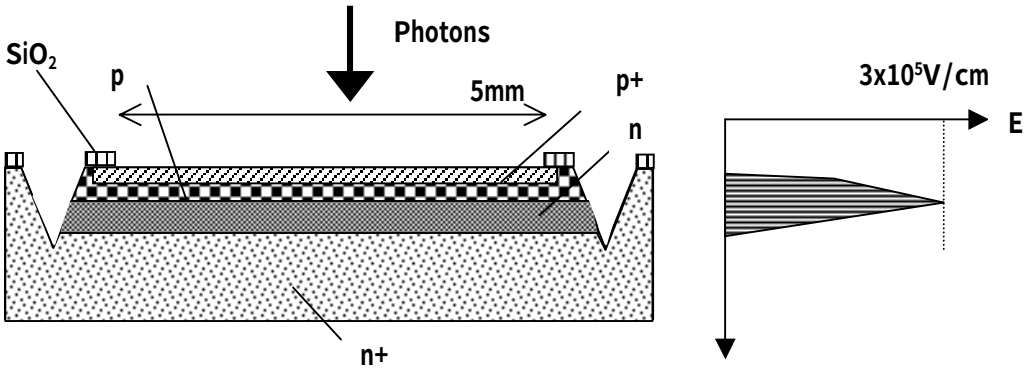

Fig. 4.2 (b): Sectional drawing of an epi-type APD (APD-2) [5].

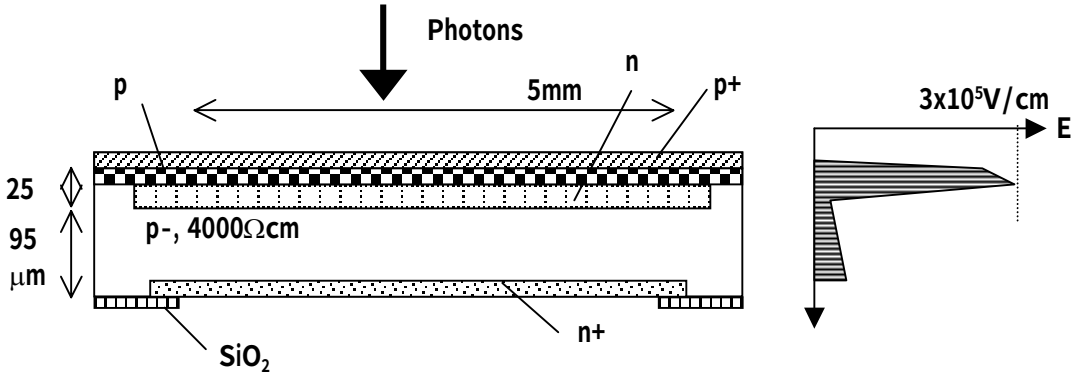

Fig. 4.2 (c): Sectional drawing of a reverse reach-through APD (APD-3) [6].

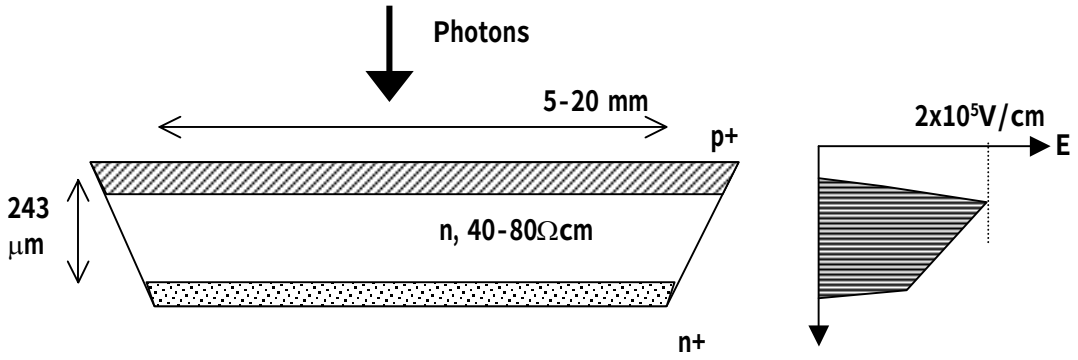

Fig.4.2 (d): Sectional drawing of a beveled APD (APD-4) [7], [8].

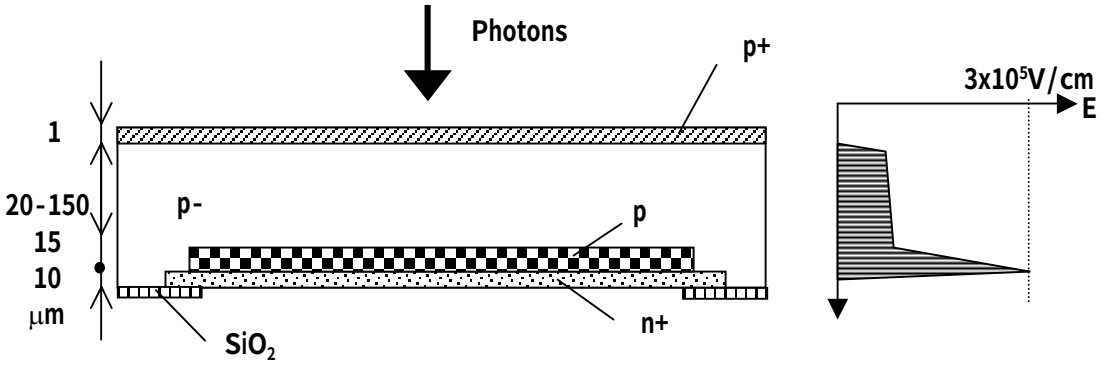

Fig.4.2 (e): Sectional drawing of a reach-through APD with back illumination (APD-5) [9].

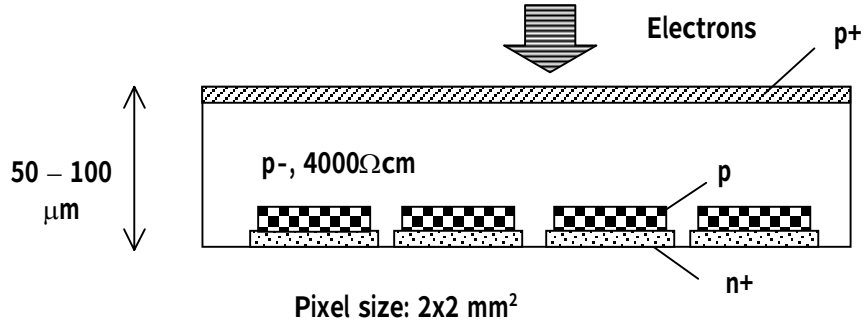

Fig. 4.3: Sectional drawing of the multi-pixel AD to be used for the HPD.

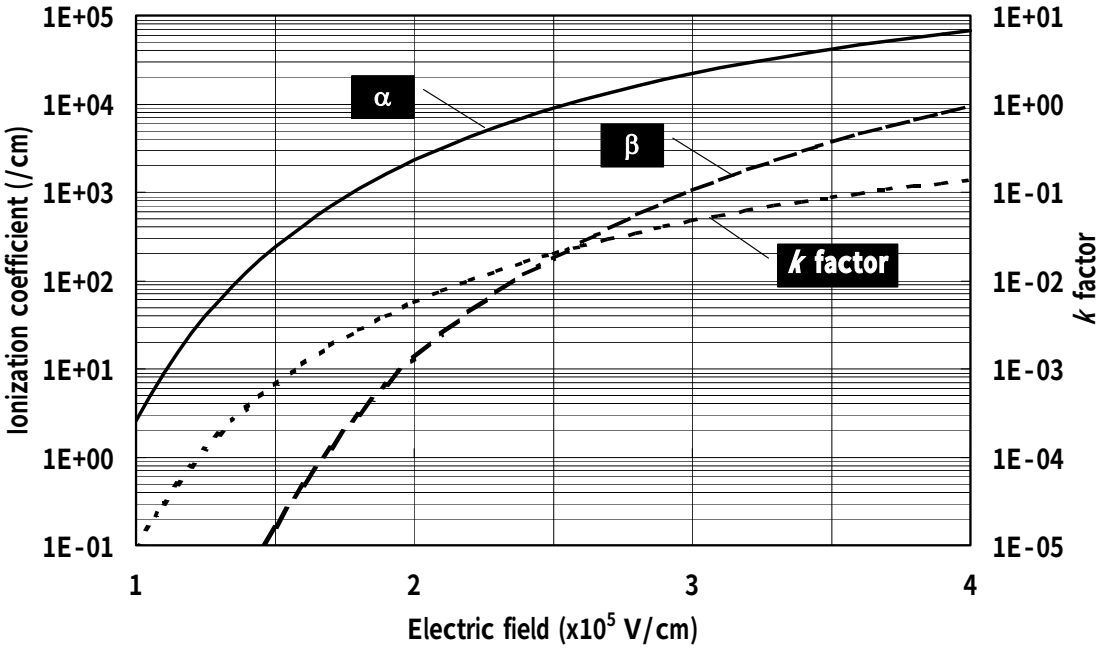

Fig. 4.4: Ionization coefficients of electrons (α), holes (β) and *k* factor as a function of the electric field. The *k* factror is calculated as β/α.

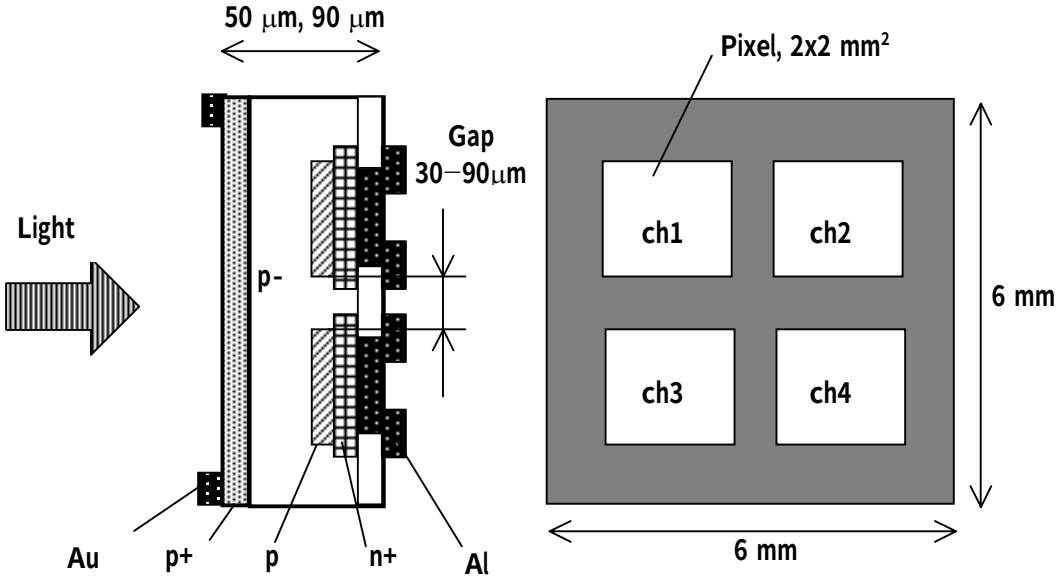

Fig. 4.5: Structure of a preliminary tested AD.

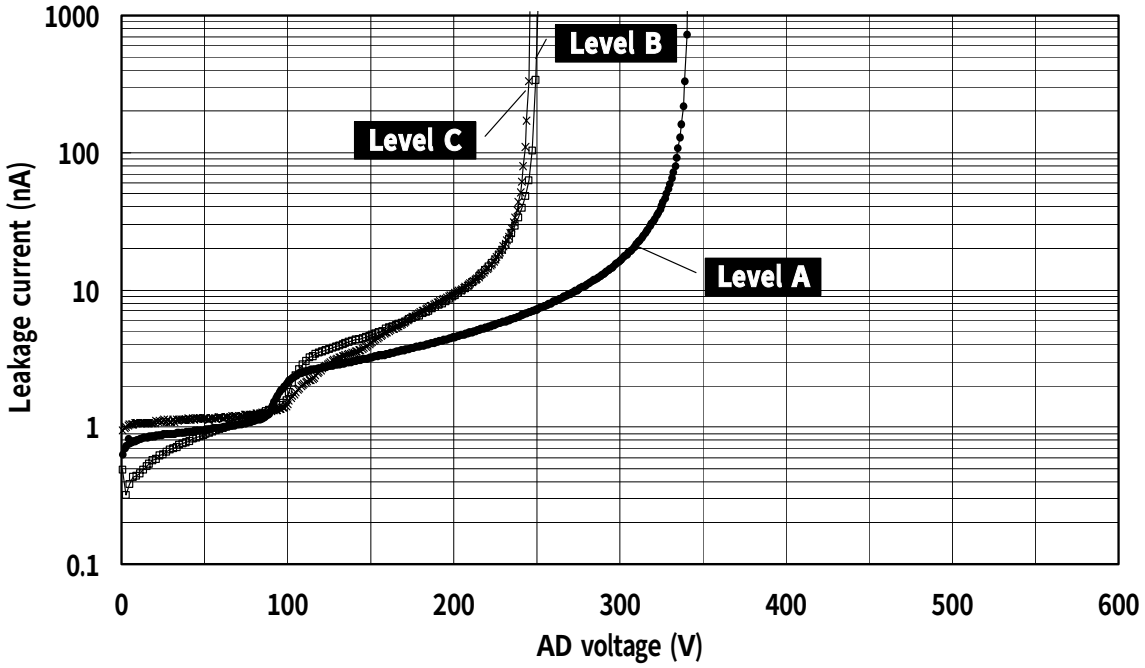

Fig. 4.6: Leakage currents of tested ADs as a function of the AD voltage. The impurity level is varied from lightly doped "Level A" to heavily doped "Level C" for a 50 μm thick substrate.

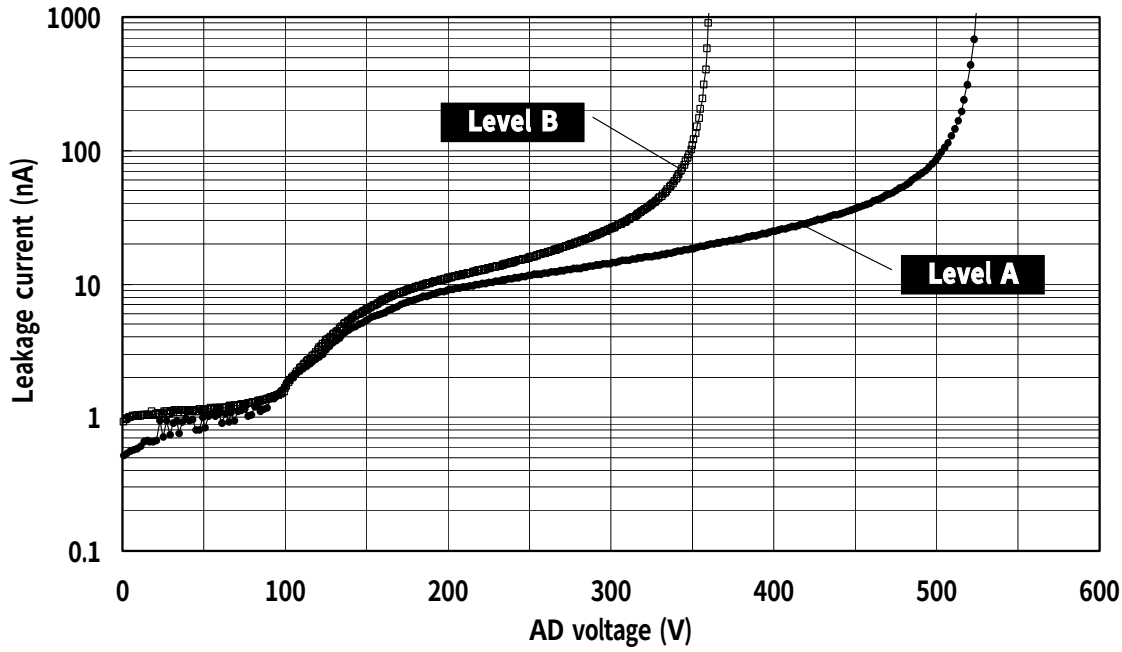

Fig. 4.7: Leakage currents of tested ADs as a function of the AD voltage. The impurity level is varied from lightly doped "Level A" to heavily doped "Level B" for a 90 μm thick substrate.

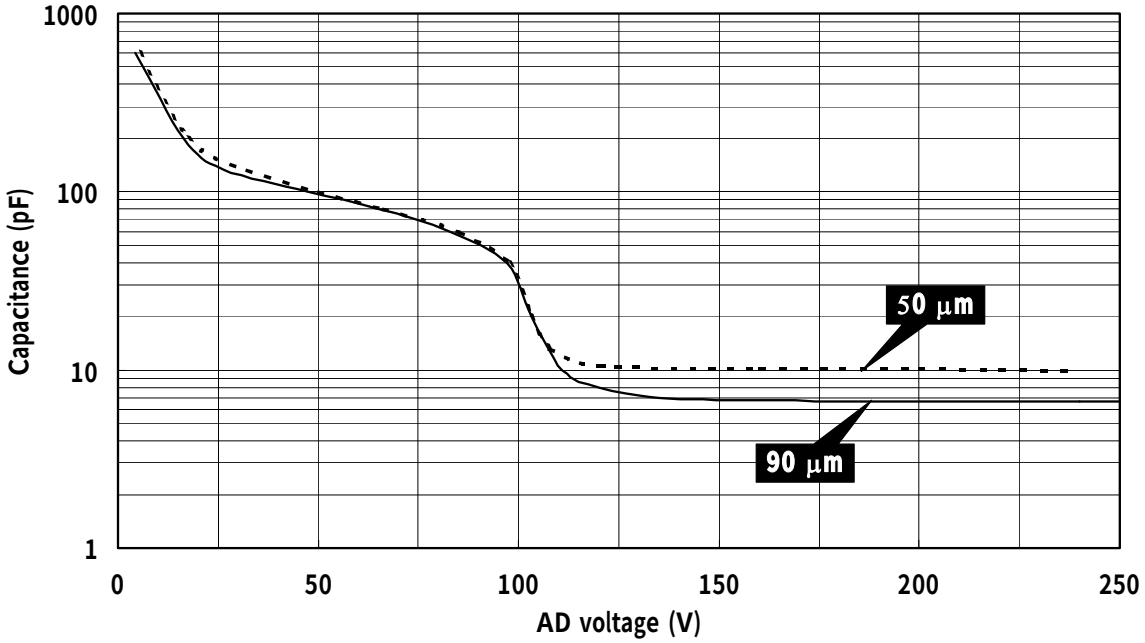

Fig. 4.8: C-V characteristics of tested ADs with substrate thicknesses of 50 μm and 90 μm.

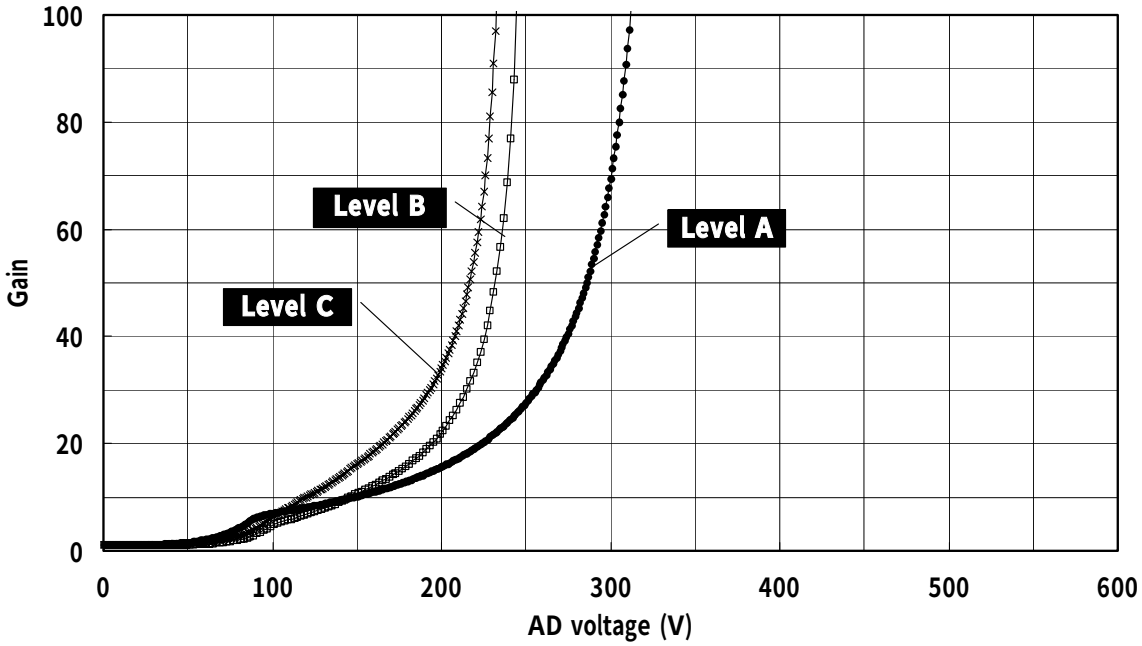

Fig. 4.9: Avalanche gains of tested ADs as a function of the AD voltage. The impurity level is varied from lightly doped "Level A" to heavily doped "Level C" for a 50 μm thick substrate.

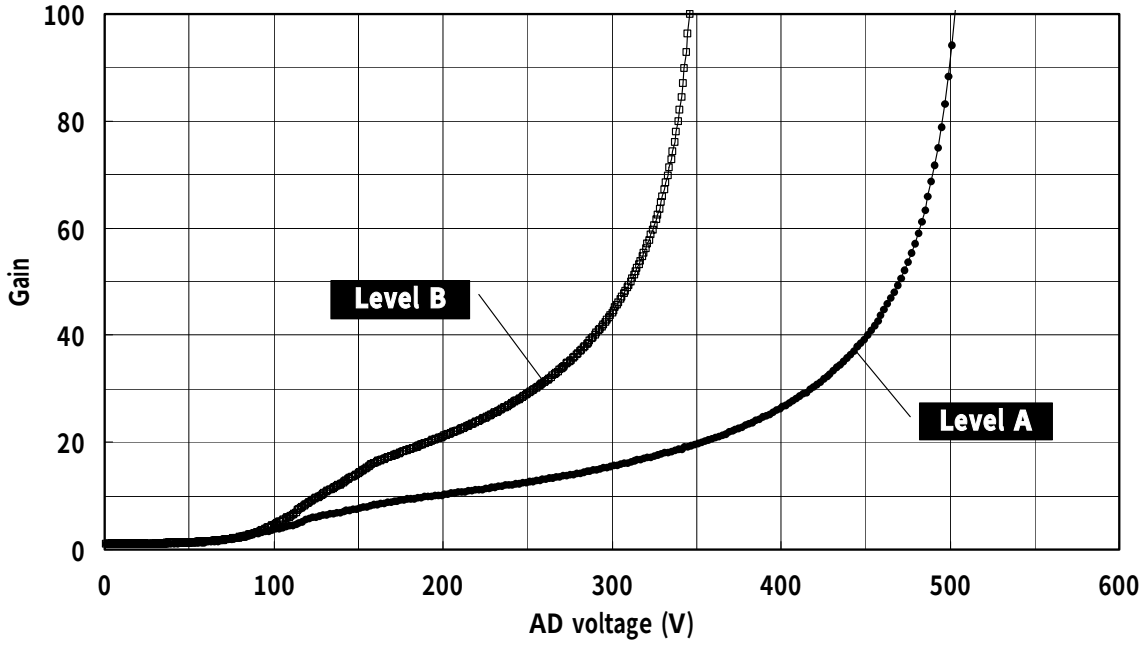

Fig. 4.10: Avalanche gain of tested ADs as a function of the AD voltage. The impurity level is varied from lightly doped "Level A" to heavily doped "Level B" for a 90 μm thick substrate.

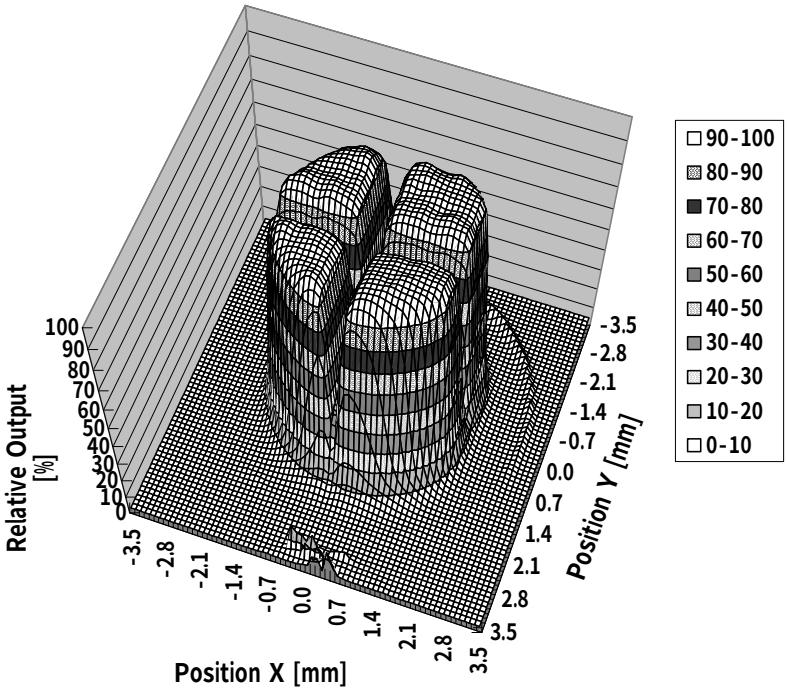

Fig. 4.11: Uniformity of an avalanche gain measured by scanning a light spot of 0.1 mm with an average avalanche gain of 45.

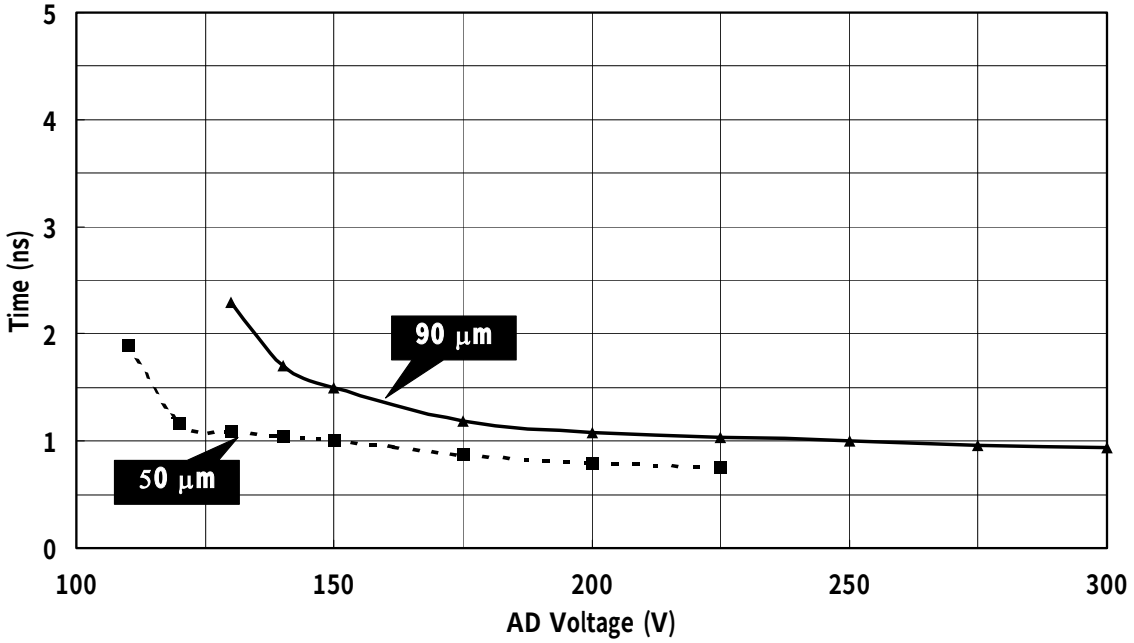

Fig. 4.12: Rises time of ADs with substrate thicknesses of 50μm and 90μm, as a function of the AD voltage.

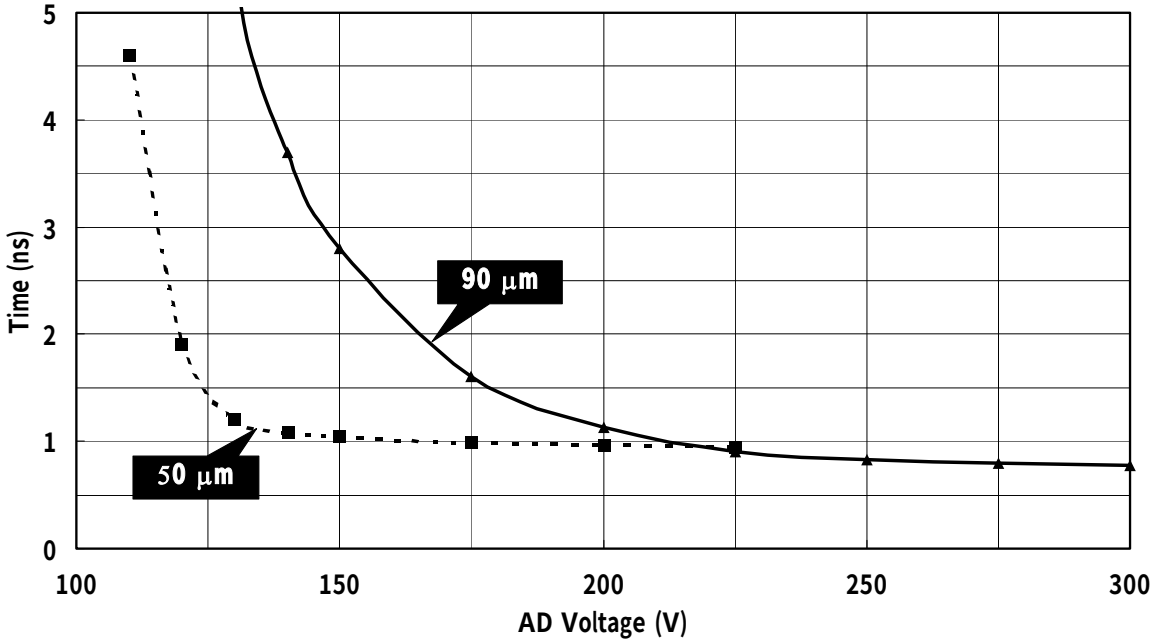

Fig. 4.13: Decay time of ADs with substrate thicknesses of 50μm and 90μm, as a function of the AD voltage.

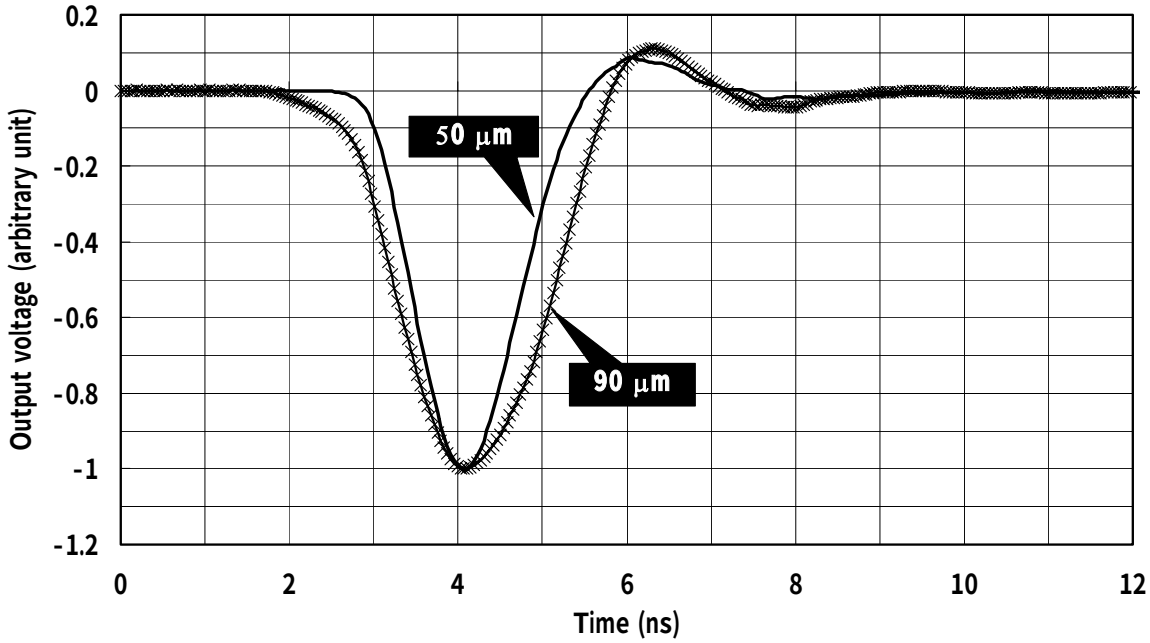

Fig. 4.14: Impulse response of ADs at 200 V with substrate thicknesses of 50 μm and 90 μm.

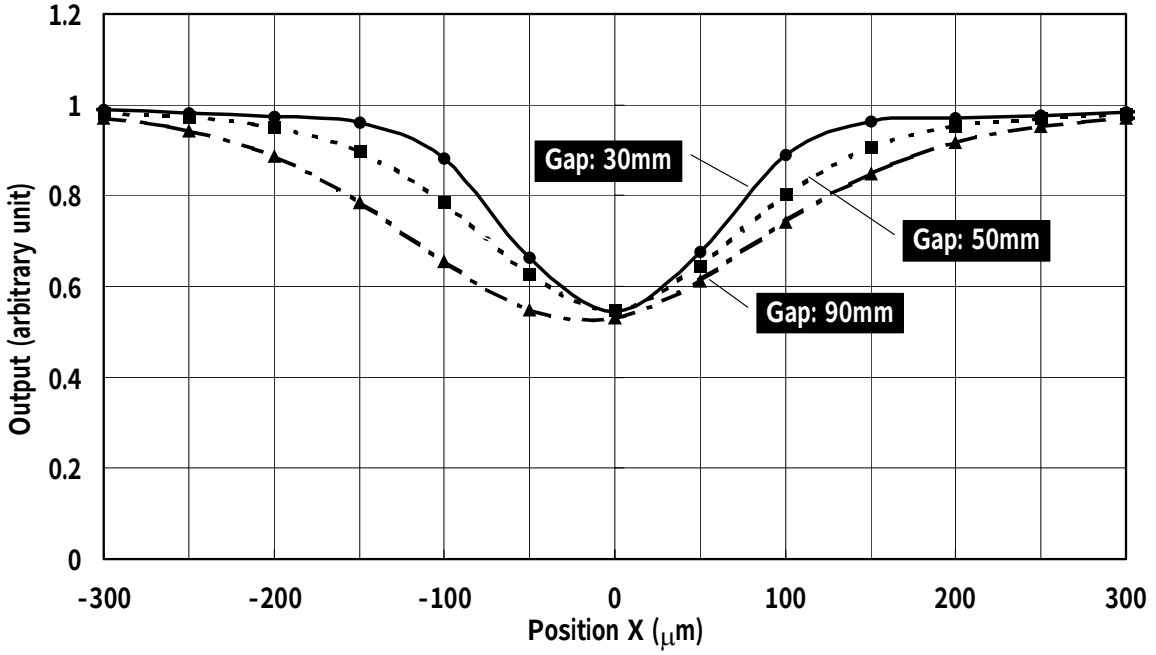

Fig. 4.15: Response of the boundary of the pixels measured by scanning a light spot of 30 μm. The pixel gap of the ADs was varied by 30 μm, 50 μm and 90 μm.

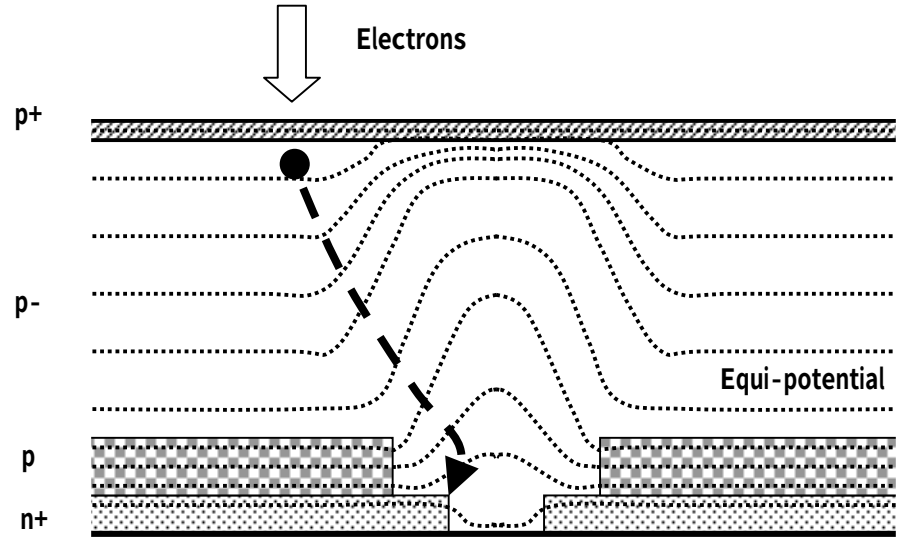

Fig. 4.16: Edge effect of the electric field between pixels.

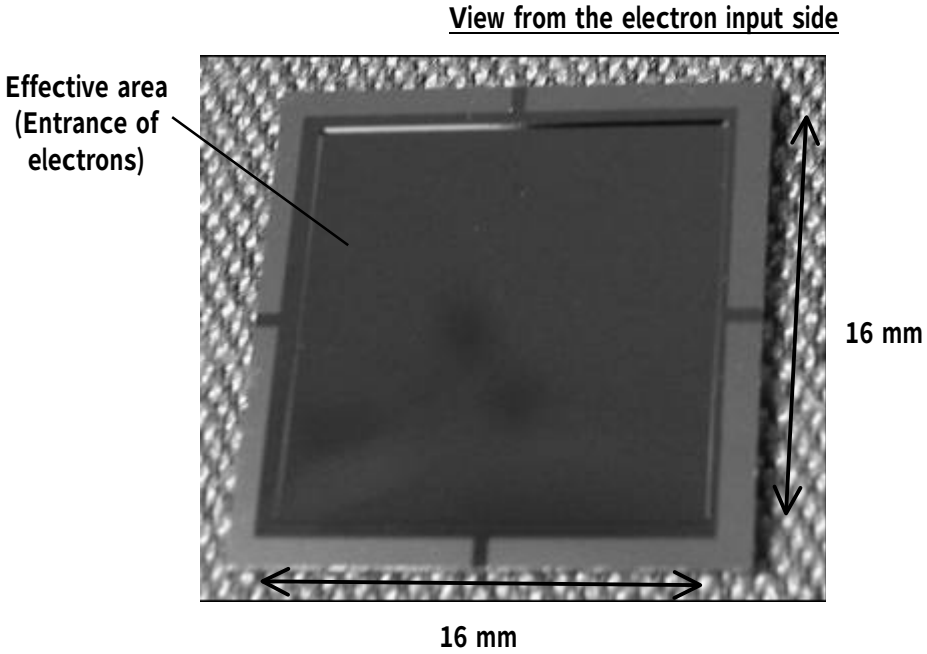

Fig. 4.17: Developed multi-pixel AD (8×8 pixels).

Chapter 5

Development of a hybrid photo-detector

Based on the design concept described in chapter 3, a proximity focused hybrid photo-detector (HPD) equipped with a multi-pixel avalanche diode was designed. The key parameter to be considered in the HPD structure is the distance between the photocathode and the avalanche diode (AD). The assembling method of the AD and the stem for the AD is also the key issue for manufacturing. The detailed structure as well as the manufacturing process are described.

5.1 Structure

A schematic drawing of the multi-pixel HPD to be developed is shown in Fig. 5.1. The primary components of the HPD are a photocathode, an AD and a vacuum container. The vacuum container consists of an input window, a cylindrical ceramic sidewall and a stem. The ceramic sidewall has two openings. The input window made of glass seals one end, and the stem does the other one to make a vacuum-tight structure. A multi-alkali photocathode is coated on the vacuum side of the input window. The AD is assembled on the stem facing the photocathode. The distance between the photocathode and the AD is 2.5mm. Output pins come out on the atmospheric side of the stem to apply a bias voltage to the AD, or to extract signals from it.

5.2 Issues in designing

5.2.1 Photocathode

The effective diameter of the photocathode is chosen to be 25 mm. Then, an AD area of 16×16

mm^2 (diagonal of 22.6 mm) has good matching to the circular photocathode effective area. Since this is a standard effective size of image intensifiers [1], the same machinery can be used for activation of the photocathode. A multi-alkali photocathode is employed. The typical spectral response of a multi-alkali photocathode is 20% in quantum efficiency from a wavelength of 200 nm to 400 nm, gradually decreasing to 10% at 500 nm, and 1% at 700 nm. It is suitable for the detection of Cherenkov light.

The input window for the photocathode could be made either of a quartz glass or of a fiber-optic plate (FOP). The quartz window has a transmission of higher than 95% from 200 nm to 300 nm, and is thus suitable for the detection of Cherenkov light. Since the FOP window is made of a bundle of optical fibers, an image focused on the input surface of the FOP is transferred to the output surface without any loss of spatial information. Therefore, the FOP is suitable to connect scintillating fibers to the window directly.

5.2.2 Application of a high voltage between a photocathode and an avalanche diode

Due to its operational principle, an HPD requires a high voltage between the photocathode and the AD. On the other hand, the best performance of the proximity focused configuration can be accomplished with a small photocathode-AD distance, resulting in a high electric field strength. Care should be taken to prevent spark discharges. In previous studies, 10 kV was applied to a gap of 1.6 mm (6.3 kV/mm) in the streak tube [2], and 8 kV to the gap of 2.5 mm (3.2 kV/mm) in the EB-CCD [3].

The spatial resolution is predominantly determined by the spread of electrons from the photocathode. When emitted from the photocathode, electrons have spreads in their initial energies and angles, and their spot on the AD may distribute widely. The spread of electrons on the AD was calculated as follows. The initial energy of electrons from the multi-alkali photocathode for 400 nm-photons exhibits a peak at 0.74 eV and a full width at half maximum (FWHM) of 0.56 eV [2], as shown in Fig. 5.2. A cosine distribution normal to the photocathode plane can be assumed for the emission angle of the electron [4]. Under these conditions, a Monte-Carlo simulation was carried out to compute the line-spread function of electrons on the AD. The photocathode voltage was fixed at -8 kV, and the photocathode-AD distance was varied from 1.5 mm to 3.5 mm. The results corresponding to 1×10^5 events are shown in Fig. 5.3. It can be seen that the spreads of electrons on the AD were 44 μm, 74 μm and 104 μm (FWHM) for distances of 1.5 mm, 2.5 mm and 3.5 mm, respectively.

Considering both the sustainable voltage between the photocathode and the AD and the simulated line spreads, the photocathode-AD distance was chosen to be 2.5 mm and the maximum voltage between them to be 8 kV.

The maximum sustainable voltage on the surface of the insulating sidewall is not as high as that of a vacuum gap. Therefore, both the input window and the stem are protruded to keep a small gap of 2.5 mm between them, while the path length on the insulating sidewall is much longer than the gap. The multi-pixel HPD shown in Fig. 5.1 was designed while taking these factors into account. This kind of structure is successfully used in image intensifiers [5][6].

5.2.3 Assembling method of an avalanche diode with back illumination

As mentioned in the section 4, the multi-pixel AD for the HPD has an electron input surface on the backside and bonding pads for electrical connection on the front side. Since the input surface should face the photocathode, a viable method of electrical connection between the AD and the stem is flip-chip bonding using bumps in between. The structure of the AD bonded to the stem is shown in Fig. 5.4. In order to ease the mechanical stress during the baking process of the HPD, the AD is once bump bonded to a connecting board made of Si, and the board is bonded to the stem. Bonding wires make electrical connections between the substrate and the stem.

5.2.4 Electrical connection from the vacuum to the atmosphere

In the HPD, wiring between the vacuum side and the atmospheric side is necessary. In the case of PMTs, glass stems with 10 to 20 metal pins are used for this purpose. This is useful to assemble dynodes on it, but is not suitable for assembling a multi-pixel AD. Furthermore, many more pins are needed for the present HPD to readout all 64 pixels of the AD. Accordingly, a different type of stem was designed for the HPD based on multi-layer ceramic technology. As a quarter of the stem shown in Fig. 5.5, there are 64 bonding pads on the vacuum side and 64 output pins on the atmospheric side. In order to connect them, a multi-layer ceramic board is used. Wiring patterns made of tungsten are formed on the surface of the second and third layers of the ceramic, and layer-to-layer connections are made through holes filled with tungsten. The layers of the ceramics are laminated and co-fired to make the body of the stem for the HPD. In this way, an electrical connection through vacuum tight structure is accomplished. A photograph of the stem is shown in Fig. 5.6.

5.3 Manufacturing process

5.3.1 Assembly of an avalanche diode

The AD is flip-chip bonded to a connecting board using bumps, as described in section 5.2.3. The connecting board with the AD is mounted on the ceramic stem. The electrical connections between the bonding pads on the board and those on the ceramic stem are made by bonding wires. A schematic drawing of the AD mounted on the stem is shown in Fig. 5.4, and a photograph is shown in Fig. 5.7.

5.3.2 Preparation of other components

A cylindrical ceramic sidewall is used for the HPD. Two circular flanges are blazed to both ends of the sidewall. The flange of the output side is welded to the stem before photocathode processing, and thus the sidewall and the stem make a single body as a part of the vacuum container. The flange of the input side holds an adhesive metal, which makes a vacuum tightness of the input window after photocathode processing.

A chromium electrode is deposited on the edge of the input window for electrical connection between the photocathode and the flange on the input side. The inner side of the window, which is made of either FOP or quartz, is processed to activate a multi-alkali photocathode, as described below.

5.3.3 Activation of a photocathode

For activating a photocathode, a large vacuum chamber, a so-called transfer system, is used [6]. Individual components of the HPD, such as the sidewall with the stem and the input window, are set separately in a baking room of the transfer system. After pumping up to an ultra-high vacuum on the order of 10^{-6} Pa, each component is baked for several hours to reduce the outgassing. Then, the input window is transferred to an activation room. In the activation process, antimony as well as alkali materials, such as sodium, potassium and cesium, are deposited on the protruding part of the input window several times. During this process, the current from the photocathode responding to incident light is monitored, and the quantity of each material is accurately controlled to acquire an optimal multi-alkali photocathode performance. The total thickness of the photocathode is several tens of nano-meters.

After activation, the input window and the sidewall with the stem are sealed together with an adhesive metal in between so as to establish a vacuum-tight structure of the tube. After the sealing

process, the HPD is taken out from the transfer system. Fig. 5.8 shows photographs of HPDs with a glass input window (HPD-16×2) and with a FOP window (HPD-8×8).

[REFERENCES]

[1] Catalogue of Hamamatsu Photonics K.K., Electron Tube Center, “Image Intensifiers”, December 2000

[2] K. Kinoshita et al., “Femtosecond streak tube”, Rev. Sci. Instrum.58 (6), pp.932-938, 1987

[3] M. Suyama et. al, “An electron bombardment CCD tube”, SPIE Vol.3137, pp.422-429, 1998

[4] M. Wada, “Opto-electronic systems (in Japanease)”, Kindaikagaku-sha, p.11, 1959

[5] K. Kinoshita and H. Mizushima, “Ultra-high sensitive imaging technology (in Japanese)”, The Journal of the Institute of Television Engineering of Japan, Vol.42, No.8, pp.794-799, 1988

[6] E. Roaux et al., “Third-Generation Image Intensifier”, Adv. Electron. Electron Phys., Vol.64A, pp.71-75, 1985

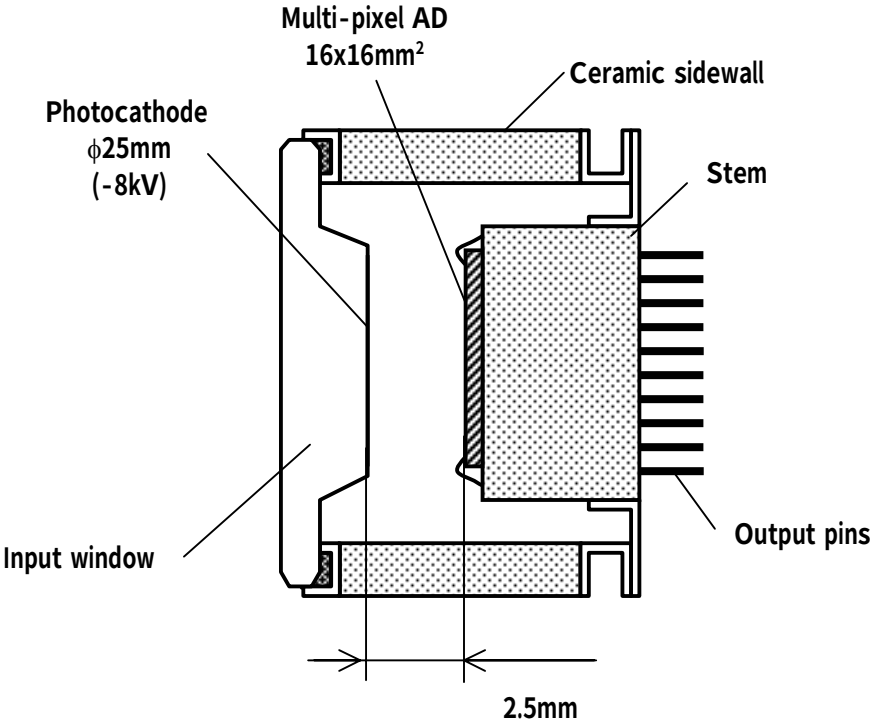

Fig. 5.1: Sketch of a multi-pixel HPD to be developed.

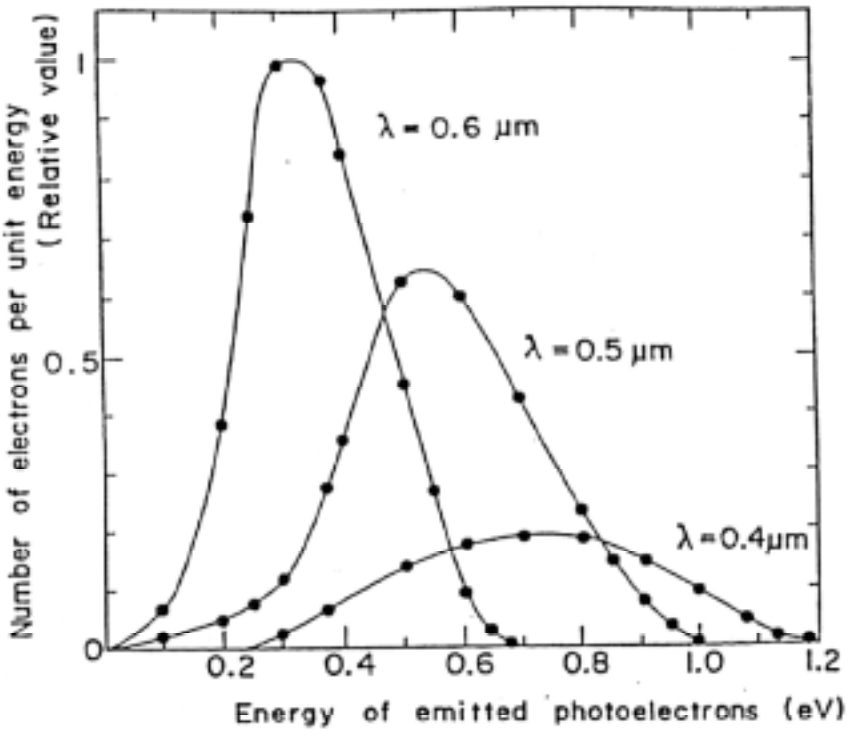

Fig. 5.2: Initial energy distribution of electrons from a multi-alkali photocathode at different wavelengths [8].

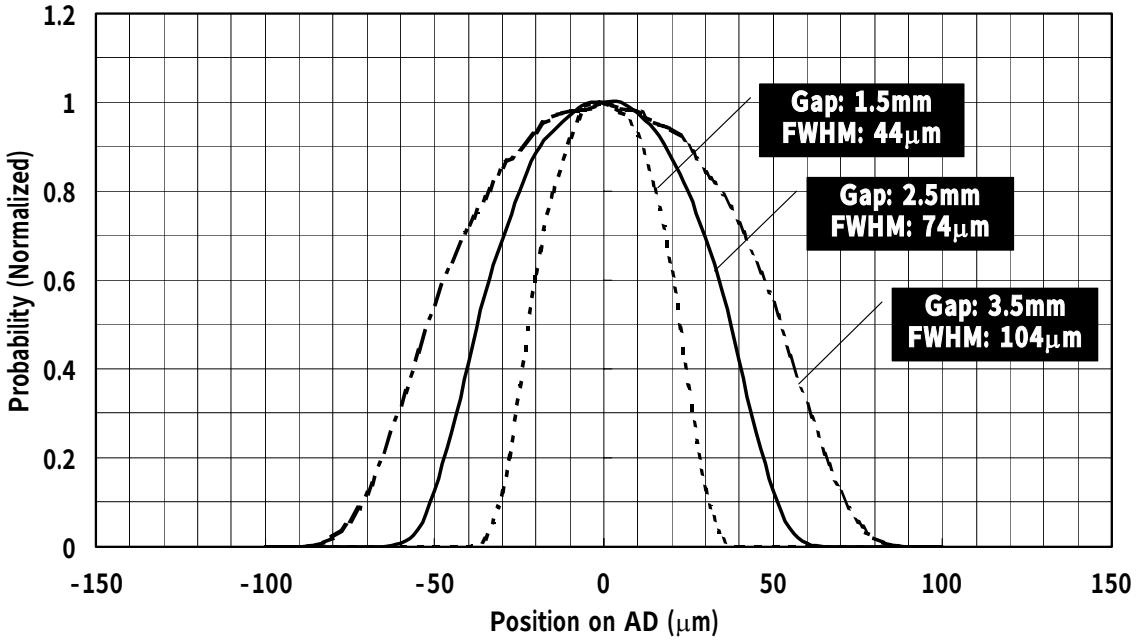

Fig. 5.3: Calculated spread of photoelectrons on the AD (line spread function) for different photocathode-AD distances.

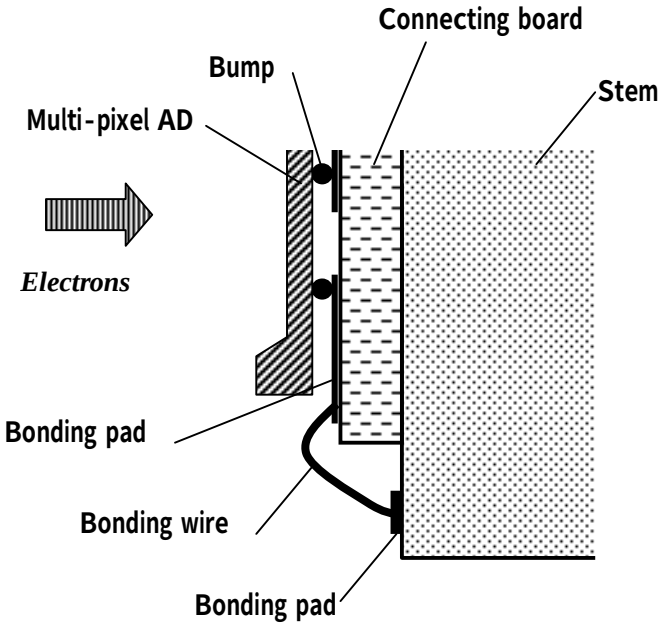

Fig. 5.4: Bonding structure of the AD.

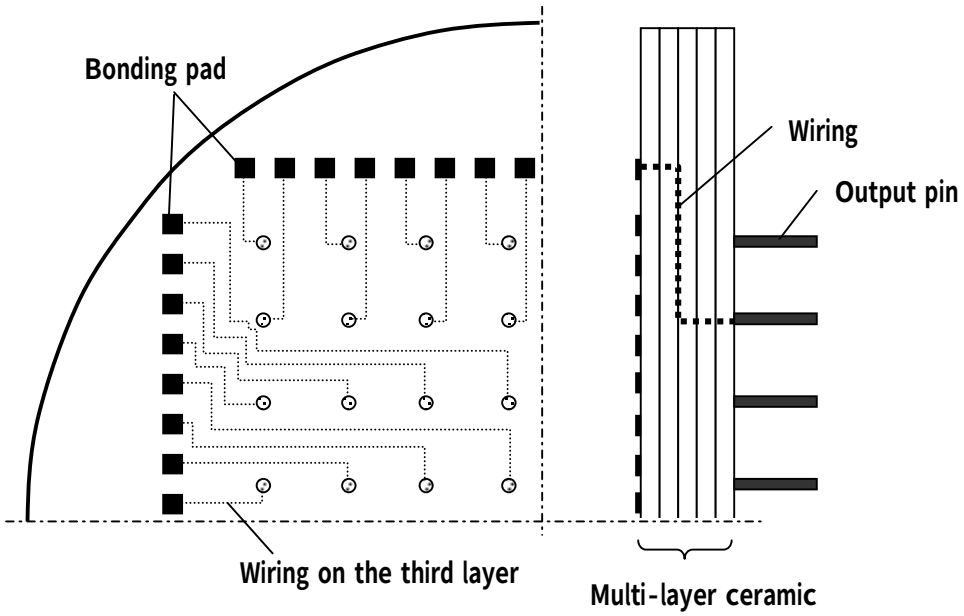

Fig. 5.5: Sketch of a quarter of the multi-layer ceramic stem.

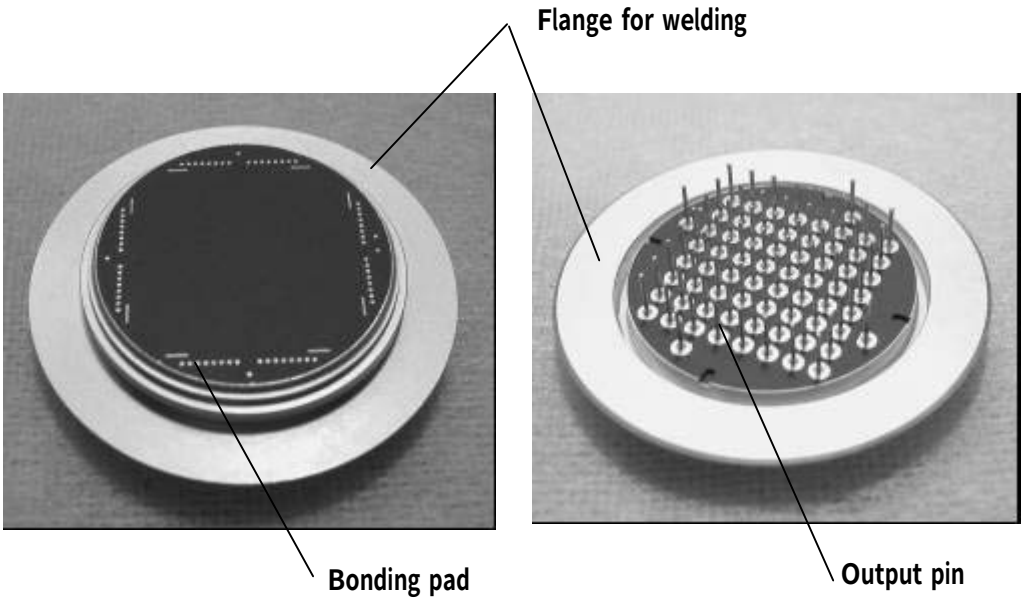

Fig. 5.6: Photograph showing the stem.

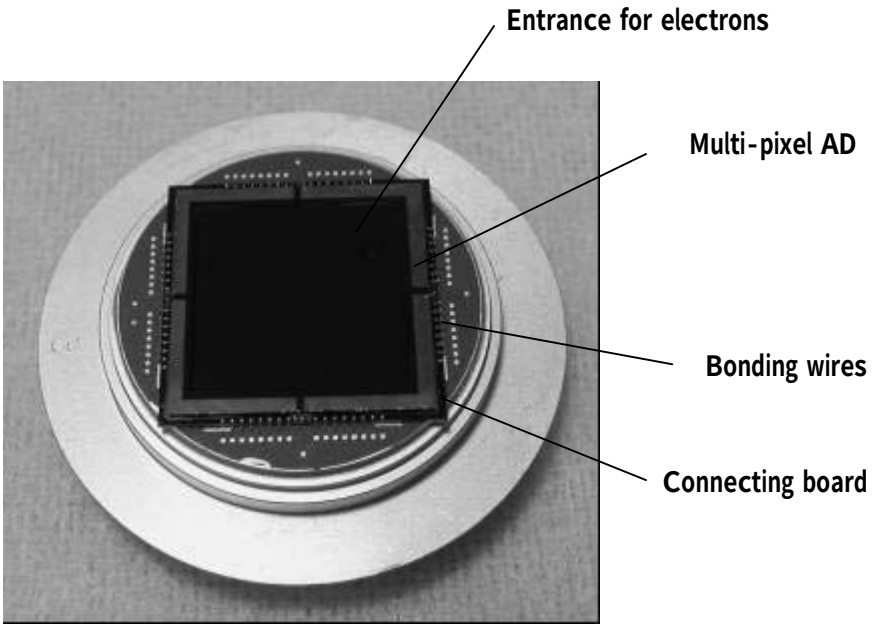

<Bump is located between the AD and the connecting board.>

Fig. 5.7: Multi-pixel AD mounted on the stem.

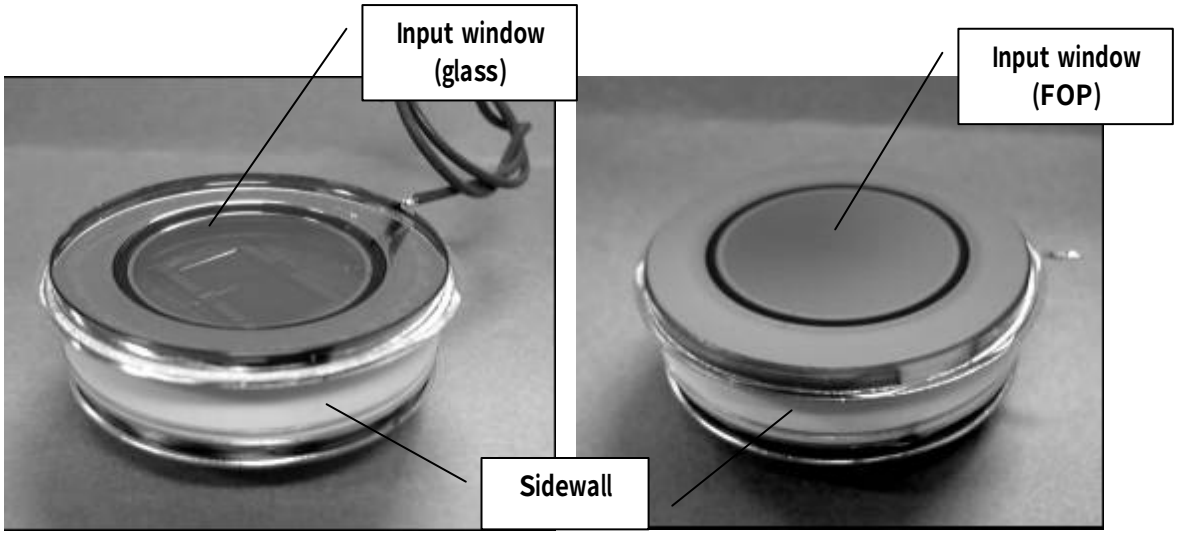

Fig. 5.8: Multi-pixel HPDs developed in this study.
HPD-16×2 with a glass window (left), and HPD-8×8 with a FOP window (right).

Chapter 6

Evaluation of a hybrid photo-detector

A few types of multi-pixel hybrid photo-detectors (HPD) were manufactured for a detailed evaluation. One (denoted as HPD-8×8) was equipped with an avalanche diode (AD) having 8×8 pixels of 2×2 mm^2 each, and the other (denoted as HPD-16×2) having 16×2 pixels of 1×4 mm^2 each, while both had multi-alkali photocathodes. The pixel patterns of these ADs are sketched in Fig. 6.1. The HPD-8×8 uses a fiber-optic plate (FOP) for the input window, whereas the HPD-16×2 has a quartz window. The ADs incorporated in the evaluated HPDs have an impurity dose of "Level A" for the deeply diffused p layer. In this chapter, the results on the HPD-8×8 are mainly reported. Since the maximum applicable voltage to the AD of HPD-8×8 is low (340V), the performance of the HPD16×2 at various AD voltages is also presented.

6.1 Fundamental performance

6.1.1 Photocathode sensitivity

The quantum efficiency (QE) of the photocathode is the photon-to-electron conversion efficiency at a wavelength (λ [nm]), which can be related to the radiant sensitivity (S_r [A/W]), defined as the conversion efficiency of the input light power (L_i [W]) to the output current (I_c [A]) as given below:

$$S_r = \frac{I_C}{L_i} \quad \text{and} \tag{6.1}$$

$$QE = \frac{S_r \times 1240}{\lambda}. \tag{6.2}$$

The measured QE of the HPD is shown in Fig. 6.2 as a function of the wavelength of the input light. It is higher than 20% in the UV and blue regions, while it is 10% or less in the visible region.

The cutoff wavelength of 360 nm for the FOP window is determined by the transmission characteristic of the FOP. These are typical responses of a multi-alkali photocathode, and are at the same level as the design goal of 20% at 400 nm.

6.1.2 Electron-bombarded gain

The photocathode current (I_c) and the output current (I_{AD}) were measured at various photocathode voltages, where light was focused onto the photocathode to generate I_c. The AD was operated at unity gain. The electron-bombarded gain (m_{EB}) was defined as the ratio of I_{AD} and I_c,

$$m_{EB} = \frac{I_{AD}}{I_C}, \tag{6.3}$$

and measured as a function of the photocathode voltages, as shown in Fig. 6.3. An m_{EB} of 1190 was observed at an operation voltage of -8 kV. This is very close to the design goal of 1200. The pair production energy, the average energy needed to produce one electron-hole pair, can be estimated from the slope of the gain to be 3.2 eV. This is close to the theoretical value of 3.6 eV [1]. The threshold voltage (V_{th}), which is thought to be determined by the thickness of the surface dead layer, is -4.2 kV. m_{EB} can be approximated by the following formula for the photocathode voltage (V [kV]) and the threshold voltage (V_{th}[kV]):

$$m_{EB} = \frac{-(V - V_{th}) \times 1000}{3.2} \quad . \tag{6.4}$$

To estimate the actual thickness of the dead layer, m_{EB} was evaluated as a function of the thickness using the simulation code PENELOPE [2]. The best fit shown in Fig. 6.3 was obtained at a thickness of 235 nm, which approximately corresponds to the thickness of the p+ layer. The details of the simulation are presented in Appendix 1.

6.1.3 Characteristics of an avalanche diode

The leakage current of the AD was measured against the reverse bias voltage (AD voltage) under a dark condition. The results (V-I characteristics) are shown in Fig. 6.4, where the summed current from all good pixels (64 pixels in HPD-8×8, 31 pixels in HPD-16×2) was measured. The measured leakage current per pixel is 1.2 nA at 285 V for HPD-8×8, and 0.7 nA at 291 V for HPD-16×2. At these voltages, the avalanche gain is 30, as shown later.

The C-V characteristics were measured by a C-V meter (M1319A, Sanwa-musen-sokki K.K). The results are shown in Fig. 6.5. In this case, all pixels were connected so as to avoid lateral capacitance between the pixels. The maximum measurable capacitance was limited to be 3000 pF due to the range of the meter. The capacitances at the full depletion voltage were 402 pF and 218

pF for 8×8 pixels and 16×2 pixels, respectively, leading to an average capacitance per pixel of 6.3 pF and 6.8 pF. These satisfy the required value of 9 pF. Using the difference of the boundary structure between the HPD-8×8 and the HPD-16×2, it is estimated that the capacitance of a pixel not facing the boundary is 5.2 pF, and the capacitance per boundary length (1.1 pF/mm) should be added for those at the boundary. A parallel-plate model for 4 mm^2 area and a 75 μm thick depletion layer gives 5.6 pF. The measured result is consistent with this calculation.

Under a constant illumination of light, the output current was measured at various reverse bias voltages. The avalanche gain was then calculated by normalizing the output current to that measured at 1 V, where the avalanche gain is considered to be unity. The result is shown in Fig. 6.6. The avalanche gain was 30 at 285 V and 291 V for HPD-8×8 and HPD-16×2, respectively. Those two HPDs show similar avalanche gain characteristics.

The measured avalanche gain under electron irradiation is shown in Fig. 6.7 for the HPD-16×2. To our surprise, it was found that the avalanche gain decreases when the photocathode voltage is increased. The avalanche gain is again shown in Fig. 6.8 as a function of m_{EB} this time. The effective avalanche gain does clearly decrease with m_{EB}. This behavior was observed for the first time. One of the possible explanations is a local space-charge effect. A primary electron from the photocathode generates one thousand electrons inside the AD, localized in a volume of several cubic microns. The localized charge compensates the electric field at the avalanche region and, therefore, reduces the avalanche gain significantly, as mentioned above. Even with gain reduction, the target avalanche gain of 30 is achieved at an AD voltage of 308 V. The total gain is 3.4×10^4 at 302 V on the AD, 5.7×10^4 at 354 V, and 8.1×10^4 at 382 V with -8 kV on the photocathode. The total gain is typically 5×10^4, and higher than the design goal of 3.6×10^4.

The resistance between two adjacent pixels of the HPD-8×8 was measured at different AD voltages. The result shown in Fig. 6.9 exhibits an increase with the AD voltage. This is because the depletion layer extends to the surface farther with a higher AD voltage. The resistance is on the order of 1 MΩ at an AD voltage higher than 200 V, which is sufficiently high for a measurement with a low-impedance circuit, such as an amplifier or a current-meter.

6.2 Pulse-height spectra

6.2.1 Pulse-height spectra at various photocathode voltages

The pulse-height spectra of HPD-16×2 for single photons were measured under several operational conditions with the experimental setup shown in Fig. 6.10. The pulsed light source was a light-emitting diode (LED) at 650 nm that provided 30 ns-wide pulses. The HPD output signal

was amplified by a charge-sensitive amplifier (ORTEC 142A), further amplified and shaped by a linear amplifier (CANBERRA, 3100-02), and then analyzed by a multi-channel analyzer (Laboratory equipment co., MCA/AT). The photocathode voltage was -7 kV, -8 kV or -9 kV with the AD voltage being fixed to 245 V. The total gains for these conditions were 1.6×10^4, 2.2×10^4 or 2.7×10^4, respectively. The measurements were made at a relatively low AD voltage to avoid the gain saturation observed at a higher voltage, as described in the next paragraph in detail.

Fig. 6.11 shows the measured pulse-height spectra for single photons. The peak channel naturally increases with the photocathode voltage, because m_{EB} increases with it. The resolution R, which is the ratio of the standard deviation of the spectrum and the peak channel, improves with the photocathode voltage. The standard deviation is simply estimated by FWHM/2.35, assuming a Gaussian distribution. The observed peak positions, FWHMs and resolutions are summarized in Table 6.1.

The improvement of the resolution with the photocathode voltage can be explained by the energy loss of electrons in the surface dead layer of the AD. When electrons from the photocathode lose a significant part of their energy in the dead layer, the energy detected in the sensitive layer would also fluctuate largely event by event. Accordingly, m_{EB} fluctuates badly. A simulation code, PENELOPE [2] (see Appendix 1), was used to simulate the energy loss in the surface dead layer and its fluctuation. Referring to the result of m_{EB}, the thickness of the dead layer was assumed to be 235 nm. The computed fractional energy loss and the fluctuation (in FWHM) of energy loss normalized to the deposited energy in the sensitive layer are shown in Fig. 6.12. The energy losses were evaluated to be 3.2 keV (46% of the incident energy) at the photocathode voltage of -7 kV, 2.9 keV (36%) at -8 kV and 2.6 keV (28%) at -9 kV, while the fluctuation of the energy loss was calculated to be 54% at -7 kV, 32% at -8 kV and 22% at -9 kV. This effect leads to a smaller fluctuation of m_{EB} for higher energy electrons, in other words, a high pulse-height resolution.

Photocathode	**-7 kV**		**-8 kV**		**-9 kV**	
AD voltage	**245 V**	**382 V**	**245 V**	**382 V**	**245 V**	**382 V**
Peak (ch)	450	1880	660	2200	760	2420
FWHM (ch)	530	1070	330	570	170	370
Resolution	50%	24%	21%	11%	9.5%	6.5%

Table 6.1: Measured resolution for single photons with various photocathode voltages. The AD voltage was 245 V or 382 V.

6.2.2 Pulse-height spectra at various voltages to an avalanche diode

The pulse-height spectra for single photons were measured at various AD voltages from 245 V to 382 V, with the photocathode voltage fixed at -8 kV. Fig. 6.13 displays the results. The increase in the peak channel with the AD voltage can be simply explained by an increase in the avalanche gain. Surprisingly, the resolution is improved with the AD voltage, as shown in Fig. 6.14. This may be explained by the behavior of the avalanche gain on m_{EB}, as shown in Fig. 6.8. The event with a higher (lower) m_{EB} due to a fluctuation tends to have a larger (smaller) saturation in the avalanche multiplication process, and thus produces a relatively smaller (larger) gain there. The compensation could be more significant for a higher AD voltage, as shown in the figure. Accordingly, the overall gain could fluctuate less, and the pulse-height resolution is better for a higher AD voltage.

6.2.3 Pulse-height spectra for multi-photons

With the same setup, the light power was increased and the pulse-height spectra for multi-photons were studied. The AD voltage was 382 V, and the photocathode voltage was -8 kV or -9 kV. The results are shown in Fig. 6.15, where the peak for single photoelectrons is normalized to 500 ch. As shown, peaks corresponding to 1 to 5 electrons from the photocathode are clearly identified. They appear to be narrower at a photocathode voltage of -9 kV than at -8kV, because of the smaller loss fluctuation in the surface dead layer, as described in section 6.2.1. The resolutions for a single photon with these conditions are listed in Table 6.1.

6.2.4 Pulse-height linearity

The output pulse-height linearity of the HPD-16×2 was studied by varying the input light power with calibrated neutral density (ND) filters. The photocathode voltage was -8 kV, and the AD voltage was 382 V. The measured pulse-height spectra for high-density ND filters (ND 1 to ND 3) are shown in Fig. 6.16, and those for low-density ND filters (ND 4 to ND 6) are shown in Fig. 6.17. The horizontal scale differs by a factor of 30 between Figs. 6.16 and 6.17. The number of photoelectrons for each condition was estimated by integrating the observed spectrum and dividing it by an integral corresponding to single photoelectrons. The result plotted in Fig. 6.18 proves good linearity of up to 230 photoelectrons. This implies that the linearity of the relation between the intensity of light and the number of detected photoelectron is preserved even with the space-charge effect on the avalanche gain. This also suggests that the space-charge effect is quite localized, as discussed in section 6.1.3.

6.2.5 Noise factors of a hybrid photo-detector and an avalanche diode

Using the pulse-height spectra, the noise factor of an HPD was studied. The noise factor of the HPD (F_{HPD}) is defined by

$$F_{HPD} = \left(\frac{A_{in} / \sigma_{in}}{A_{out} / \sigma_{out}}\right)^2, \tag{6.5}$$

where the peak-output signal (A_{out}) and its standard deviation (σ_{out}) are derived from the pulse-height spectrum. The number of photoelectrons (A_{in}) entering the AD can be calculated from the peak-output signal (A_{out}); its deviation (σ_{in}) is taken to be the square root of A_{in}, considering a Poisson distribution.

The pulse-height spectra for approximately 200 photoelectrons were measured at AD voltages from 245 V to 382 V, with the photocathode voltage being fixed at -8 kV. The results are summarized in Table 6.2. As expected, F_{HPD} is close to the theoretical minimum of unity. This is because the gain in the first stage of multiplication by electron bombardment is higher than 1000, and the statistical fluctuation there is small. The noise factor decreases with the AD voltage, because of the compensation effect described in section 6.2.2.

For a reference, the noise factor of the incorporated AD itself was measured. The photocathode voltage was set to 0 V, and pulsed light transmitting through the photocathode was used. The result is also given in Table 6.2. It can be seen that the noise factor of the AD is much larger than the theoretical minimum of unity, and increases further with the AD voltage. This is a typical characteristic of the avalanche photodiode (APD) used for photon detection.

AD voltage	245 V	302 V	354 V	382 V
Avalanche gain (for light)	21.1	33.4	66.9	126
F_{HPD}	1.15	1.07	1.07	1.02
F_{AD}	2.44	2.44	3.10	4.17

Table 6.2: Estimation of the noise factor of an HPD and incorporated AD.

A theoretical treatment of the noise factor of an HPD is discussed. As given in Appendix 3, the noise factor (F_{HPD}) for two-stage cascade multiplication is expressed as

$$F_{HPD} = F_{EB} + \frac{F_{AD} - 1}{m_{EB}}, \tag{6.6}$$

where F_{EB} is the noise factor for electron-bombarded multiplication, and F_{AD} is for avalanche multiplication. From this equation, it is clear that the effect of the second stage, i.e. the noise factor

of the AD, is reduced by the gain in the first multiplication (m_{EB}).

Among the factors in equation 6.6, F_{EB} can be estimated by

$$F_{EB} = 1 + \frac{\sigma_{EB}^2}{m_{EB}^2}. \tag{6.7}$$

The measured resolution of 21% for single photons at a low AD voltage is considered to be σ_{EB}/m_{EB}. Then, F_{EB} turns out to be 1.05. On the other hand, F_{AD} is 3.1 at an avalanche gain of 67. Assuming an m_{EB} of 1190, the noise factor of the HPD (F_{HPD}) is estimated to be 1.05, and is thus consistent with the measured one.

6.3 Time response

6.3.1 Time response for impulse light

The time response of the HPD-16×2 was measured with the experimental setup shown in Fig. 6.19. The light from a pulsed laser diode (LD) at 405 nm was focused onto one pixel of the HPD. The pulse width was 95 ps, short enough to be considered to be an impulse. The applied voltages were -8 kV on the photocathode and 302 V on the AD, giving a total gain of 3.4×10^4. The output signal from the HPD was measured by an oscilloscope (Infiniium, Agilent), the bandwidth of which was 1.5 GHz and the input impedance was 50 Ω. The observed signal is shown in Fig. 6.20. The rise and decay times are 1.1 ns and 1.7 ns, respectively. As presented in section 4.4, the rise and decay times of the preliminarily tested ADs were 1.0 ns and 0.8 ns, respectively, when 300 V was applied. It appears that the time response is slightly worse for the HPD than for the AD alone possibly due to the assembling method using flip-chip bonding, which gives an additional stray capacitance on the connecting board. The observed response of this HPD is still fast enough for most applications.

6.3.2 Single-photon response

The time response for a single photon was measured using a high-speed amplifier (Miteq, AU-1494-300, 300 MHz, Gain: 60 dB) and an attenuator (1/10). The light source was an LED operated in the single-photon level. The output signal for a single photon is shown in Fig. 6.21, where 64 signals were averaged on the oscilloscope. Both the rise and decay times were 1.1 ns. The noise was measured in the real-time mode of an oscilloscope to be 5 $mV_{p\text{-}p}$, which should be compared with a signal level of 18 mV for a single photon. This clearly shows that the HPD is capable of detecting a single photon with a fast response, owing to the additional avalanche gain and the low capacitance due to the small size of each pixel. An HPD without avalanche gain can not

detect a single photon at this speed.

As a next step, timing resolution for a single photon was measured with the setup shown in Fig. 6.22. A pulsed LD, with a pulse width of less than 50 ps and a wavelength of 780 nm, was used for the light source. After the two-stage amplifier (Miteq: AU-1494-300 and HP8447F: 1.5 GHz), the output signal was fed to a constant-fraction discriminator (CFD, ORTEC 583) to generate a start signal for the time-to-amplitude converter (TAC, ORTEC 547). The trigger signal from the LD driver was used as a stop signal of the TAC. The TAC output was recorded by a multi-channel analyzer (MCA, Laboratory equipment co., MCA/AT). From the result shown in Fig. 6.23, the timing resolution for a single photon is estimated to be 89 ps in standard deviation. This timing response is as fast as the transit-time-spread (TTS) of commercially available fast PMTs. A simple estimation of the transit time of electrons from the photocathode to the AD is given in Appendix 4. The result is consistent with the timing response shown above.

6.4 Performance as a multi-pixel photon sensor

6.4.1 Uniformity

The output current of the HPD-8×8 was measured, while a light spot of 0.94 mm in diameter was focused onto the center of each pixel and scanned pixel by pixel. The wavelength was 500 nm. The photocathode voltage was -8 kV, and the AD voltage was 325 V. Under this condition, the m_{EB} was 1190, the avalanche gain 51, and the total gain 6.1×10^4. The result is shown in Fig. 6.24. The convention used to specify each pixel is shown in Fig. 6.1, because the lower right is pixel (1,1) and the upper left is pixel (8,8). The standard deviation of the gains among the 64 pixels was found to be 7.9%, when the average output currents of the efficient pixels were normalized to 100%. Hereafter, the standard deviation was normalized to the average output signal like this. The smallest output was 75% of the largest. This uniformity is better than that of a commercially available multi-pixel PMT, where the smallest is typically 30% of the largest one.

To analyze the source of non-uniformity, individual factors, such as the photocathode sensitivity, m_{EB} or avalanche gain, were studied. To measure the photocathode sensitivity, the cathode and the anode of the AD were connected electrically, and the HPD was operated as a phototube. With -1 kV on the photocathode, the output current was measured, as shown in Fig. 6.25. The photocathode sensitivity is almost flat over the effective area with a standard deviation of 1.6%.

To examine the uniformity of m_{EB}, the HPD was operated with a unit avalanche gain and its output was divided by the photocathode sensitivity. As shown in Fig. 6.26, m_{EB} was flat over the effective area, with its standard deviation being 1.3%. m_{EB} was determined by the energy of incident

electrons and the thickness of the surface dead-layer of the AD. The electron energy was constant within 0.2%, being dominated by the stability of the photocathode voltage. The dead-layer thickness was determined by the semiconductor process, especially the production of the backside p+ layer. There is no reason for the thickness to have a large variation over an effective area of 16×16 mm^2. Consequently, m_{EB} is expected to be uniform, just as proven by measurements.

In order to study the uniformity of the avalanche gain, the HPD output obtained with an avalanche gain of 51 on average was divided by that measured with unity avalanche gain. As shown in Fig. 6.27, the standard deviation is 7.1%. From this analysis, it is found that the uniformity of the HPD is mostly determined by that of the avalanche gain in the AD. It can be improved if the AD gain, itself, is reduced. For example, the standard deviation in an AD of 5.3% operated at a gain of 30 is reduced to 2.4% for a gain of 10.

6.4.2. Cross talk for DC light

The cross talk between the pixels of the HPD-8×8 with a fiber-optic plate (FOP) was studied under DC light illumination. A light spot of 0.94 mm in diameter was focused onto the input surface of the FOP. The result is shown in Fig. 6.28. The cross talk was 1.3% from the closest pixels, and was less than 1.0% from the others.

One of the reasons for the cross talk is suspected to be an optical type in the FOP. In order to clarify this point, a light spot of 30 μm (FWHM) was scanned over a pixel of the HPD-8×8 (FOP window) and the HPD-16×2 (Glass window) in steps of 50 μm. The results are shown in Fig. 6.29. The response with the FOP window changed gradually, whereas it was rather sharp with a glass window. For example, at 0.5 mm apart from the edge of the pixel, the cross talk was 2.3% and 0.8% for the FOP window and the glass window, respectively. The cross talk for the glass window decreased to 0.5% when the spot was moved to 1 mm from the pixel edge, while it was 1.4% for the FOP. Accordingly, cross talk of about 0.9% is attributed to the FOP window character. A residual cross talk of 0.5% is considered to come from backscattered electrons, as discussed in section 6.5.

6.4.3 Cross talk for pulsed light

A spot of pulsed light was focused on a pixel of the HPD-8×8, and output signals from the irradiated pixel (3,5) and the next one (3,6) were measured by an oscilloscope. The output pulses are compared in Fig. 6.30. Approximately 15% of the signal appears on the next pixel, showing a differential form. Therefore, the capacitive coupling of the signals seems to be a major source of cross talk. The long signal path of 20 mm from the pixel to the output pin with a 0.2 mm separation in some place is considered to be the main contribution of the capacitance. Since the

studied pixels were in the middle of the effective area, and a path length of 20 mm was the longest, the result given here shows the worst case for the HPD.

6.4.4 Low-gain zone between pixels

The low-gain zone between pixels was investigated by scanning over the border of two adjacent pixels with a light spot of 30 μm in diameter. HPD-8×8 was operated at an m_{EB} of 1190, an avalanche gain of 34 and a total gain of 4.0×10^4. The result is shown in Fig. 6.31. If a low-gain zone is defined as the area where the gain is less than 50% of the effective area, it extends by 120 μm, slightly wider than the design goal of 100 μm. A low-gain zone was simulated, where a step-like gap was assumed while taking the size of the light spot into account. The result is also shown in Fig. 6.31. The best fit was obtained for a gap of 120 μm and a sensitivity of 25% of the normal gain, in sufficiently good agreement with the measurement.

6.5 Performance in a magnetic field

6.5.1 Output current for DC light

In a magnetic field, the output currents from a pixel (4,8) and an adjacent one (5,8) of the HPD-8×8 were measured under constant light illumination. The direction of the magnetic field was set at 0 and 30 degrees to the tube axis. The input side of the FOP window was masked by a light-shield tape to illuminate one pixel (4,8). The exposed area was 1.0×1.2 mm^2 on a pixel of 2×2 mm^2. An LED at 470 nm driven in the DC mode was used as a light source. An electromagnet was used to generate a magnetic field. The diameter of the pole was 400 mm, and the gap was 150 mm. The magnetic field was changed between 0 T and 1.5 T. HPD-8×8 was operated at an m_{EB} of 1190, an avalanche gain of 34 and a total gain of 4.0×10^4. The experimental condition is illustrated in Fig. 6.32.

The result for a magnetic field parallel (0 degree) to the tube axis is shown in Fig. 6.33. It clearly shows that the HPD can be operated at a magnetic field of at least up to 1.5 T. The observed 10% rise of the output from 0.1 T to 0.6 T is considered to be the reentry of backscattered electrons to the pixel. The maximum reach of the electrons backscattered from the input point is 5 mm without a magnetic field, while it becomes very short in high magnetic fields. Those backscattered electrons would contribute to the signal in the next pixel without a magnetic field. As a matter of fact, the output signal of the next pixel (5,8) changed from 1.4% under zero field to 0.8% at 1.5 T. The difference, 0.6%, is likely to be the contribution of the backscattered electrons at zero magnetic

field.

The result for a magnetic field inclined by 30 degrees to the tube axis is shown in Fig. 6.34. The output current from the irradiated pixel (4,8) rapidly decreased with the field strength, while a quick increase was observed in the next one (5,8). This was caused by a shift of the electron trajectory by the Lorenz force. This effect was calculated in terms of the shift of the trajectory in the *x* direction as a function of the distance in the *z* direction, as shown for the different magnetic fields in Fig. 6.35. See Fig. 6.32 for the geometry and Appendix 5 for the calculation. The position shift rapidly increased with the magnetic field from 0.1 T to 0.3 T, and remained almost constant at 1.43 mm with a magnetic field higher than 0.5 T at a distance of 2.5 mm in the *z* direction, which corresponds to the photocathode-AD distance. It is evident that the trajectory with a shift of 1.43 mm can reach the next pixel, as observed in the experiment. The calculation can thus explain the experimental result.

6.5.2 Pulse-height spectrum

The pulse-height spectrum was measured in a magnetic field parallel to the tube axis under the illumination of pulsed light from an LED. A charge-sensitive amplifier (Amptek, A250) was connected to the irradiated pixel, and the spectrum was stored in a multi-channel analyzer. The pulse-height spectrum for a few photons is shown in Fig. 6.36. A slightly larger number of photons was observed for 1.5 T case. This phenomenon can again be explained by the reentry of backscattered electrons to the pixel due to the magnetic field.

6.6 Stability in long-term operation

To check the stability of an HPD, a long-term illumination test was performed with an HPD-16×2. The applied voltages were -8 kV on the photocathode and 250 V on the AD. In this condition, m_{EB}, the avalanche gain and the total gain were 1300, 18 and 2.3×10^4, respectively. The input light power was adjusted to be an output current of 37 μA for the sum of all pixels. This corresponds to an irradiated light power of 2.5×10^{-8} W, a power density of 2.0×10^{-10} W/mm^2, and a photon number of 1.7×10^9 photons/pixel/s. Under this condition, operation for 100 hours, corresponding to an output charge of 0.42 C/pixel, was performed.

The changes in the performance after the operation are listed in Table 6.3. The variations of the QE was 1.05; m_{EB}, 0.97; avalanche gain, 1.02; total gain, 0.99; and leakage current, 0.99. It can be concluded that there was no significant degradation in the performance during operation. If an experiment under 10 photoelectrons/pixel/event and an event rate of 100 kHz on average, or 1×10^6

photoelectrons/pixel/s is assumed, the output current would be 4.0 nA for a total gain of 2.5×10^4. Thus, the output charge of 0.42 C in this test corresponds to 29,000 hours of operation time. This is long enough for real experiments. It should be noted that the selected structure of the AD of backside illumination is quite stable for electron irradiation.

	Initial	After 100 hours of operation
QE at 420 nm	18.8%	19.8%
m_{EB} at -8 kV	1300	1260
Avalanche gain at 250V	17.7	18.1
Total gain	2.30×10^4	2.28×10^4
Leak current per pixel	0.78 nA	0.77 nA

Table 6.3: Change in the performance after operation corresponding to an output charge of 0.42 C/pixel.

6.7 Practical test

In order to demonstrate the capability of the HPD developed here to be used in a particle detector, it was integrated with a bundle of scintillating fibers, where a read out system for 64 pixels was also prepared. The test setup is schematically shown in Fig. 6.37. A bundle of the plastic scintillating fibers (Kuraray SCSF-78M, ϕ0.7mm), which emitted and transferred scintillation photons upon the passage of charged particles, was directly connected to the FOP window of the HPD. The peak wavelength in the emission spectrum was 430 nm. The cross section of the fiber bundle was 16×16 mm^2, which matched to the effective area of the HPD, and the length was 200 mm. A mirror was put on the other end of the scintillating fibers to reflect photons to the HPD. The applied voltages were -8 kV on the photocathode and 315 V on the AD; m_{EB}, the avalanche gain and the total gain were 1190, 44 and 5.1×10^4, respectively. All 64 pixels of the HPD were connected to readout circuits, which consisted of a front-end chip (IDE, VA32_HDR2), a control box to adjust the level of the signal, and an analog-to-digital converter (ADC) board (National instruments, PCI-6111E) mounted on a personal computer. The front-end chip had 64 charge-sensitive amplifiers and shapers. The output signals from the shapers were sampled and held, and sequentially read out by a multi-plexer. Since a trigger generator followed the front-end chips, the readout circuits were operated by the self-trigger mode.

Prior to a measurement of cosmic-ray muons, the combination of the HPD and the readout circuit was evaluated. A pulsed LED was used as a light source, and the pulse-height spectrum for a few photoelectrons was measured. The result shown in Fig. 6.38 clearly demonstrates peaks corresponding to one and two photoelectrons. The output voltage for one photoelectron

corresponds to 12 mV. The noise of the system can be derived from the spread of the pedestal to be 1.2 mV rms. Accordingly, the signal-to-noise ratio of the system for the detection of a single photon is 10.

The cosmic-ray tracks were recorded with the system in a self-trigger mode, as mentioned above. Three representative tracks are shown in Fig. 6.39. The columns and rows in the plots show the number of photoelectrons converted from the output voltages of the stored data. Pixels showing more than 5 photoelectrons are hatched. The tracks can be clearly seen in the plots. The output voltage per track length of 2 mm turns out to be 0.20V on average, corresponding to 17 photoelectrons from the photocathode. It is also seen that the noise level is well below that of a photoelectron. Thus, it is proven that the HPD developed in this study is really useable for photon-counting applications.

[REFERENCES]

[1] J. R. Fiebiger and R. S. Muller, “Pair-Production Energies in Silicon and Germanium Bombarded with Low-Energy Electrons”, J. Appl. Phys., Vol.43, pp.3202-3207, 1972

[2] F. Salvat et al., “PENELOPE – A Code System for Monte Carlo Simulation of Electron and Photon Transport”, NEA/NSC/DOC Vol.19, 2001

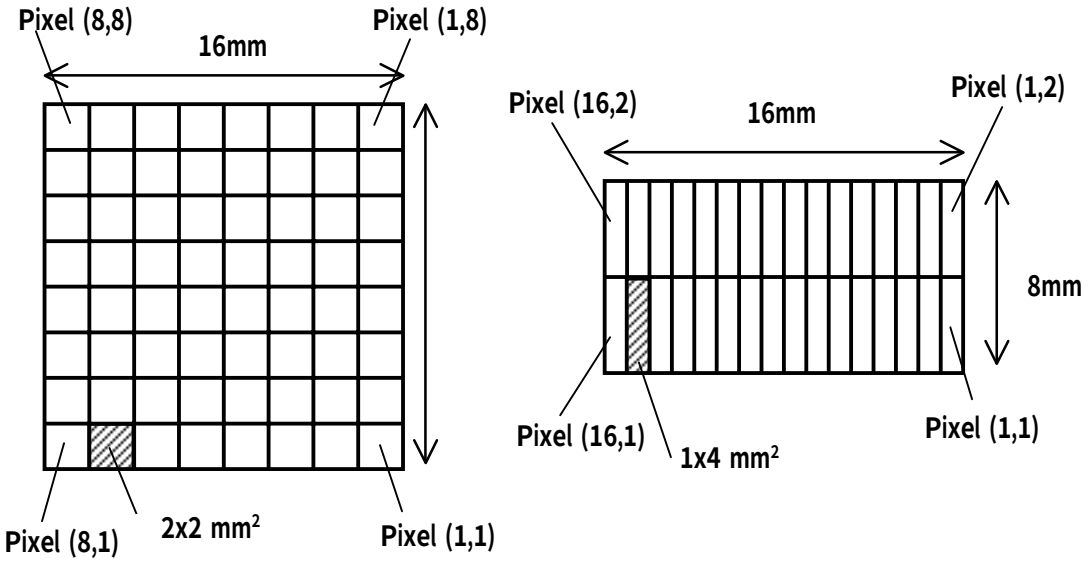

(a) 8×8 pixels **(b) 16×2 pixels**

Fig. 6.1: Pixel arrangement.

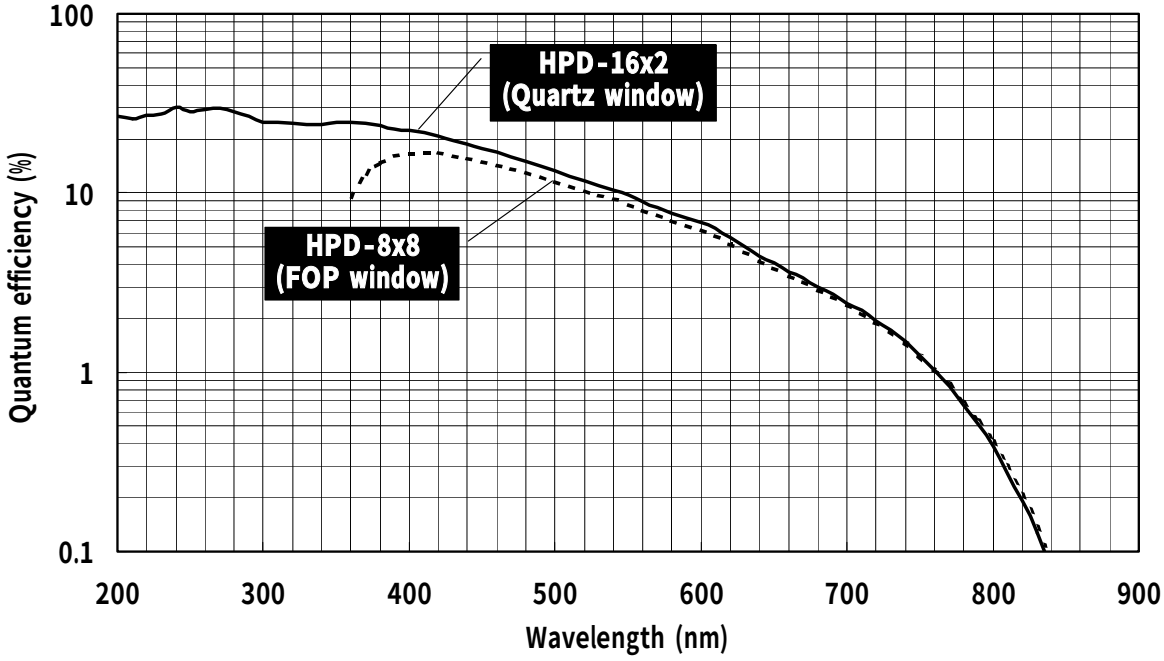

Fig. 6.2: Measured quantum efficiencies of HPDs as a function of the wavelength. The cutoff wavelength of the FOP window is determined by its transmission characteristic.

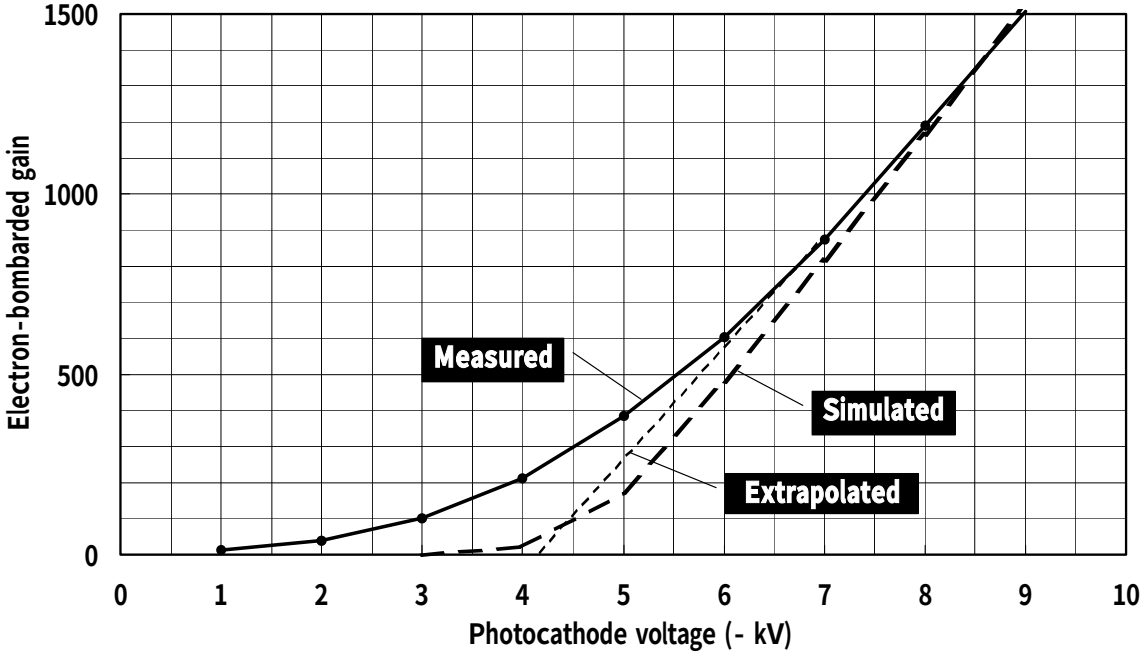

Fig. 6.3: Measured and simulated electron-bombarded gain as a function of the photocathode voltage. "Extrapolated" is given by equation 6.4 in the text.

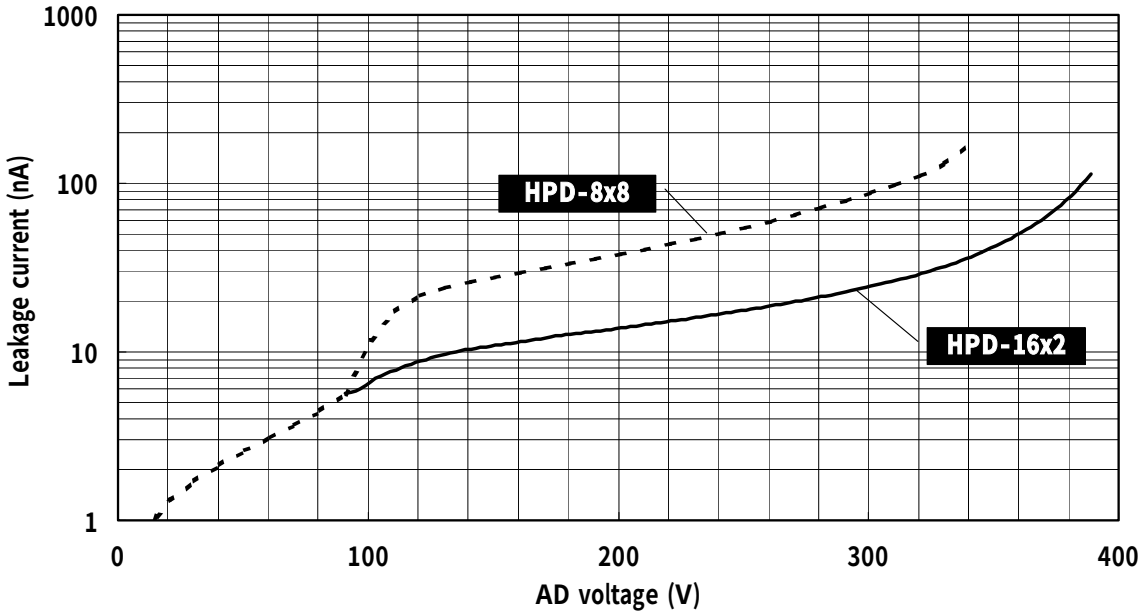

Fig. 6.4: Leakage currents of ADs as a function of the AD voltage. The currents from all good pixels (64pixels in HPD-8×8, 31pixel in HPD-16×2) are summed.

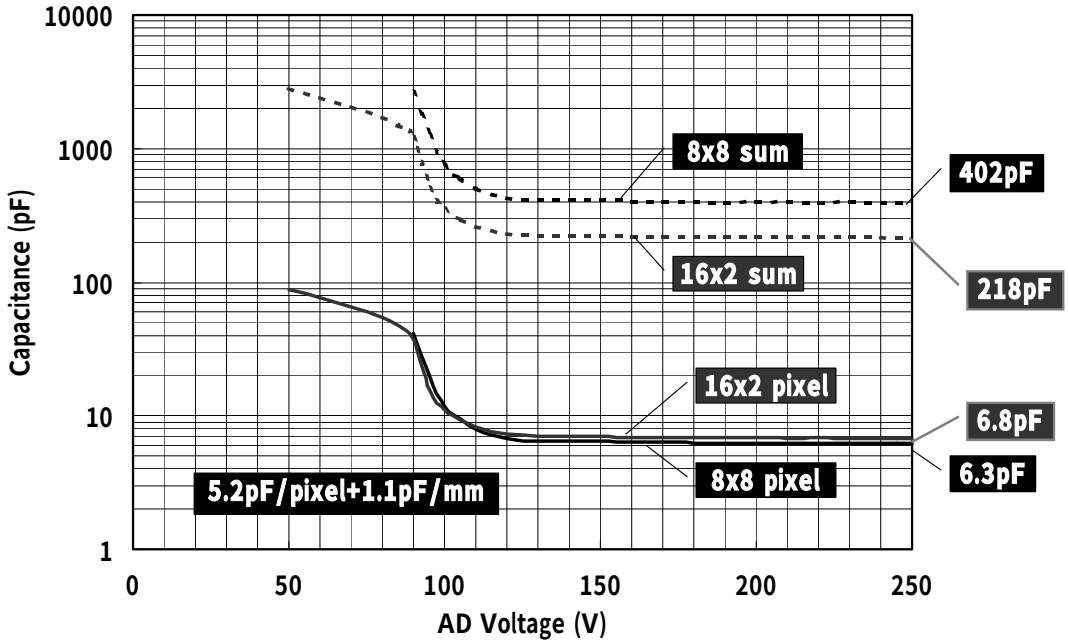

Fig. 6.5: C-V Characteristics of ADs incorporated in the HPD-8×8 and the HPD-16×2. The capacitance of a pixel was calculated from measurements for all of the pixels summed.

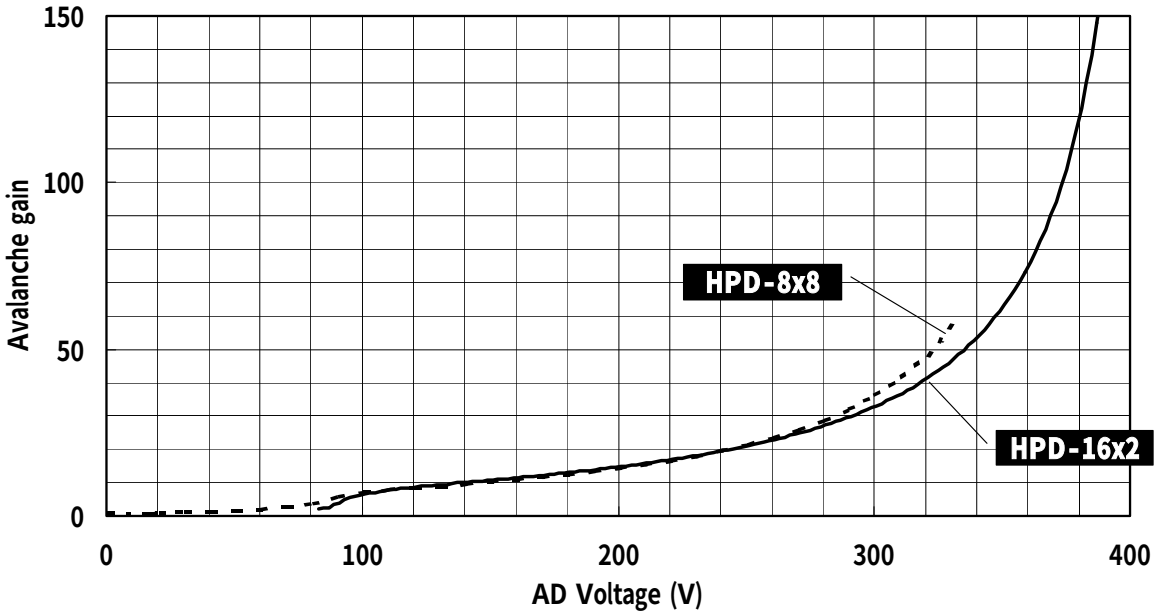

Fig. 6.6: Avalanche gains as a function of the AD voltage measured with light directly illuminated on the AD.

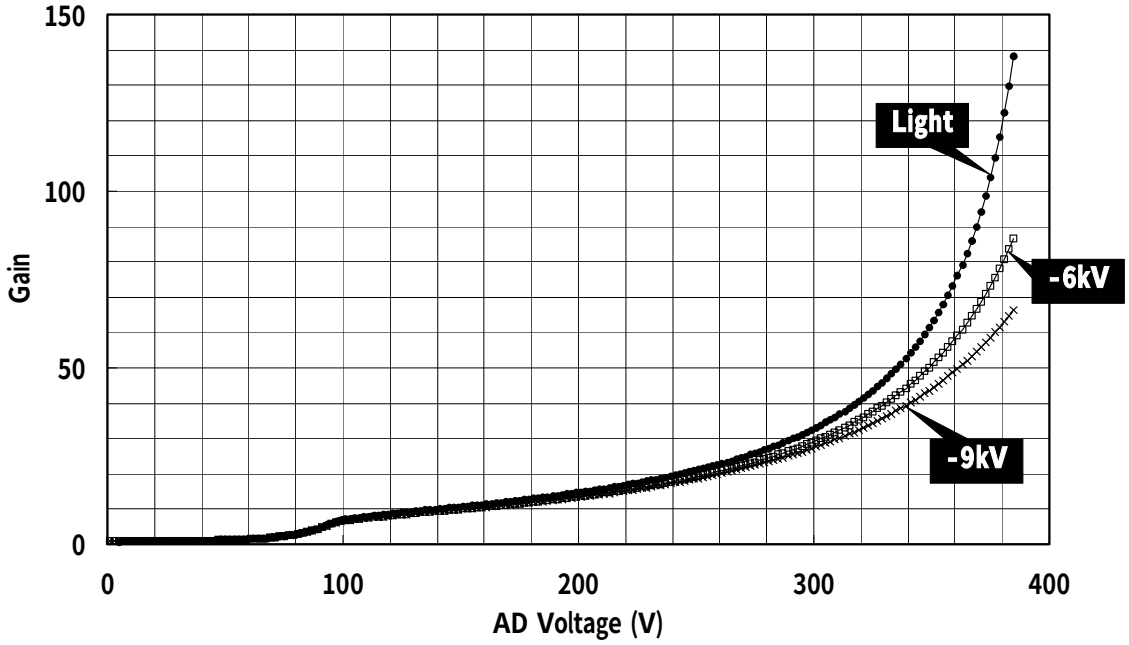

Fig. 6.7: Avalanche gain of HPD-16×2 under irradiation of electrons, as a function of the AD voltage. The photocathode voltage was varied as a parameter. "Light" is the gain shown in Fig. 6.6 as a reference of no electron-bombarded gain.

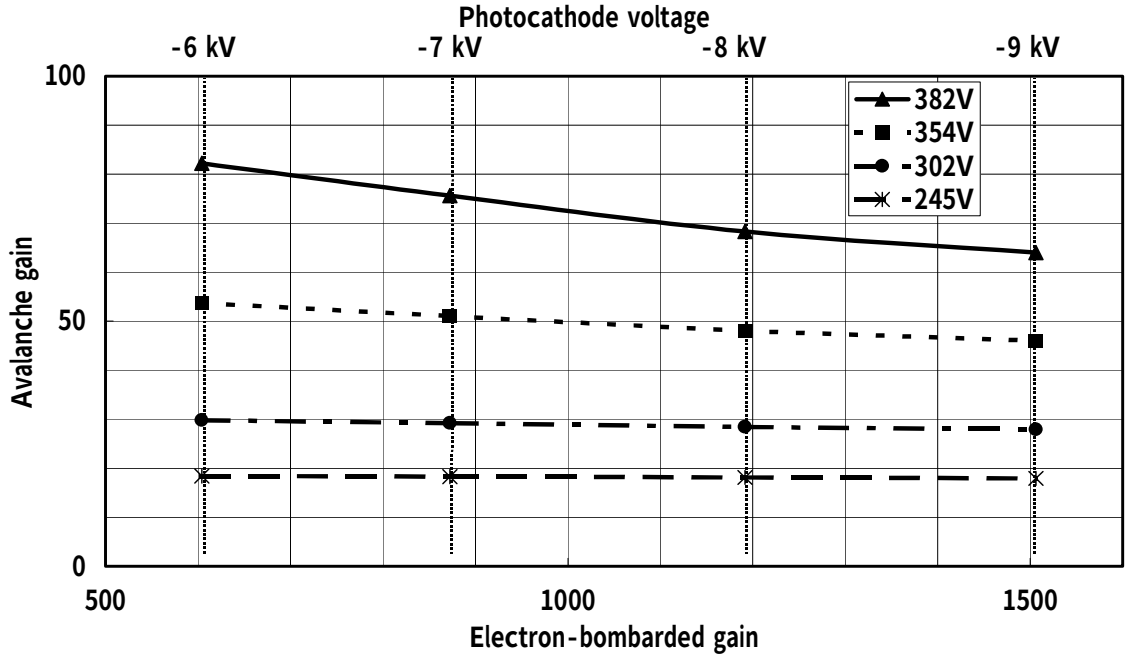

Fig. 6.8: Avalanche gain as a function of the electron-bombarded gain, measured for various AD voltages.

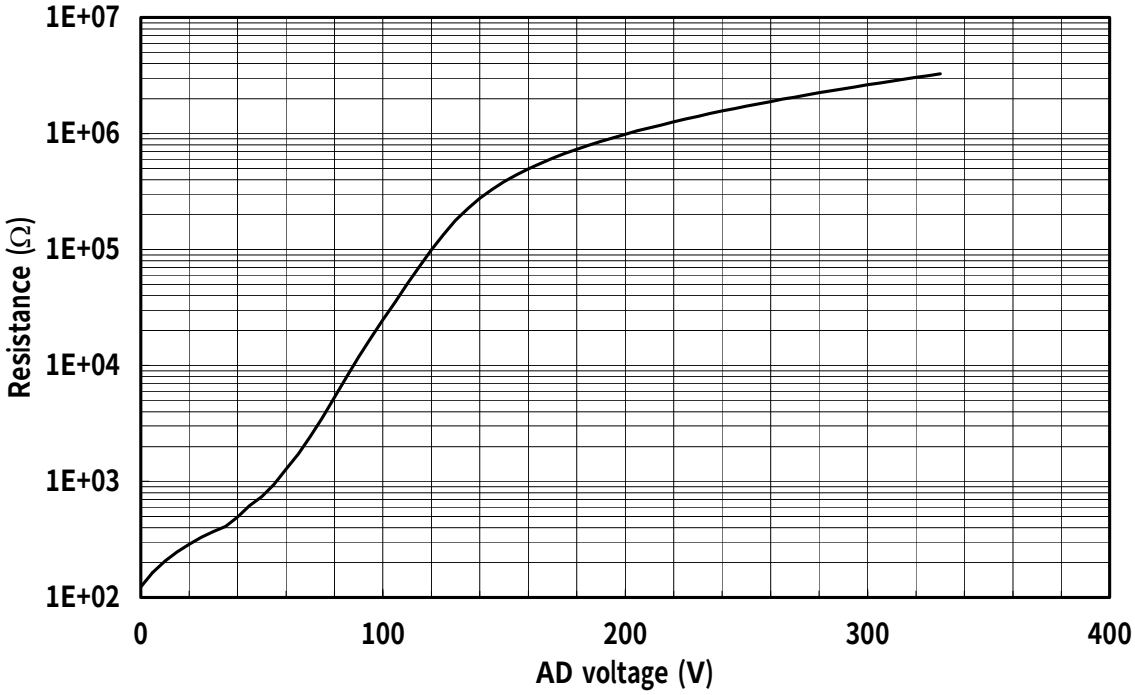

Fig. 6.9: Resistance between adjacent pixels as a function of the AD voltage.

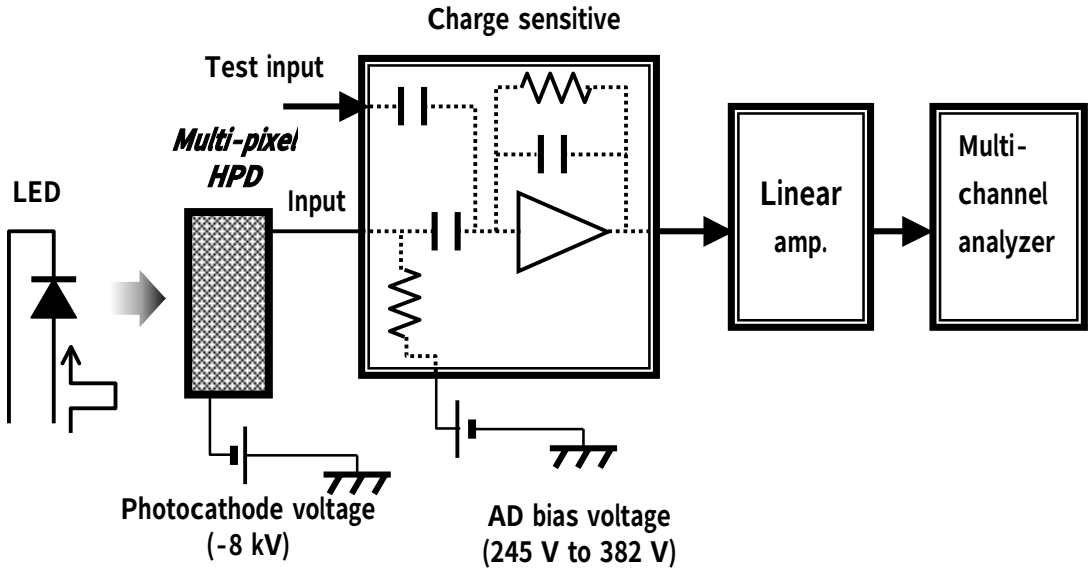

Fig. 6.10: Setup for measuring the pulse-height spectra.

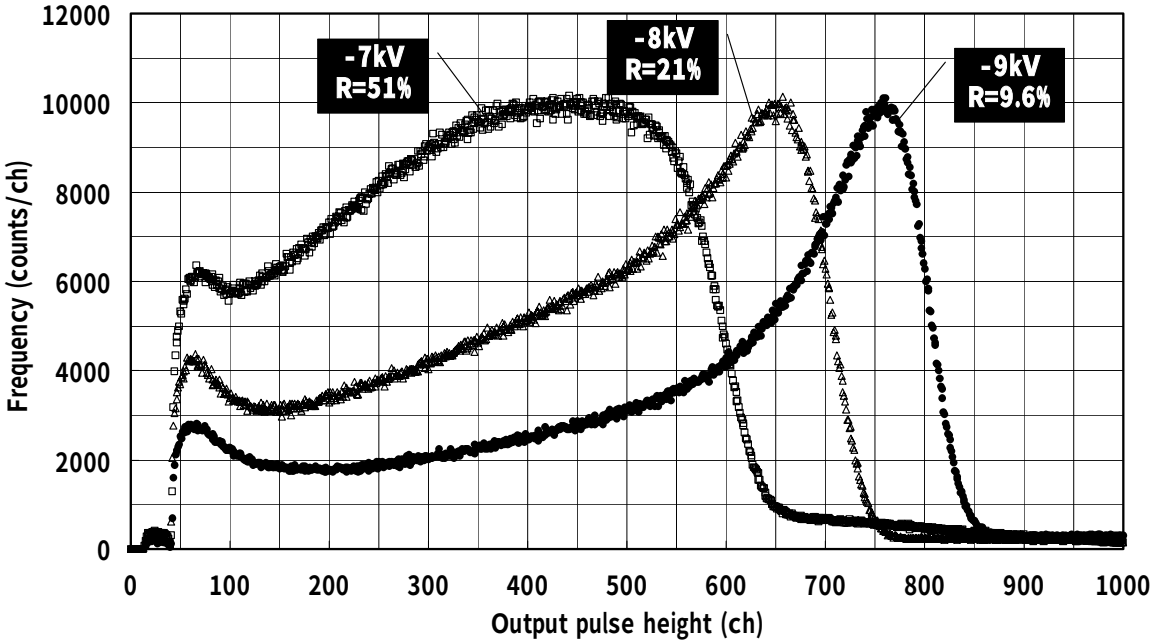

Fig. 6.11: Single-photon spectra of the HPD-16×2 for various photocathode voltages, with the AD voltage fixed at 245 V.

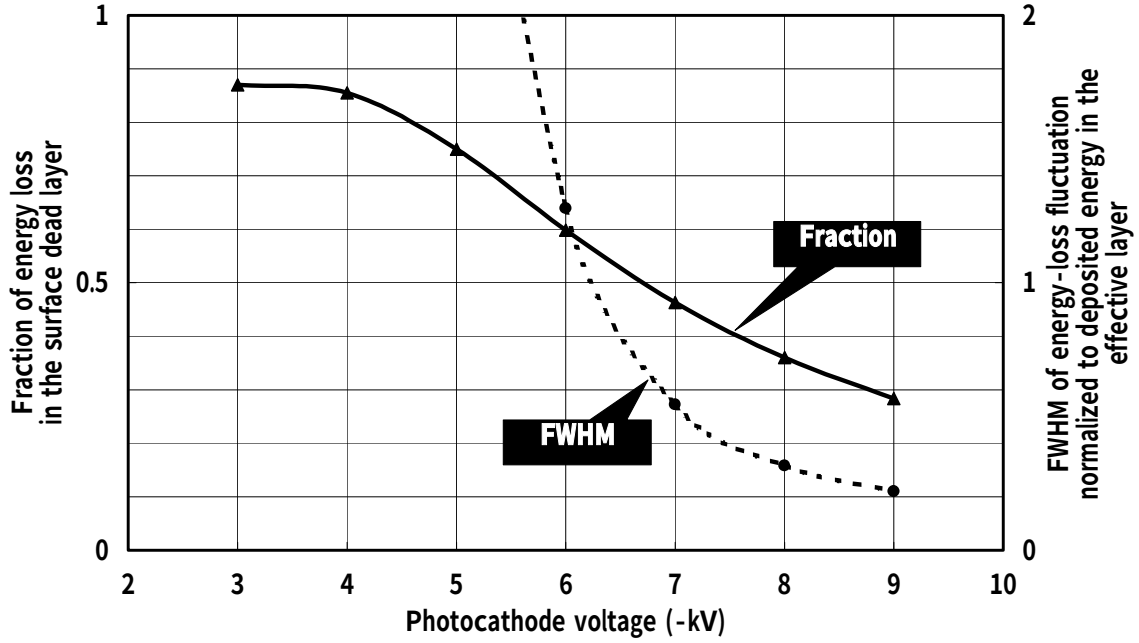

Fig. 6.12: Computed fraction of energy loss and its fluctuation (in FWHM) of electrons in the surface dead layer. A thickness of 235 nm was assumed for the dead layer, referring to the result obtained in Fig. 6.3.

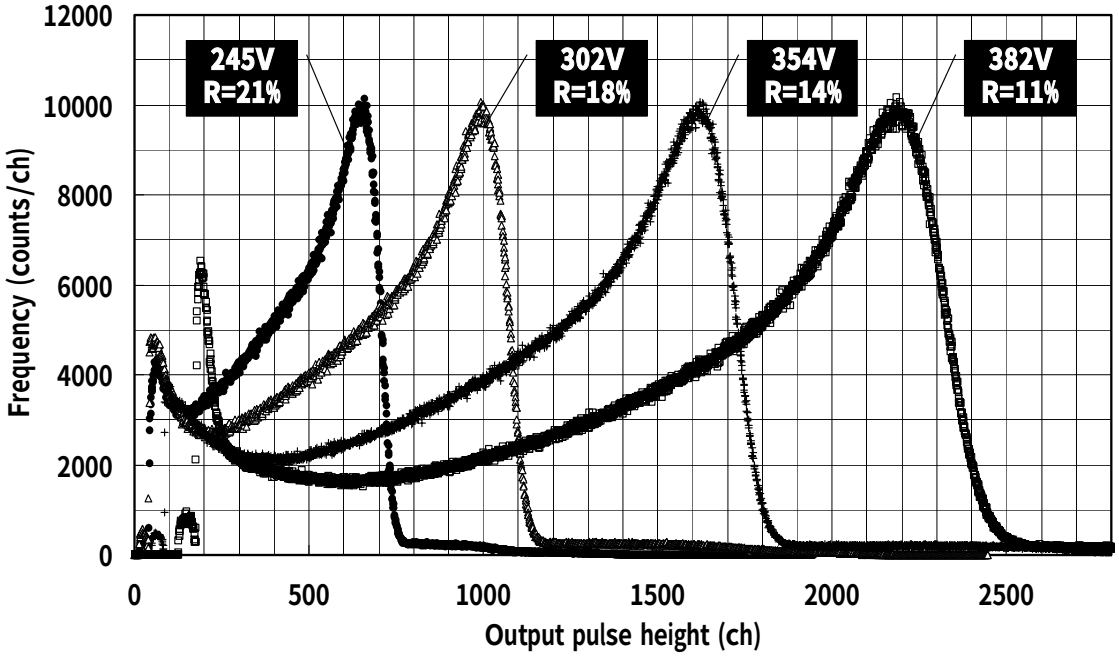

Fig. 6.13: Single-photon spectra of HPD-16×2 for various AD voltages, with the photocathode voltage fixed at -8 kV.

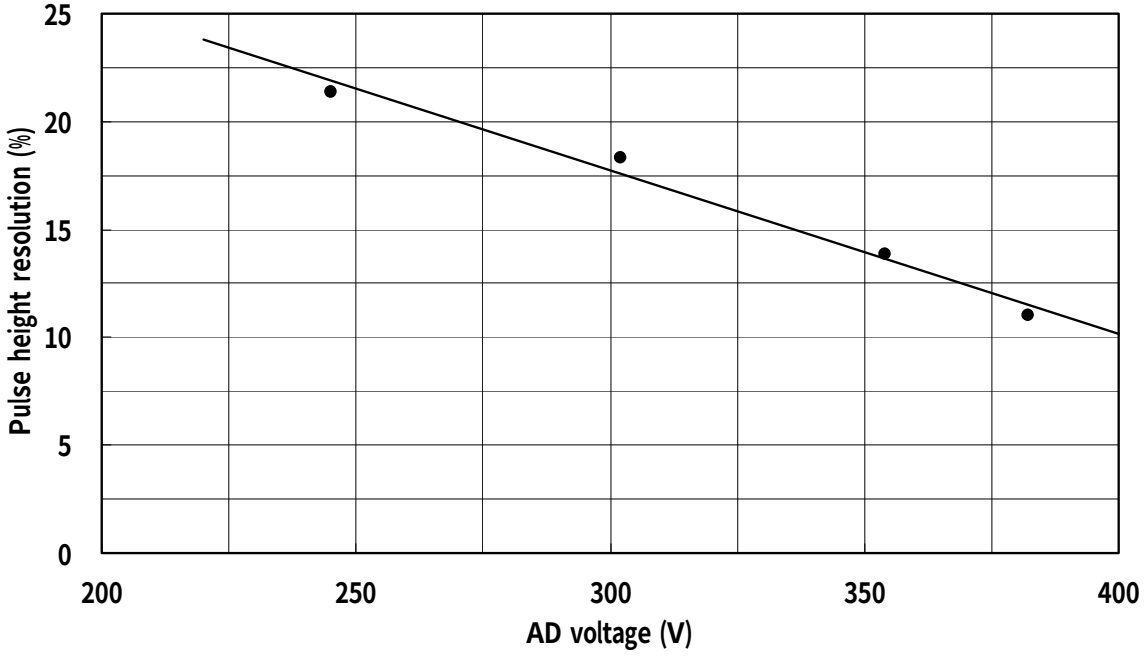

Fig. 6.14: Pulse-height resolution for a single photon as a function of the AD voltage.

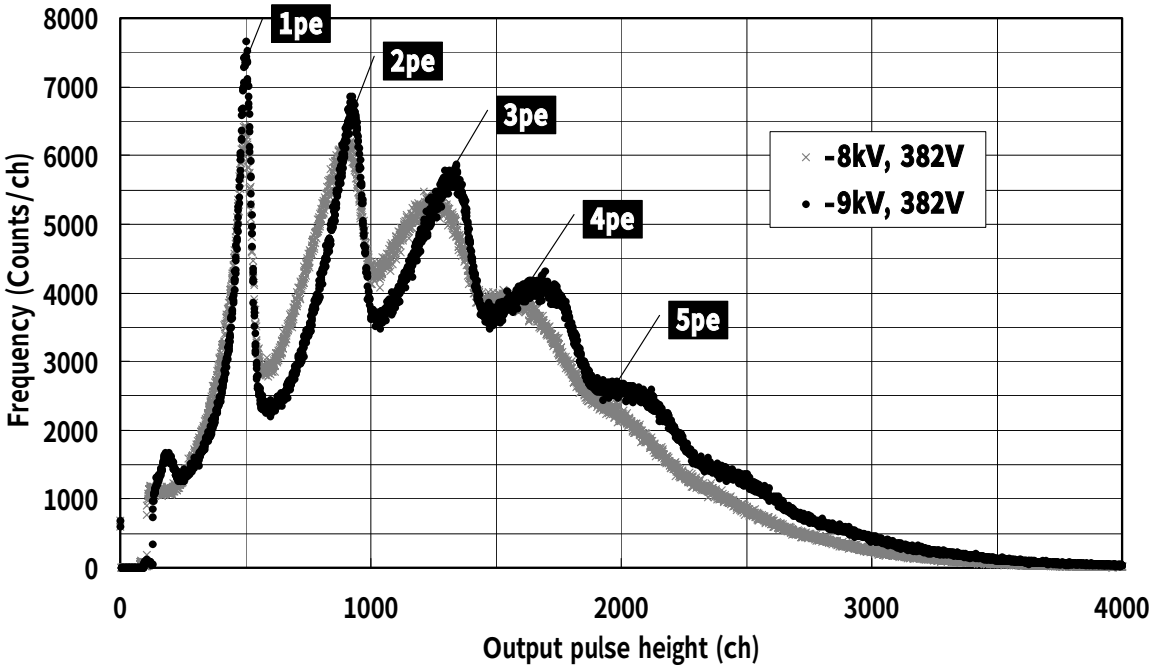

Fig. 6.15: Pulse-height spectra of the HPD-16×2 for multi-photons at a photocathode voltage of -8 kV and -9 kV with the AD voltage fixed at 382 V. The single-photoelectron peak is normalized to 500 ch.

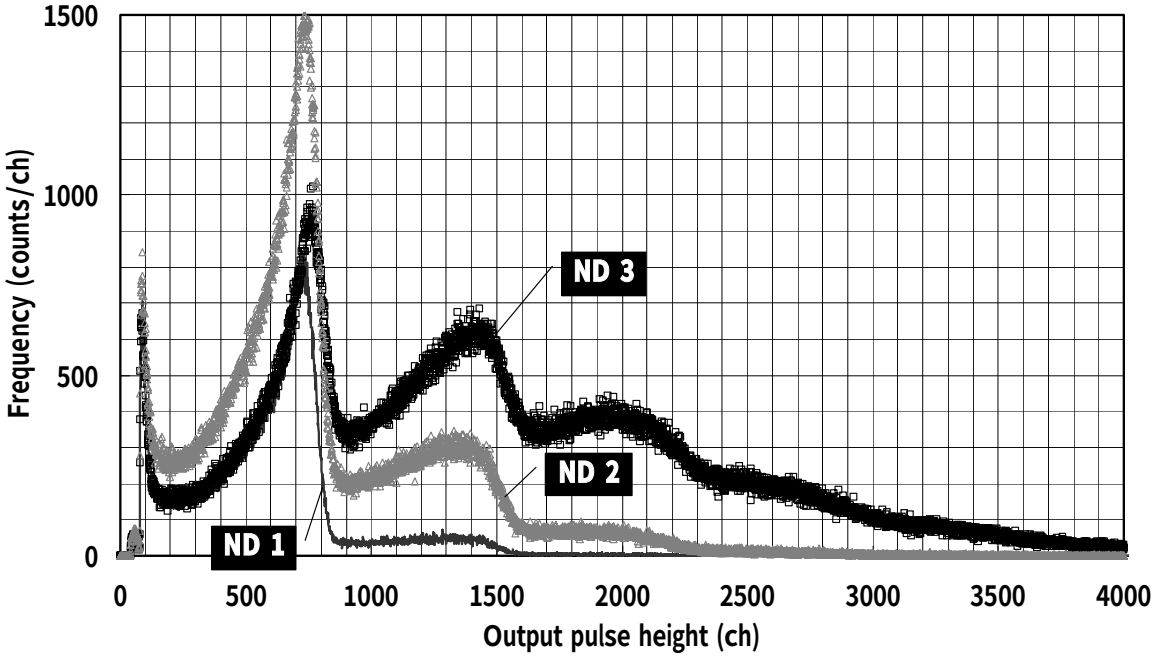

Fig. 6.16: Pulse-height spectra for relatively weak light, where ND 1 to ND3 are neutral-density filters used to vary the input light power.

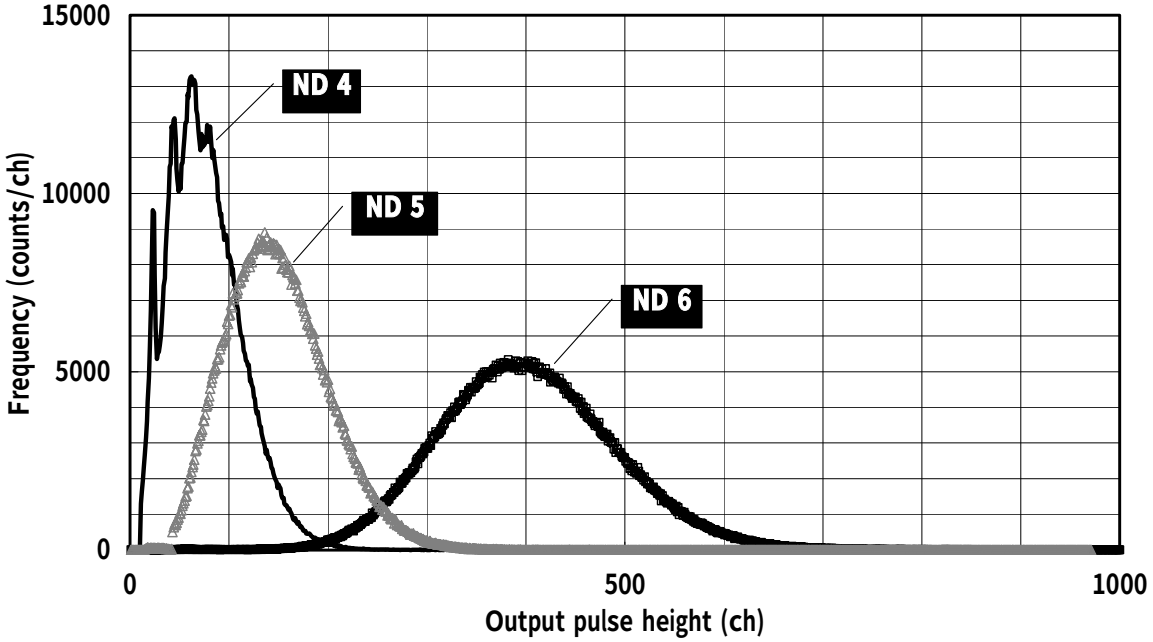

Fig. 6.17: Pulse-height spectra for relatively intense light, where ND 4 to ND6 are neutral density filters used to vary the input light power.

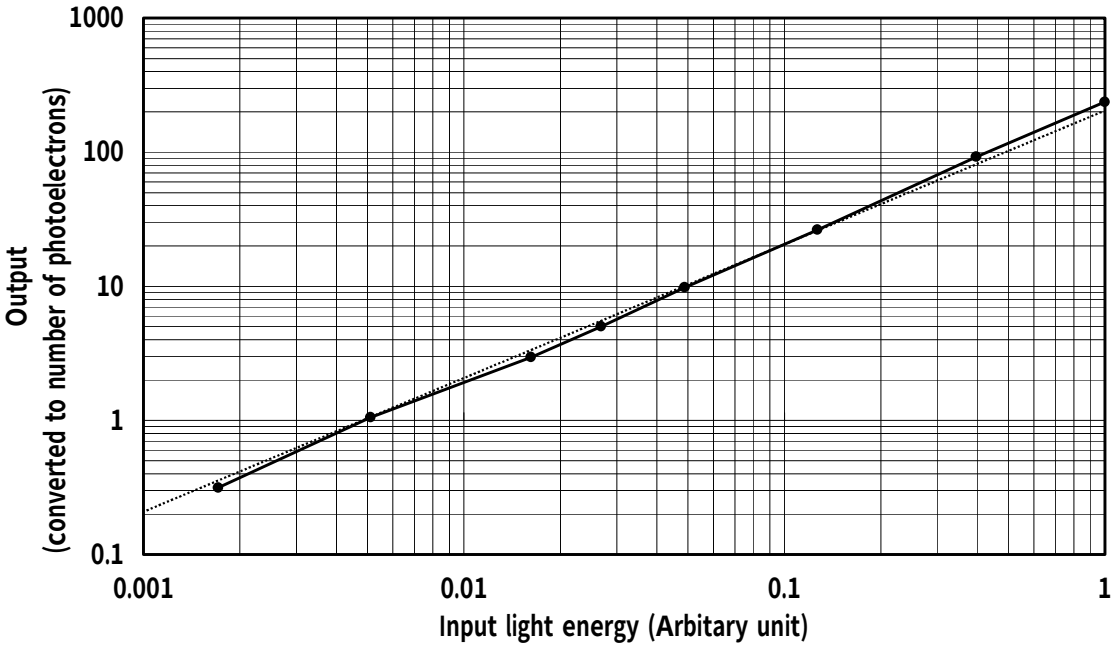

Fig. 6.18: Pulse linearity derived from the pulse-height spectra shown in Figs. 6.16 and 6.17. The horizontal axis shows the relative light power.

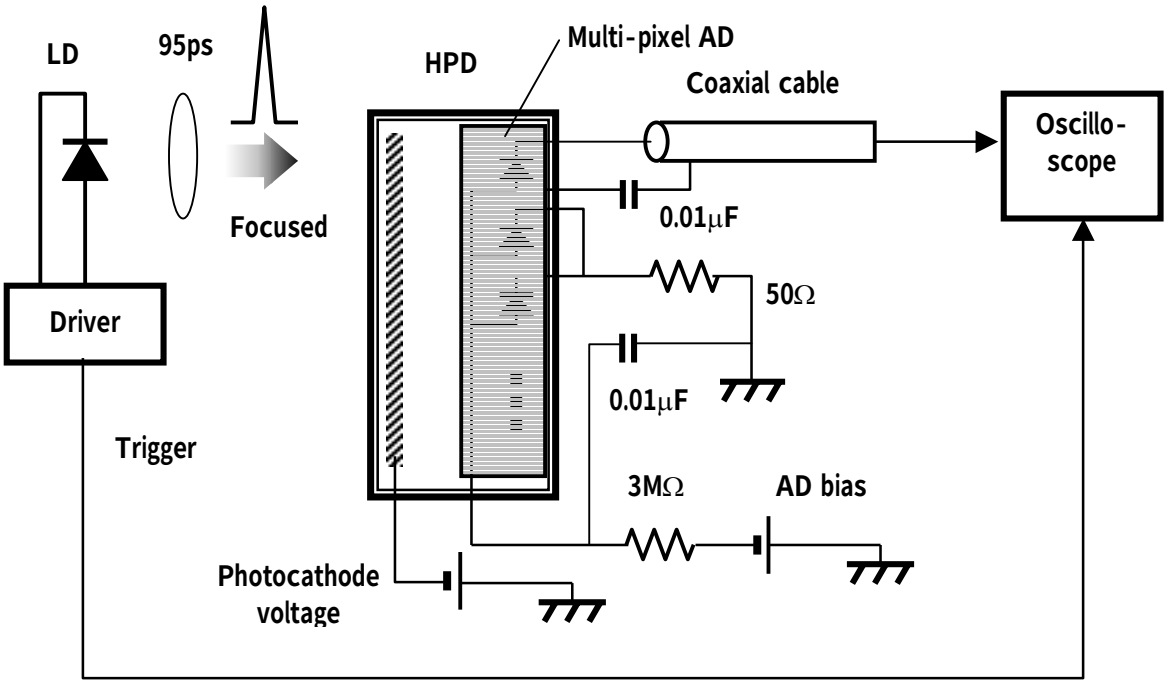

Fig. 6.19: Setup for measuring the time response.

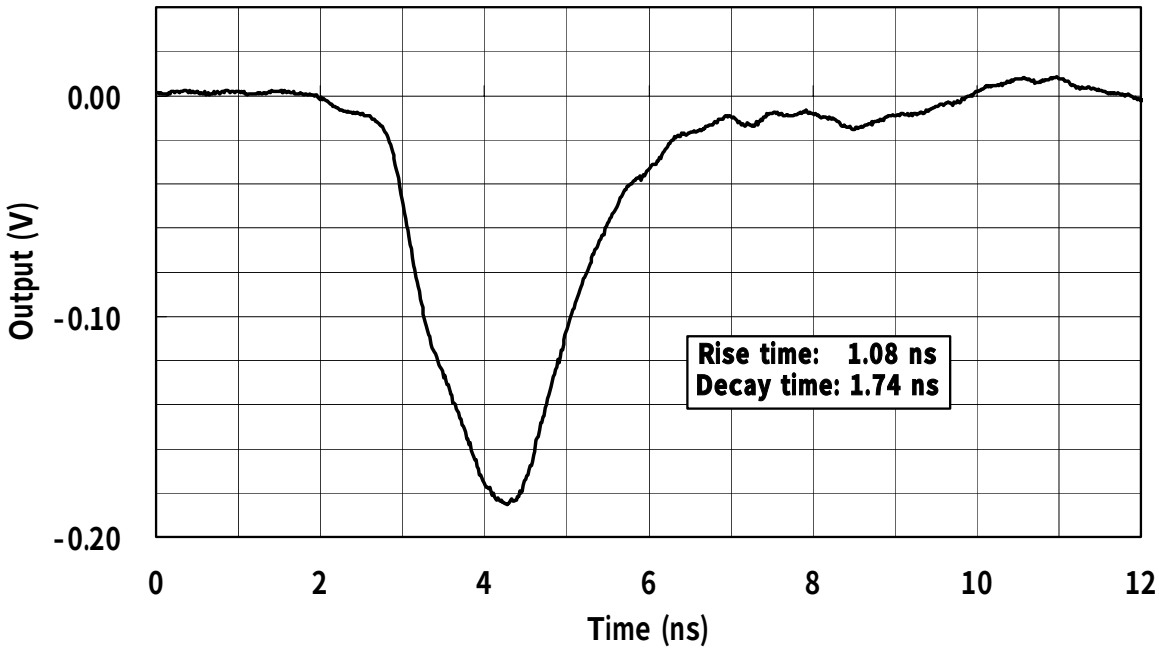

Fig. 6.20: Impulse responses of the HPD-16×2: -8 kV on the photocathode and 302 V on the AD.

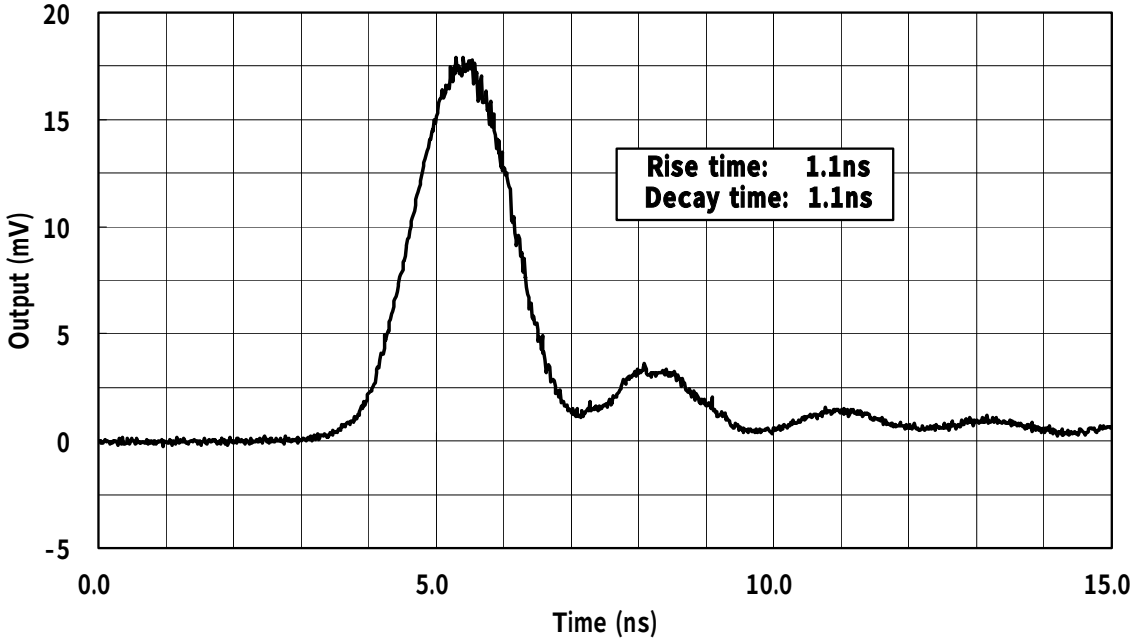

Fig. 6.21: Output signal for single photons with 64 signals averaged on an oscilloscope.

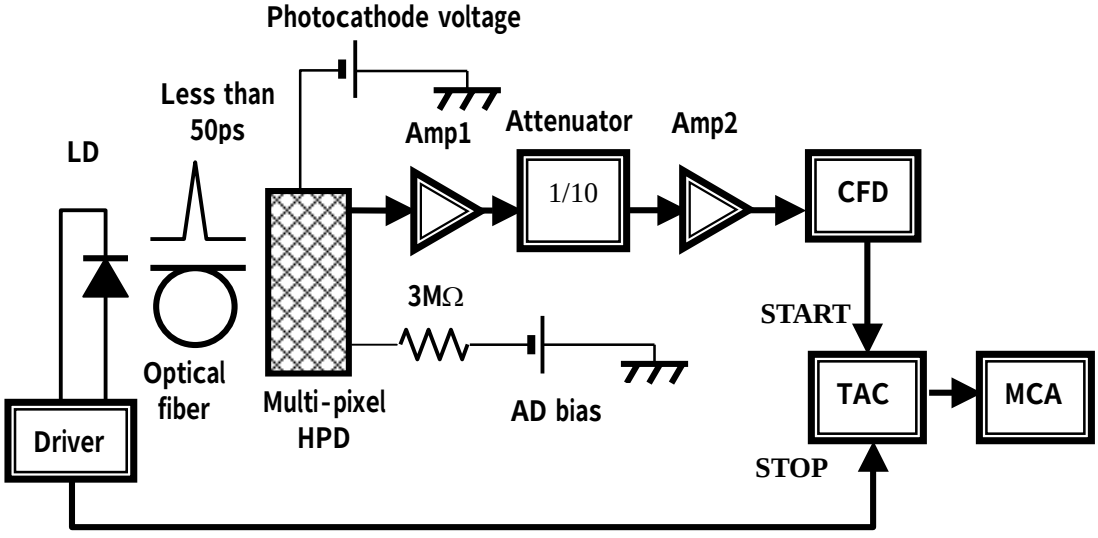

Fig. 6.22: Setup for measuring the timing resolution.

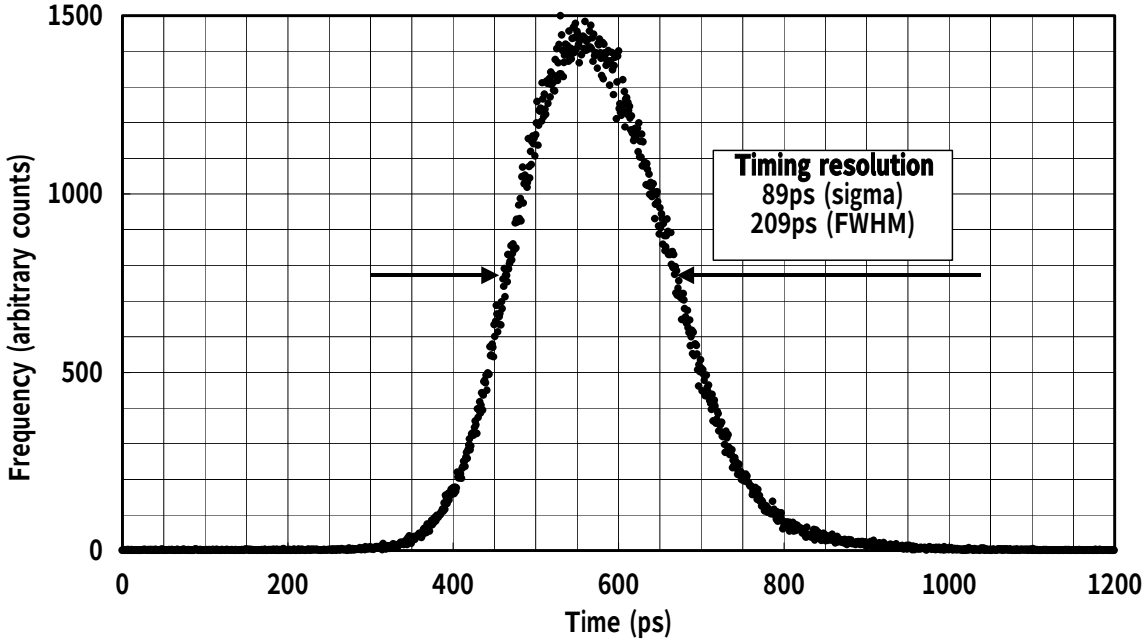

Fig. 6.23: Timing resolution of the HPD-16×2 for single photons.

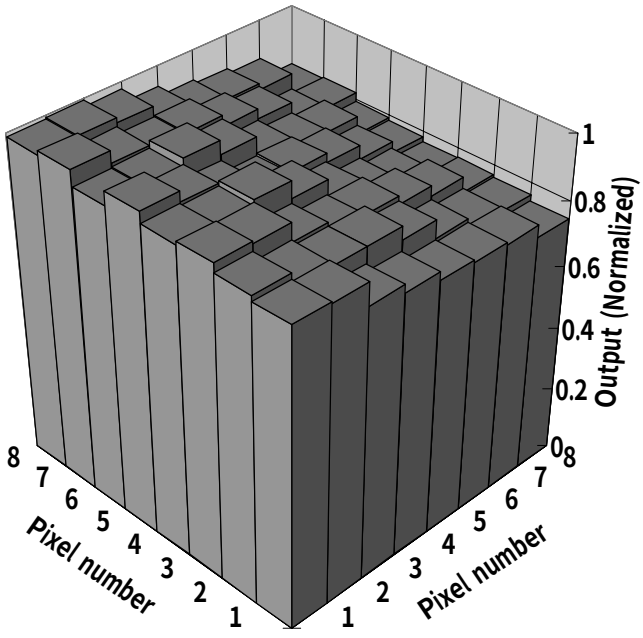

Fig. 6.24: Overall gains of pixels of the HPD-8×8 measured by scanning a light spot of 0.94mm on the center of each pixel.

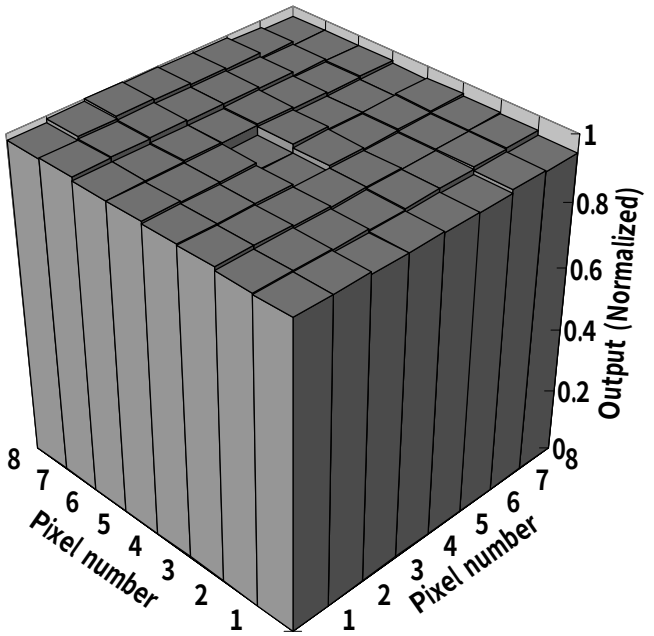

Fig. 6.25: Photocathode uniformity of the HPD-8×8 measured by scanning a light spot of 0.94mm on the center of each pixel.

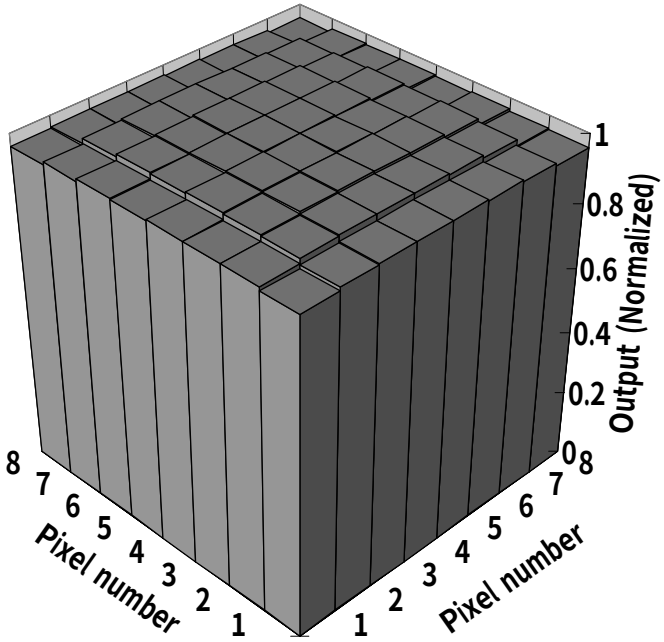

Fig. 6.26: Uniformity of the electron-bombarded gain derived from the measured responses.

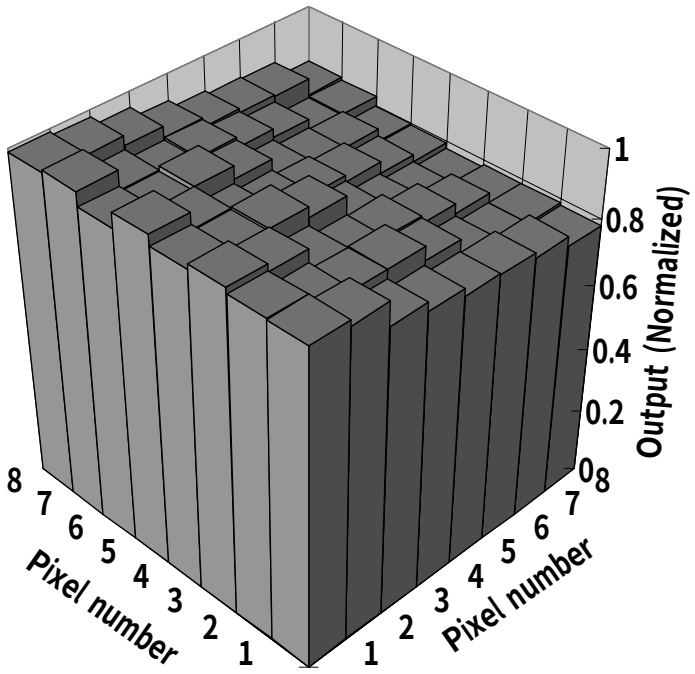

Fig. 6.27: Avalanche gain of pixels derived from the measured responses.

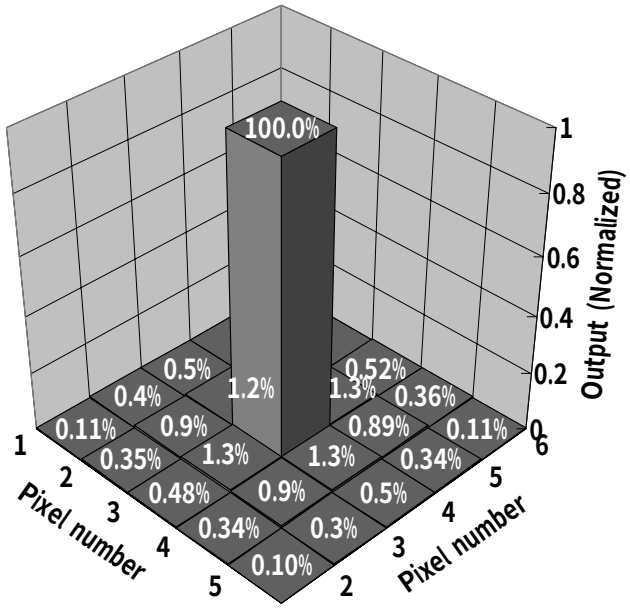

Fig. 6.28: Cross talk observed for a light spot of 0.94 mm at the center of the pixels.

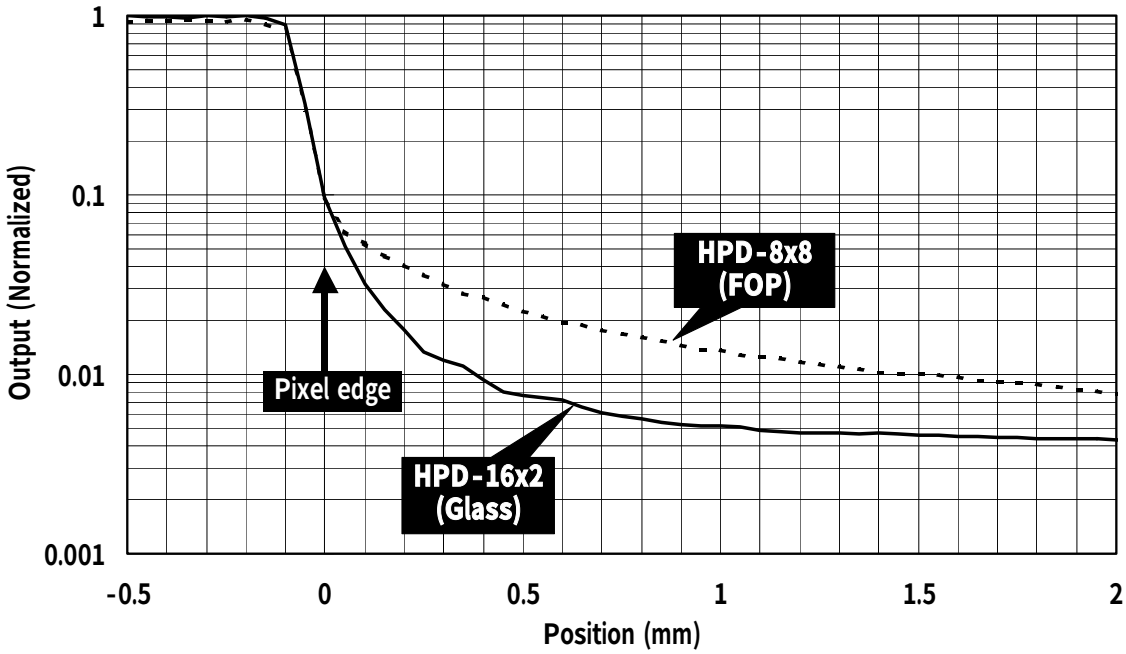

Fig. 6.29: Output signal by a light spot of 30 μm scanned over the pixel edge. It can be clearly seen that the FOP window gives a larger cross talk.

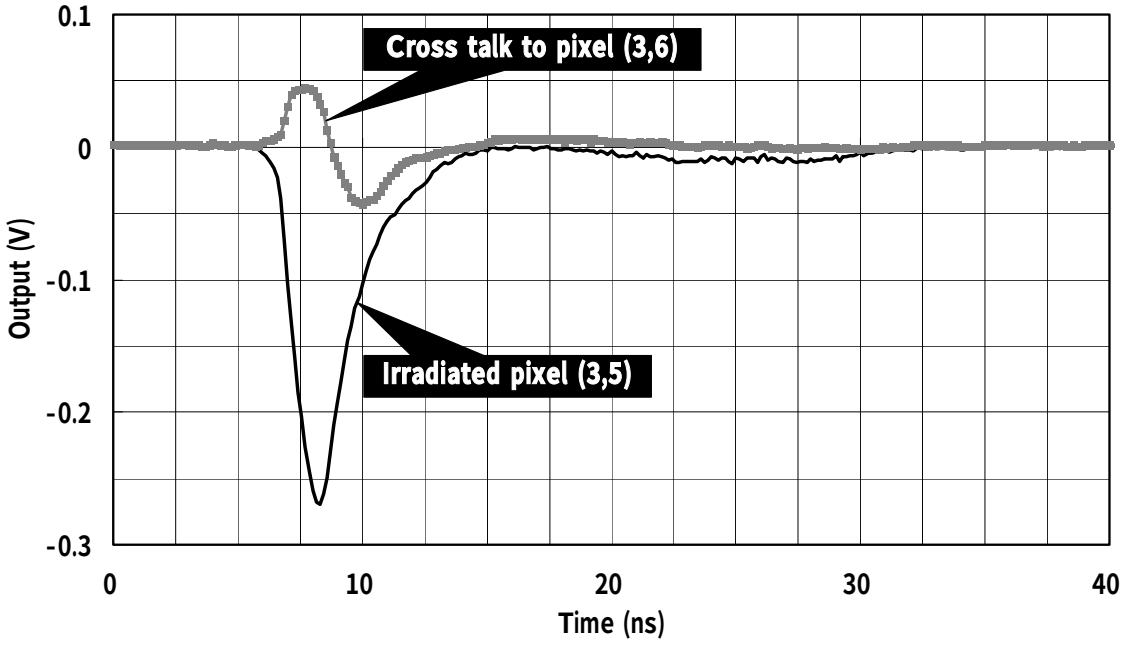

Fig. 6.30: Output signal observed in the irradiated pixel (3,5) and the next one (3,6) for pulsed light.

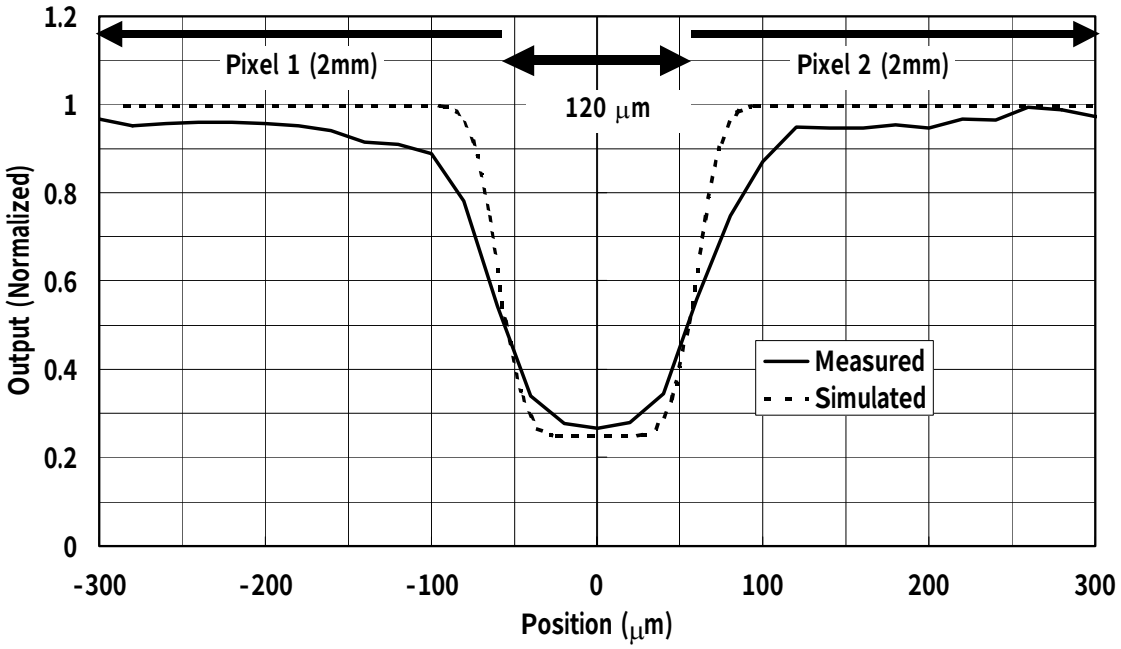

Fig. 6.31: Response at the boundary of the pixels measured by scanning a light spot of 30 μm. The simulated result assuming a step like low-gain zone of 0.12 mm wide and 25% of the normal gain is also shown.

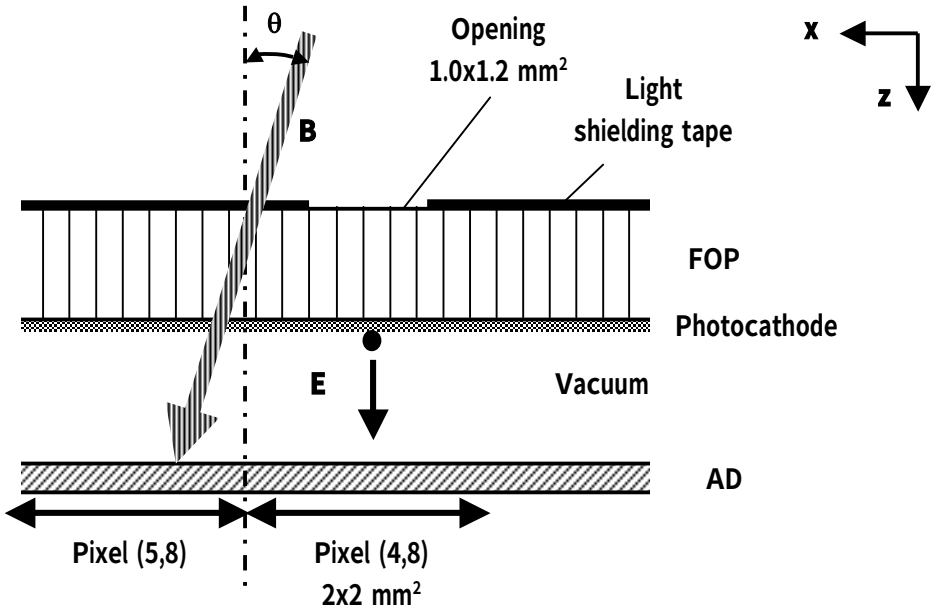

Fig. 6.32: Schematic illustration of a test in a magnetic field.
The coordinates as well as the angle (θ) of the magnetic field to the electric field are also given.

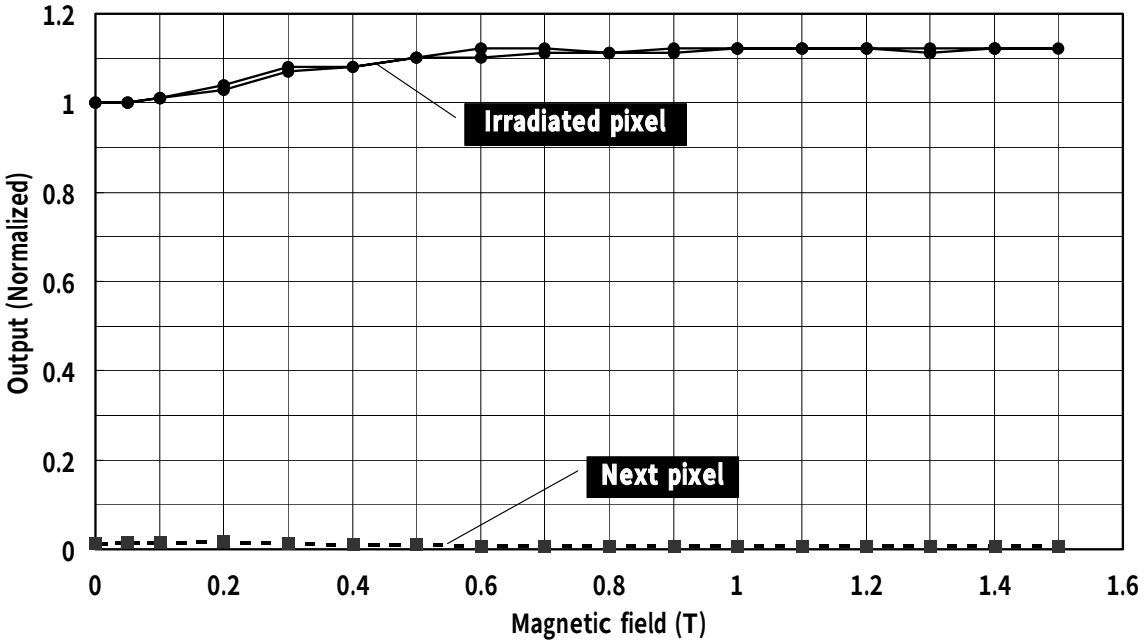

Fig. 6.33: Output current in two consecutive pixels as a function of the strength of the magnetic field parallel to the tube axis.

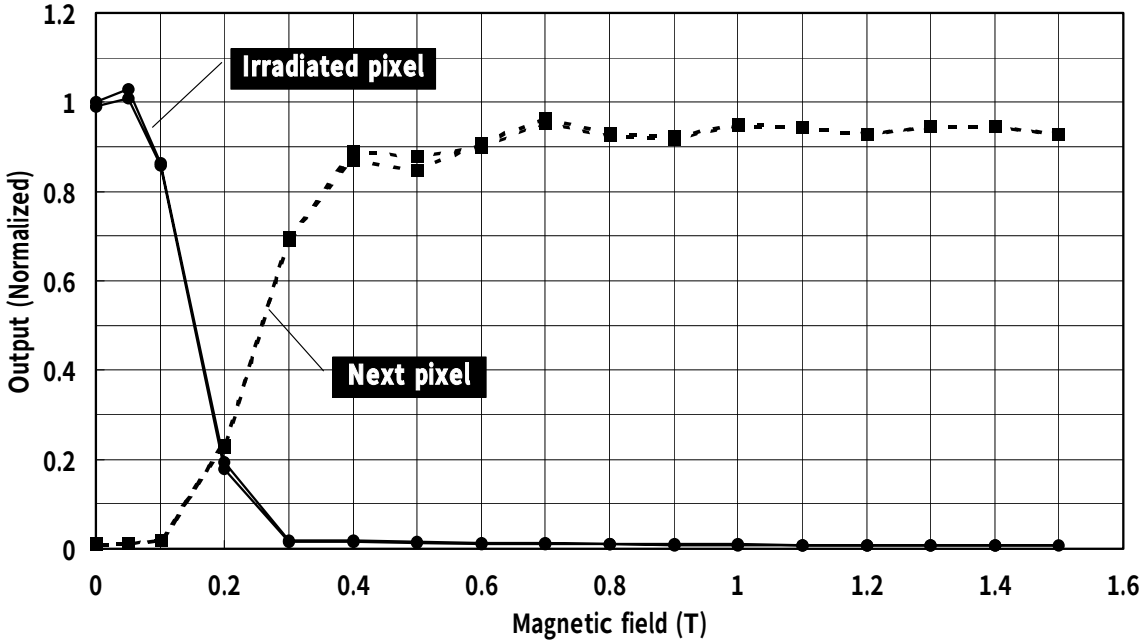

Fig. 6.34: Output current in two consecutive pixels as a function of the strength of the magnetic field applied at 30 degrees to the tube axis.

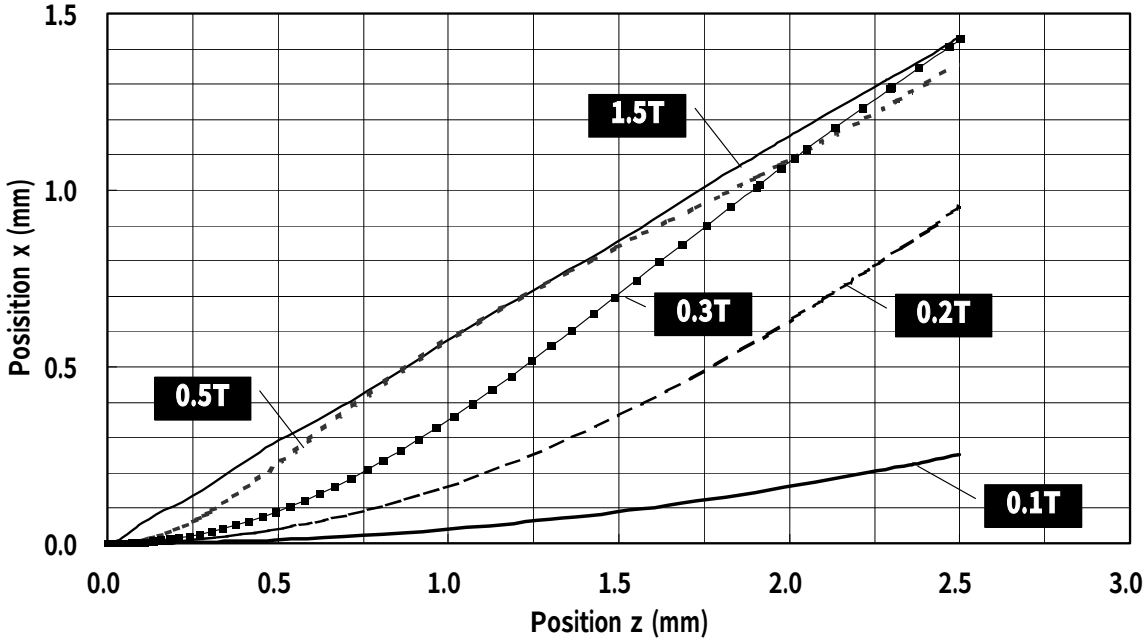

Fig. 6.35: Calculated electron trajectory in a magnetic field at 30 degrees to the tube axsis.

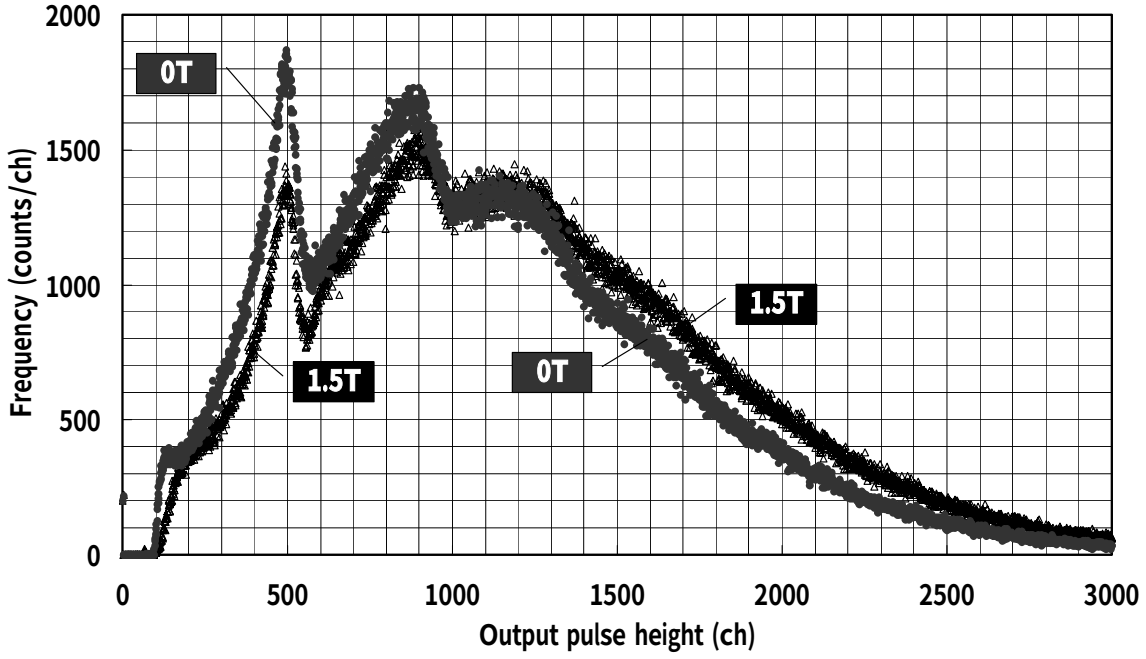

Fig. 6.36: Pulse-height spectra for a few photons with and without a magnetic field parallel to the tube axis.

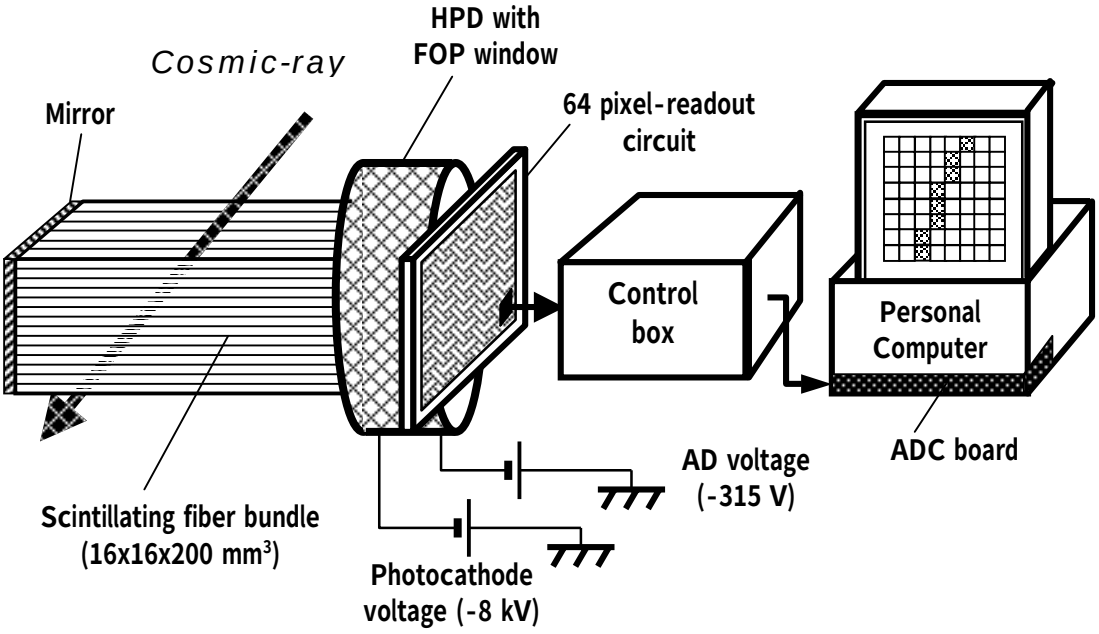

Fig. 6.37: Setup for a test with a scintillating fiber to observe cosmic-ray tracks.

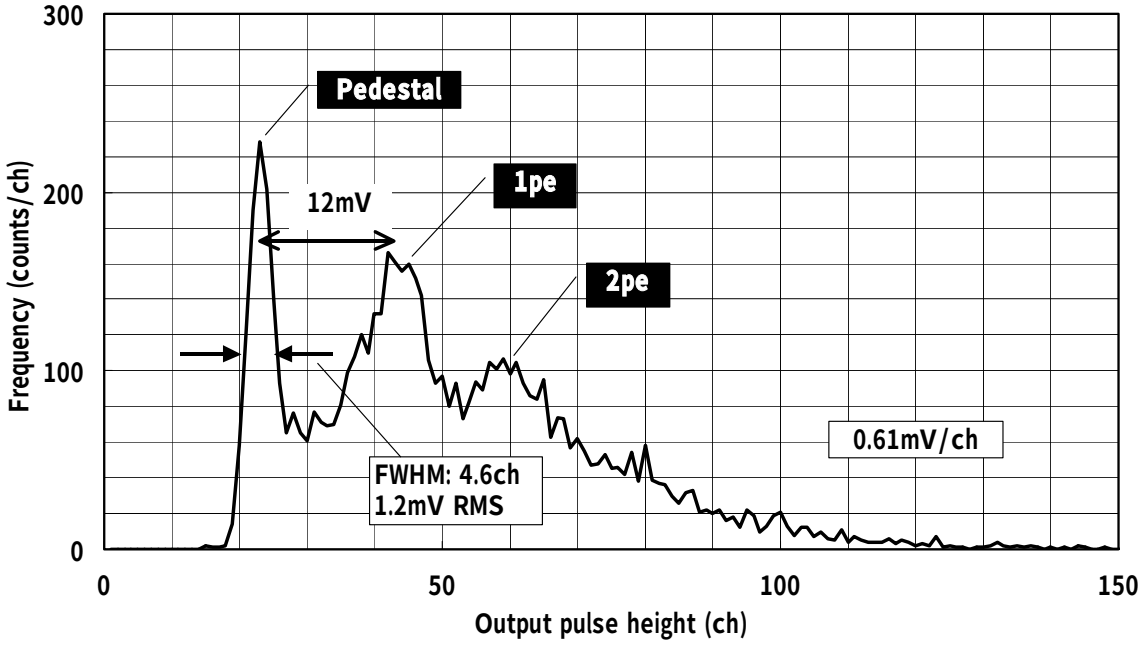

Fig. 6.38: Pulse-height spectrum measured by a 64 pixel-readout circuit.

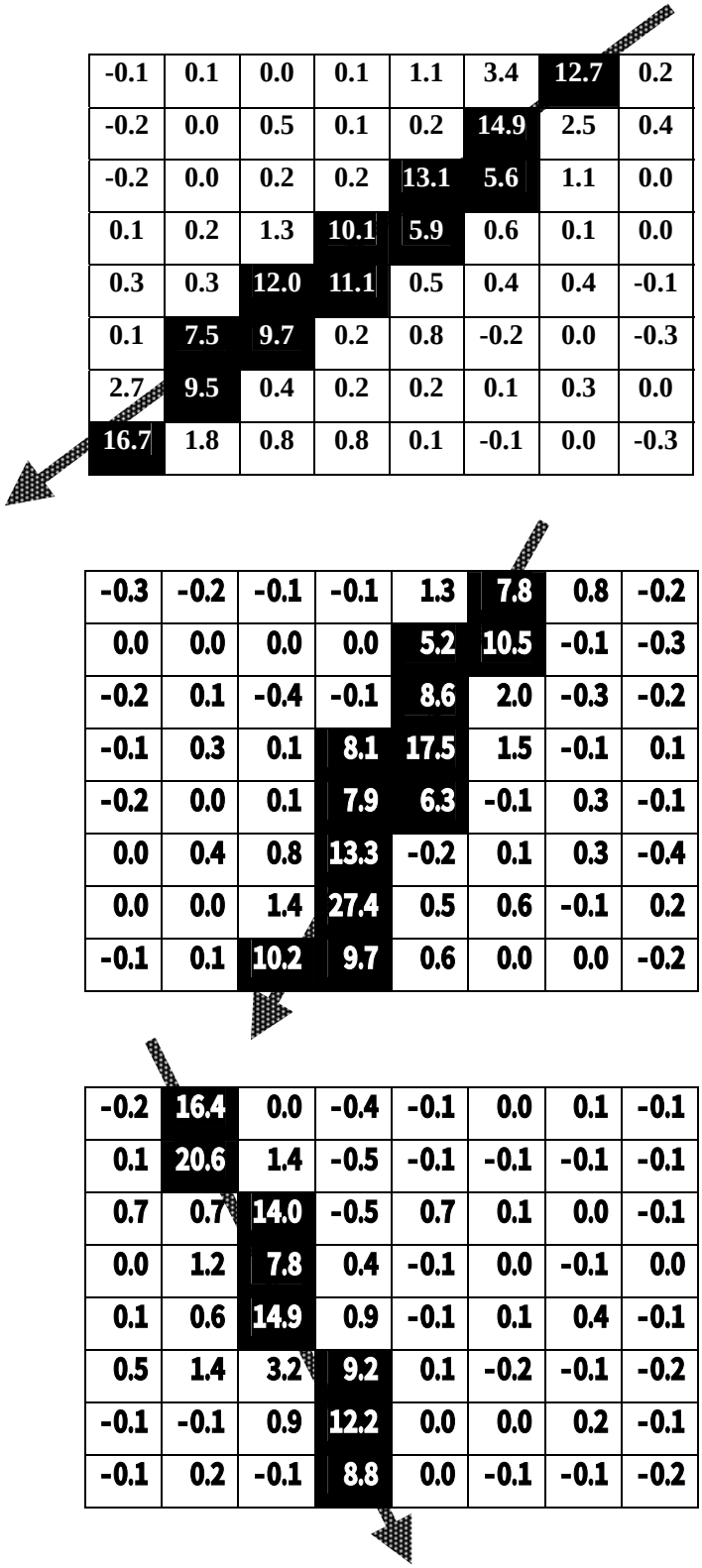

-0.1	0.1	0.0	0.1	1.1	3.4	12.7	0.2
-0.2	0.0	0.5	0.1	0.2	14.9	2.5	0.4
-0.2	0.0	0.2	0.2	13.1	5.6	1.1	0.0
0.1	0.2	1.3	10.1	5.9	0.6	0.1	0.0
0.3	0.3	12.0	11.1	0.5	0.4	0.4	-0.1
0.1	7.5	9.7	0.2	0.8	-0.2	0.0	-0.3
2.7	9.5	0.4	0.2	0.2	0.1	0.3	0.0
16.7	1.8	0.8	0.8	0.1	-0.1	0.0	-0.3

-0.3	-0.2	-0.1	-0.1	1.3	7.8	0.8	-0.2
0.0	0.0	0.0	0.0	5.2	10.5	-0.1	-0.3
-0.2	0.1	-0.4	-0.1	8.6	2.0	-0.3	-0.2
-0.1	0.3	0.1	8.1	17.5	1.5	-0.1	0.1
-0.2	0.0	0.1	7.9	6.3	-0.1	0.3	-0.1
0.0	0.4	0.8	13.3	-0.2	0.1	0.3	-0.4
0.0	0.0	1.4	27.4	0.5	0.6	-0.1	0.2
-0.1	0.1	10.2	9.7	0.6	0.0	0.0	-0.2

-0.2	16.4	0.0	-0.4	-0.1	0.0	0.1	-0.1
0.1	20.6	1.4	-0.5	-0.1	-0.1	-0.1	-0.1
0.7	0.7	14.0	-0.5	0.7	0.1	0.0	-0.1
0.0	1.2	7.8	0.4	-0.1	0.0	-0.1	0.0
0.1	0.6	14.9	0.9	-0.1	0.1	0.4	-0.1
0.5	1.4	3.2	9.2	0.1	-0.2	-0.1	-0.2
-0.1	-0.1	0.9	12.2	0.0	0.0	0.2	-0.1
-0.1	0.2	-0.1	8.8	0.0	-0.1	-0.1	-0.2

Fig. 6.39: Tracks of a cosmic-ray muon observed by an HPD, where the number of photoelectrons detected in each pixel is given in each column. Pixels with more than 5 photoelectrons are hatched, clearly displaying the passage of cosmic-ray muons.

Chapter 7

Conclusion and future prospects

7.1 Summary

Since no multi-pixel avalanche diode has been available for electron multiplication, the new structure of an avalanche diode (AD) with back illumination was developed for a hybrid photo-detector (HPD). Several test samples were fabricated to extract the design parameters for the most suitable structure. Based on these results, an AD having 64 pixels (8×8 array) of 2×2 mm^2 each was designed for an HPD. In fabricating the HPD, flip-chip bonding was successfully used to assemble the AD to a stem having a multi-layer ceramic structure to make electrical connection between the AD located on the vacuum side and the output pins on the atmospheric side. Thus, a prototype HPD with a multi-pixel AD was successfully developed.

The performance of a prototype HPD was evaluated. The results are summarized in Table 7.1. The electron-bombarded gain was 1190 with a photocathode voltage of -8 kV, and the avalanche gain was 48 with an AD voltage of 354 V. Thus, the total gain was 5.7×10^4. With this gain, a timing resolution of 89 ps was achieved for single photons. Such a high gain and precise timing resolution were accomplished for the first time in a HPD using an appropriately designed AD. The non-uniformity of the pixel-to-pixel sensitivity was as small as 7.9%, which is much better than that of multi-anode PMTs. In addition, the new HPD can be used in high magnetic fields of at least up to 1.5 T.

Finally, a long-term stability was tested. No degradation of the sensitivity was observed for a total output charge of 0.43 C/pixel, and the AD leakage current was not increased at all. This integrated charge during the test period corresponds to 29,000 hours of operation at an event rate of 100 kHz with an incident light level of 10 photoelectrons/pixel/event. This long-term stability of the new HPD is also due to the newly developed AD, particularly its backside illumination. All of these results are satisfactory, and this HPD is ready for use in particle physics experiments.

Parameter	Description	unit	Condition
Total Gain	5.7×10^4		Photocathode voltage: -8 kV AD voltage: 354 V
Rise time	1.1	ns	Photocathode voltage: -8 kV AD voltage: 302 V
Decay time	1.7	ns	
Timing resolution	89	ps	Single photon
Pixel uniformity	7.9	%	Gain: 6.1×10^4
Gap of low gain zone between pixels	0.12	mm	Gain: 4.0×10^4
Number of discriminated photoelectrons	5		From pulse-height spectrum
Immunity for magnetic field	up to 1.5	T	Parallel to tube axis

Table 7.1: Performance of the developed HPD.

7.2 Performance to be improved

Although the performance of the developed HPD is satisfactory, some aspects can be improved further, as follows.

7.2.1 Photocathode sensitivity

In this study, a practical multi-alkali photocathode was selected for the prototype HPD. Recently, highly sensitive photocathodes based on single-crystal semiconductors are available, and have been used in image intensifiers [1]. Since the structure and manufacturing process of the HPD is similar to that of image intensifiers, a photocathode, such as the GaAsP type, is easily applicable to HPDs. According to reference [2], the quantum efficiency (QE) of a GaAsP photocathode is 50% in the visible light region. Therefore, this photocathode is suitable for scintillating fiber readout.

7.2.2 Electron-bombarded gain and energy resolution

Appendix 1 shows that the thickness of the surface dead layer of an AD affects the electron-bombarded gain (m_{EB}); a thinner surface dead layer provides a higher gain. Also, the energy resolution is improved by having a thinner dead layer. In order to make a thin dead layer, one should have a thin p+ layer, thus a shallow p+/p junction. For a shallow junction, the delta-doped technology [3] could be used. In this case, a highly doped (4×10^{20} /cm^3) thin layer (2.5 nm) is grown on Si by a molecular-beam epitaxy. According to the result shown in reference [3], an m_{EB} of 2000 is expected at a photocathode voltage of -8 kV, while it was approximately 1200 in

this study.

Another method to increase the gain and the energy resolution is simply to increase the photocathode voltage, as suggested in Appendix 1. In this study, the maximum voltage between the photocathode and the AD was 9 kV. A higher voltage was not tried in order to avoid fatal damage of the HPD and the readout circuit due to a voltage breakdown. As far as we are aware, the sustainable voltage of the proximity focused structure is less than 10 kV for stable operation. Much more effort is still necessary to improve the sustainable voltage of an HPD.

7.2.3 Cross talk for pulsed light

Capacitive coupling between pixels apparently causes cross talk for pulsed light. A large part of the capacitive coupling is attributed to an electrical path of 10 mm to 20 mm between the AD and the output pins. This can be shortened by removing the connecting board. Then, the AD is directly bonded to the stem using a flip-chip bonding method. In this case, the thermal expansion coefficient of the stem should be close to that of Si to avoid mechanical stress on the AD during the baking process. With this structure, the time response can be improved as well, because the stray capacitance on the connecting board is eliminated.

7.3 Useful extensions of the technology

7.3.1 Number of pixels

In this study, the number of pixels of the HPD was 64 (8×8 pixels) with a pixel size of 2×2 mm^2. Apparently, the technology for a multi-pixel AD used in electron multiplication can be applied to various geometries by simply changing the design. Assuming the same total area of 16×16 mm^2, a pixel arrangement with 32×32 pixels (totally 1024 pixels) of 0.5×0.5 mm^2 each is available. The limitation is a low gain zone of approximately 0.1 mm between the pixels. When the number of pixels is large, care should be taken concerning the number of output pins. More than one hundred output pins are not easily housed on a stem. In this case, a readout chip should be incorporated in the vacuum. Then, output pins just to drive the chip are necessary, and the output signal from each pixel is read out sequentially.

7.3.2 Enlargement of an effective area

A drastic enlargement of the effective area can be achieved by using a different type of

electron-focusing system, an electrostatically focused lens. In this case, electrons from a large-area photocathode are demagnified and focused onto the AD by an electron lens. The applicable demagnification factor is 5 to 10, which is determined by the design of the electron optics. If a demagnification factor of 5 is assumed, the overall effective area is 80×80 mm^2 and the pixel size is 2.5×2.5 mm^2 on the photocathode, assuming an AD of 32×32 pixels with a pixel size of 0.5×0.5 mm^2. With this size, the benefits as an HPD, such as high gain, high speed, high-energy resolution and small dead area between pixels, can be maintained. In addition, the cost per pixel is low with this structure. This type of HPD is useful for scintillating fiber readout and ring-imaging Cherenkov counters (RICH). It should be noted that the feature of demagnification by an electron lens is an efficiency of 100%. In the case of an optical method, such as a lens or a tapered fiber-optic plate (tapered FOP), the light power on the focal plane is the inverse square of the demagnification factor, or less.

7.4 Conclusion

In spite of many attractive features, an HPD with a multi-pixel AD has so far not been available. This fact motivated this study, and such an HPD equipped with a specially designed AD for electron multiplication has been developed. Evaluated from various viewpoints, the overall performance of the HPD has been shown to be quite satisfactory. The developed HPD, a new multi-pixel photon sensor with single-photon sensitivity, can be used in real experiments, and will contribute to the progress of particle physics.

[REFERENCES]

[1] Catalogue of Hamamatsu Photonics K.K., Electron Tube Center, “Image Intensifiers”, December 2000

[2] M. Muramatsu and M. Suyama, “Special CCD image sensors (in Japanese)”, O plus E Vol.23, No.4, pp.455-461, 2001

[3] S. Nikzad et al., "Direct detection and imaging of low energy electrons with delta-doped charge-coupled devices", Applied Physics Letters, Vol.73, No.23, pp.3417-3419, 1998

Acknowledgement

I wish to thank Prof. Junji Haba for supervising me and giving me a lot of advice on this research to develop a multi-pixel photon sensor with single-photon sensitivity. His useful advices from the conceptual design to the evaluation method of the prototype sensor were essential to the successful completion of this work. I would like to express my special gratitude to Prof. Seigi Iwata and Prof. Fumihiko Takasaki for providing me with this wonderful opportunity to study this thesis in the Graduate University for Advanced Study and for their encouragement. I would like to thank Prof. Yoshikazu Yamada and Dr. Toru Tsuboyama for checking and brushing up this thesis to clearly describe the study. I wish to thank Prof. Francesc Salvat of Universitat de Barcelona for instructing me in the simulation code PENELOPE, and useful discussion about the result with it.

I would like to express my thanks to Messrs. Junichi Takeuchi and Toshikazu Hakamata of the electron tube center (ETC) of Hamamatsu Photonics K. K. (HPK) and Dr. Koichiro Oba for giving me the chance to carry out this study in the university. Special thanks are due to Messrs. Koei Yamamoto, Yoshitaka Ishikawa and Masaharu Muramatsu of the solid state division of HPK for technical discussions about avalanche diodes. Without the discussions with them, a high performance multi-pixel avalanche diode for electron multiplication would have never been realized. I would like to thank Messrs. Tetsuya Morita, Shinichi Muramatsu, Itaru Mizuno, Masuo Ito, Masao Kinoshita and Katsuyuki Kinoshita of ETC of HPK for their support to develop a sensor. I greatly appreciate kindly cooperation of Messrs. Akihiro Kageyama and Keisuke Inoue for assembling the avalanche diode, and Messrs. Yoshihiko Kawai and Atsuhito Fukasawa for discussions about the evaluation. I would like to express my sincere gratitude to other colleagues of HPK and my family for their support.

Appendix 1

Simulation of the electron-bombarded gain

In order to quantitatively analyze the behavior of electrons in Si, the simulation code PENELOPE, developed by F. Salvat et al. [1], was found to be useful. PENELOPE is a Monte-Carlo simulation code for electrons and photons to go through materials while taking care of interactions, such as elastic scattering, inelastic collisions and bremsstrahlung. With this code, the energy-deposition process of primary electrons as well as secondary electrons were calculated until the electron kinetic energy decreased to 100 eV. Electrons with less than 100 eV hardly move, and deposit the reminder of their energy nearby. All interactions were considered by setting the cutoff energy to be 0 eV. At an electron energy of 8 keV, for example, it took 10 minutes to simulate a 3×10^4 electron sample by a personal computer.

A1.1 Depth-dose characteristic

The energy deposition of electrons per unit length in Si was calculated for various energies. The results are shown in Fig. A1.1. The distribution of the energy deposition depends on the energy of the incident electrons. In the case of an 8 keV electron, the maximum energy deposition occurs at a depth of 0.23 μm, and most of the energy is deposited within 1 μm.

A1.2 Energy loss by backscattering

There are two factors that cause a loss of energy. One is backscattering, and the other is energy loss in the surface dead layer. The former is described here, and the latter in the next section. The probability of backscattering and the average energy of backscattered electrons are shown in Fig. A1.2 as a function of the incident-electron energy. The probability is approximately 20%, and the average energy is approximately 65% of the incident energy. These results are almost flat over

electron energies from 2 keV to 12 keV. The product of these two gives the energy loss by backscattering, as shown in Fig. A1.3.

A1.3 Energy loss in the surface dead layer

The energy loss in the surface dead layer at the entrance of the AD was calculated for thicknesses of 50 nm, 100 nm and 300 nm. The calculated fractional energy loss is shown in Fig. A1.4. This shows that the energy loss in the dead layer increases with the thickness and decreases with the electron energy. At an electron energy of 8 keV, the normalized energy loss is 47% for a thickness of 300 nm, 13% for 100 nm, and 5% for 50 nm.

A1.4 Electron-bombarded gain

The electron-bombarded gain (m_{EB}) is determined by the energy deposited in the effective layer, which is the incident-electron energy minus the two energy losses discussed above. The gain (m_{EB}) can be derived from the deposited energy (E_{depo} [eV]) as follows:

$$m_{EB} = \frac{E_{depo}}{3.6}, \tag{A1.1}$$

where 3.6 [eV] is the electron-hole pair production energy in Si. The energy deposition in the effective layer was calculated for various thicknesses of the surface dead layer. The results are shown in Fig. A1.5 as a function of the incident-electron energy, where the deposited energy is converted to m_{EB}. The m_{EB} values for 8 keV electrons are 1840, 1680 and 910 for thicknesses of 50 nm, 100 nm and 300 nm, respectively. m_{EB} is higher for a thinner dead layer. It should be noted that even m_{EB} with no surface dead layer is smaller than the ideal gain, defined as $E_{in}/3.6$, where E_{in} is the incident electron energy. This is because E_{depo} is always smaller than E_{in} because of an energy loss due to backscattering.

A1.5 Pulse-height spectra

The energy loss due to the backscattering and that in the surface dead layer produces a fluctuation of m_{EB}, and determines the pulse-height resolution for single electrons. The fluctuations of the deposited energy were simulated for various thicknesses of the surface dead layer with 8 keV electrons. The results shown in Fig. A1.6 exhibit pulse-height spectra for the input of single electrons. The horizontal axis is the number of secondary electrons, and is identical to m_{EB}. It is clearly shown that the pulse-height resolution is improved by thinning the surface dead layer. The resolution, which is defined by the ratio of the standard deviation and the peak position, is listed in

Table A1.1. In the same way, fluctuations of the deposited energy were calculated at various incident-electron energies with a dead layer fixed to 235 nm, which comes from section 6.1. The simulated result is shown in Fig. A1.7. The pulse-height resolution clearly improves with the electron energy. The resolution is summarized in Table A1.2. From these results, it is concluded that the pulse-height resolution is improved by thinning the surface dead layer and/or increasing the incident-electron energy.

Dead	50 nm	100 nm	300 nm
Resolution (%)	0.9	2.5	10.2

Table A1.1: Simulated resolution for the single-electron input with various thicknesses of surface dead layer at an electron energy of 8 keV.

Energy	8 keV	10 keV	12 keV
Resolution (%)	7.2	4.6	3.3

Table A1.2: Simulated resolution for the single-electron input with various energies of electrons at a thickness of 235 nm.

[REFERENCES]

[1] F. Salvat et al., "PENELOPE – A Code System for Monte Carlo Simulation of Electron and Photon Transport", NEA/NSC/DOC Vol. 19, 2001

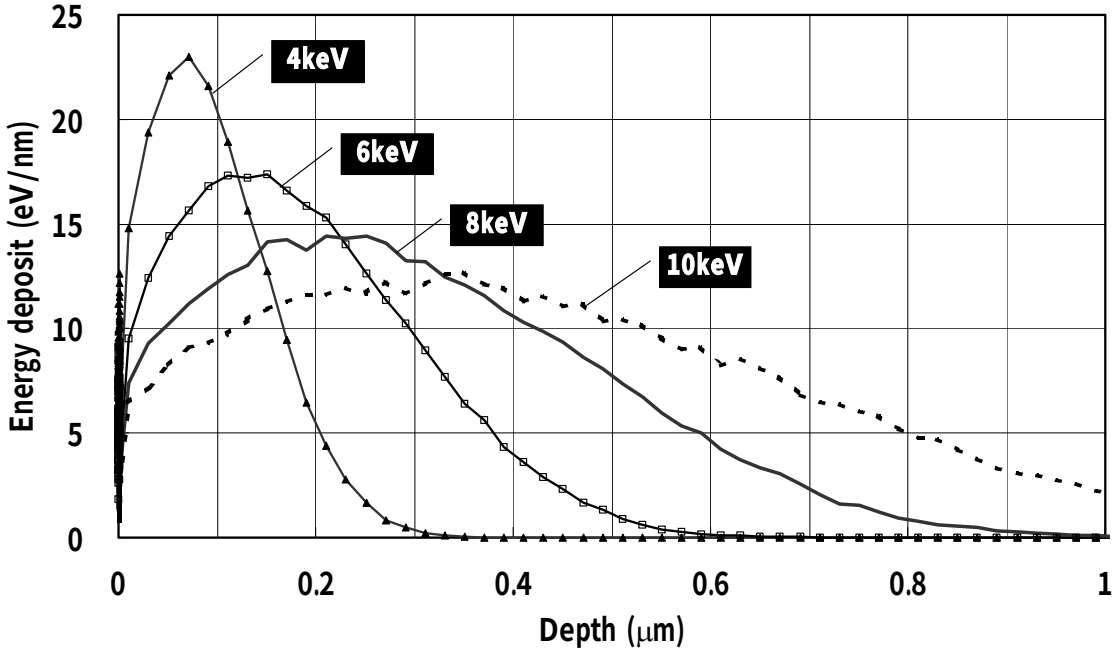

Fig. A1.1: Electron energy deposit in Si as a function of the depth.

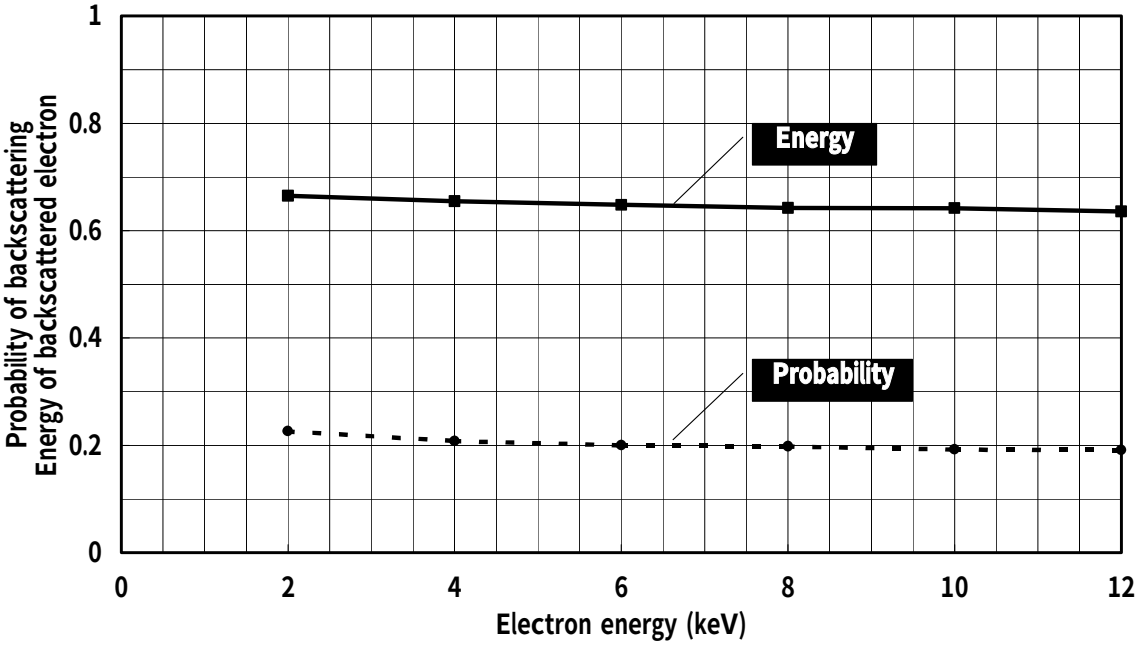

Fig. A1.2: Probability of backscattering and the average energy of backscattered electrons normalized to the energy of incident electrons, as a function of the electron energy.

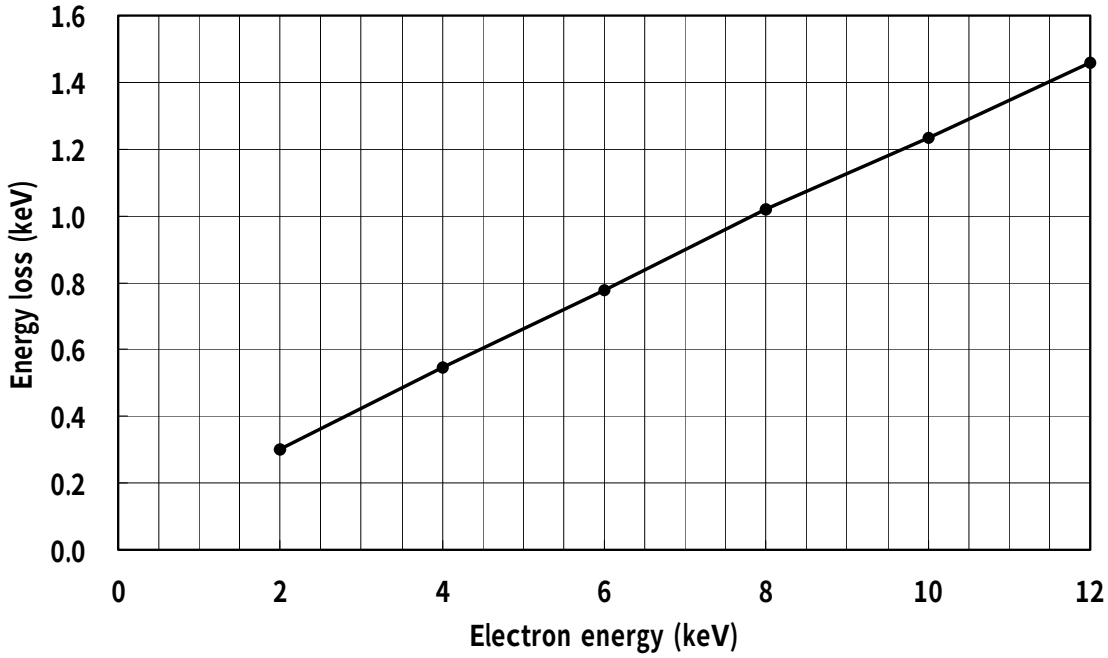

Fig. A1.3: Energy loss by backscattering given as a product of the probability and the average energy of a backscattered electron.

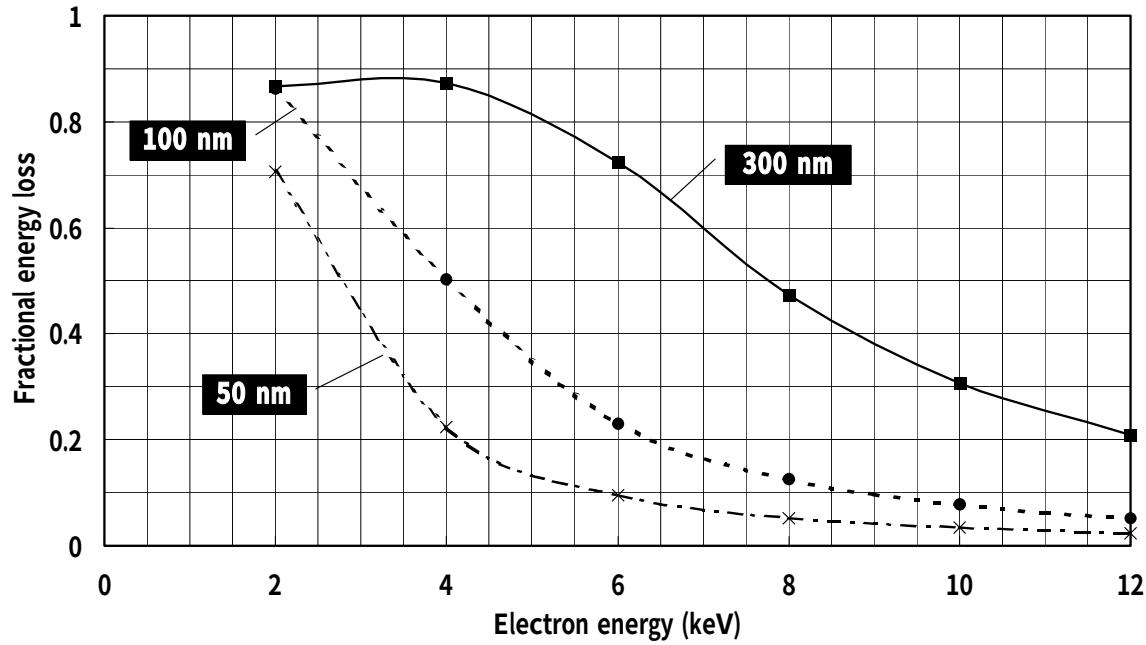

Fig. A1.4: Fractional energy loss in the surface dead layer for various thicknesses as a function of the electron energy.

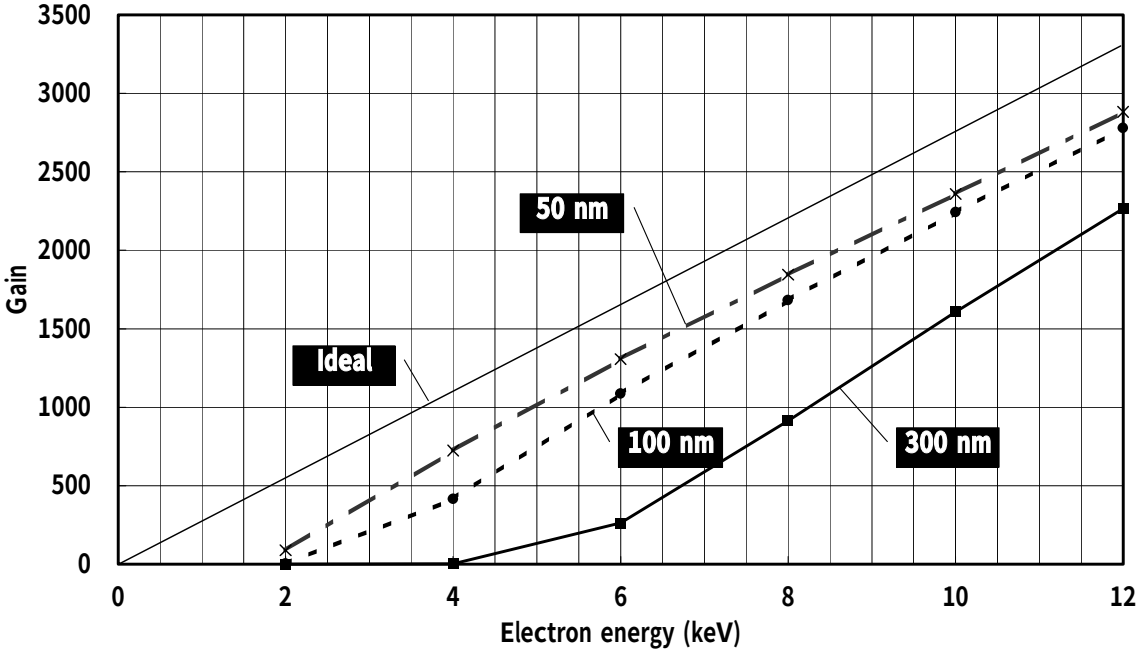

Fig. A1.5: Electron-bombarded gain for various thicknesses of the surface dead layer as a function of the electron energy. "Ideal" is given by equation A1.1 in the text.

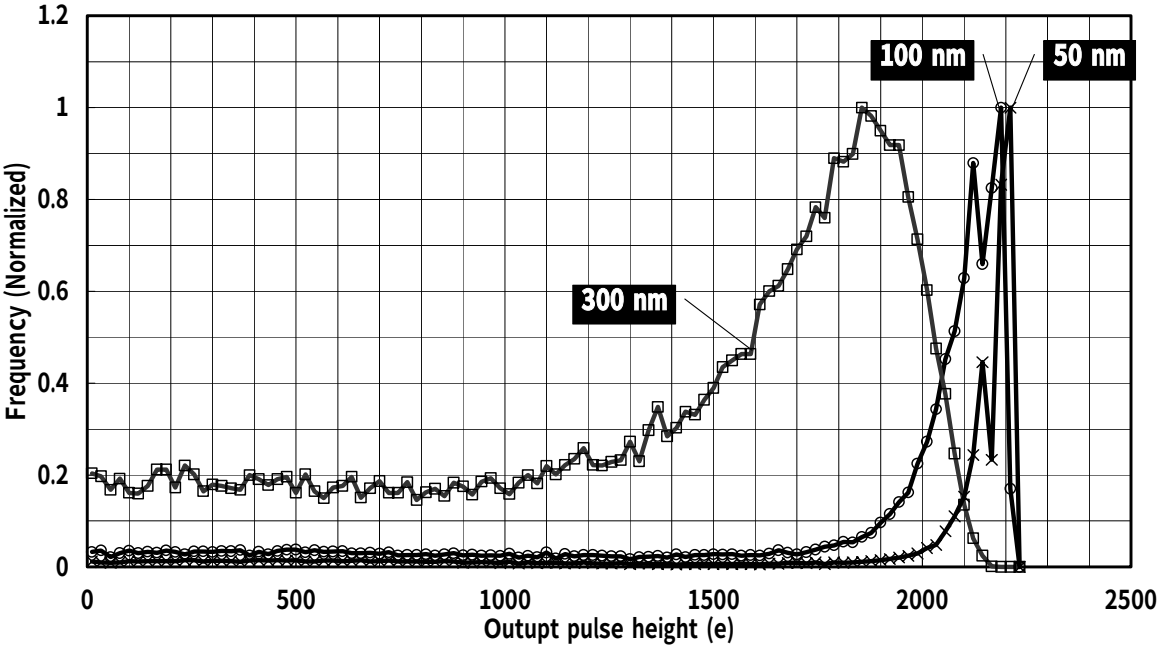

Fig. A1.6: Calculated pulse-height spectra for various thicknesses of the surface dead layer, with an electron energy of 8 keV.

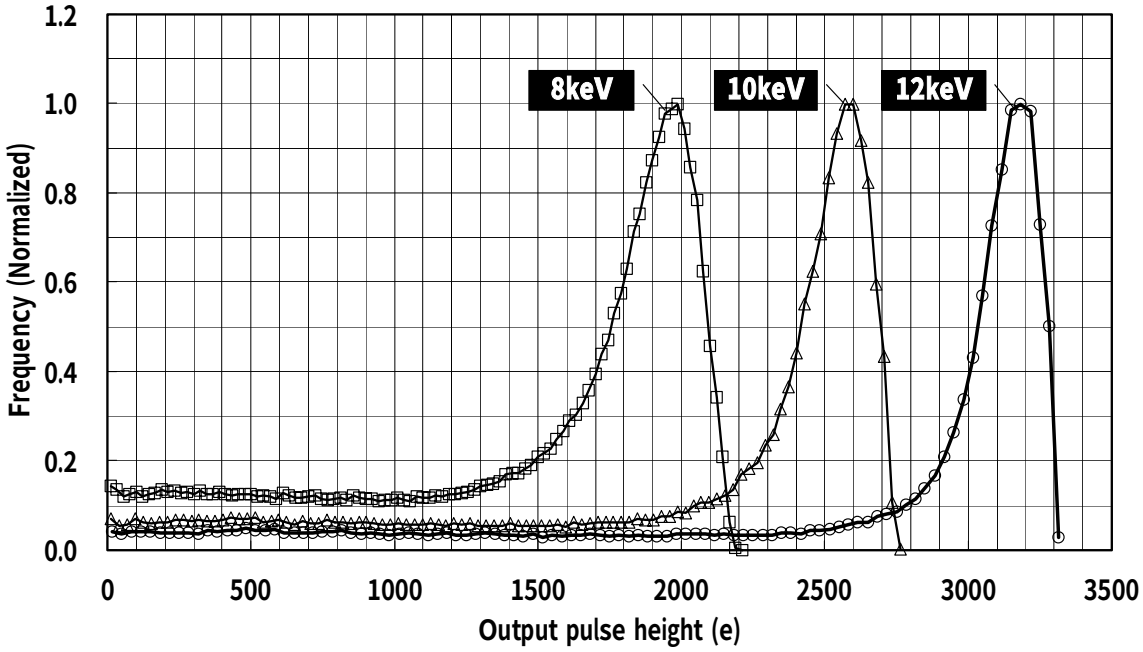

Fig. A1.7: Calculated pulse-height spectra for various energies of electrons, with a surface dead layer of 235 nm.

Appendix 2

Calculation of the full depletion voltage for an avalanche diode

The full depletion voltage (V_T) of APD-3 (reverse reach-through type), shown in Fig. 4.2 (c), is roughly estimated with various thicknesses of the substrate. With the structure of APD-3, V_T is derived as the sum of the depletion voltage of the avalanche region (V_1) and that of the substrate (V_2). Then, V_1 is given as

$$V_1 = \frac{E_{\max} \times W_1}{2}, \qquad \text{(A2.1)}$$

where E_{max} is the maximum electric field at the pn junction, and W_1 is the thickness of the avalanche region. If W_1=25 μm and E_{max} =3×10^5 V/cm [6] are assumed, V_1 is 375 V. On the other hand, the depletion voltage of substrate V_2 is given by

$$V_2 = \frac{{W_2}^2}{2 \times \varepsilon \times \mu \times R_s}, \qquad \text{(A2.2)}$$

where W_2 is the thickness of the substrate (p- layer), ε the dielectric constant of Si, μ the carrier mobility and R_s the resistivity of the p- layer. Apparently, V_2 is proportional to the square of the substrate thickness and inversely proportional to the substrate resistivity.

Assuming an R_s of 4 kΩcm as being the maximum attainable resistivity of a wafer and a μ of 480 cm^2/Vs, the depletion voltage for the substrate (V_1) and the full depletion voltage ($V_T = V_1 + V_2$) were calculated. The results are plotted in Fig. A2.1 as a function of the thickness of the substrate. The total voltages for full depletion turn out to be 400 V, 476 V and 603 V for thicknesses of 100 μm, 200 μm and 300 μm, respectively.

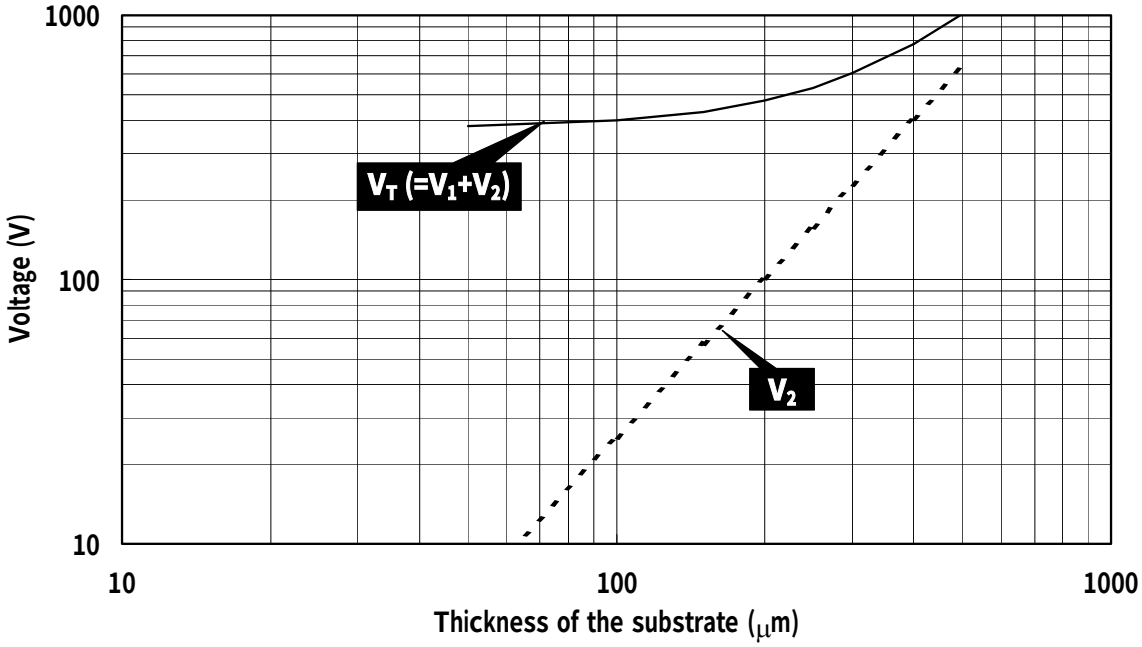

Fig. A2.1: Calculated full depleiton voltage (V_T =V_1+V_2) and the depletion voltage of the substrate (V_2) as a function of the thickness of the substrate, assuming a substrate resistivity of 4 kΩcm and a maximum electric field of 3×10^5 V/cm at the pn junction.

Appendix 3

Noise factor of a hybrid photo-detector

A theoretical treatment of the noise factor is discussed for an HPD having two-stage cascade multiplication, as shown in Fig. A3.1. It is assumed that the input signal has an amplitude of A_1 and a fluctuation of σ_1. This is amplified by the first stage, electron-bombarded multiplication, where the gain is m_{EB} and the fluctuation of the amplification is σ_{EB}. The signal is further multiplied by the second stage, avalanche multiplication, where the gain is m_{AD} and the fluctuation of the amplification is σ_{AD}. The amplitude and the fluctuation of the output signal are A_3 and σ_3, respectively.

First, the contribution of the additional noise in the first stage is considered. Denoting the amplitude and the fluctuation of the first stage output as A_2 and σ_2, the noise factor of the first stage (F_{EB}) is defined as

$$F_{EB} = \left(\frac{A_1/\sigma_1}{A_2/\sigma_2}\right)^2 = \frac{\sigma_2^2}{\sigma_1^2 \times m_{EB}^2}. \quad \text{(A3.1)}$$

Then, σ_2 is determined by the amplitude (A_1), fluctuation (σ_1), and the fluctuation of amplification (σ_{EB}) as follows:

$$\sigma_2^2 = (\sigma_1 \times m_{EB})^2 + A_1 \times \sigma_{EB}^2. \quad \text{(A3.2)}$$

Here, the noise of each multiplication is assumed to be incoherent. Using this equation, equation A3.1 can be rewritten as

$$F_{EB} = 1 + \left(\frac{\sigma_{EB}}{m_{EB}}\right)^2, \quad \text{(A3.3)}$$

where a Poisson distribution of the input signal ($\sigma_1^2 = A_1$) is assumed. In the same way, the noise factor of the second stage (F_{AD}) can be shown to be

$$F_{AD} = 1 + (\frac{\sigma_{AD}}{m_{AD}})^2 . \quad \text{(A3.4)}$$

Secondly, the noise factor of the two-stage cascade multiplication (F_{HPD}) is considered. According to the definition, F_{HPD} can be expressed as

$$F_{HPD} = (\frac{A_1 / \sigma_1}{A_3 / \sigma_3})^2 = \frac{\sigma_3^2}{\sigma_1^2 \times m_{EB}^2 \times m_{AD}^2} . \quad \text{(A3.5)}$$

In the same way as shown in equation A3.2, σ_3 can be expressed as

$$\sigma_3^2 = \sigma_2^2 \times m_{AD}^2 + A_2 \times \sigma_{AD}^2$$

$$= \sigma_2^2 \times m_{AD}^2 + A_1 \times m_{EB} \times \sigma_{AD}^2 . \quad \text{(A3.6)}$$

Using equations A3.2 and A3.6, equation A3.5 can be rewritten as

$$F_{HPD} = 1 + \frac{\sigma_{EB}^2}{m_{EB}^2} + \frac{\sigma_{AD}^2}{m_{AD}^2} \times \frac{1}{m_{EB}}$$

$$= F_{EB} + \frac{F_{AD} - 1}{m_{EB}} . \quad \text{(A3.7)}$$

This equation clearly shows that the effect of the second stage, i.e. the additional noise of the avalanche multiplication, is reduced by the gain of the first stage (m_{EB}).

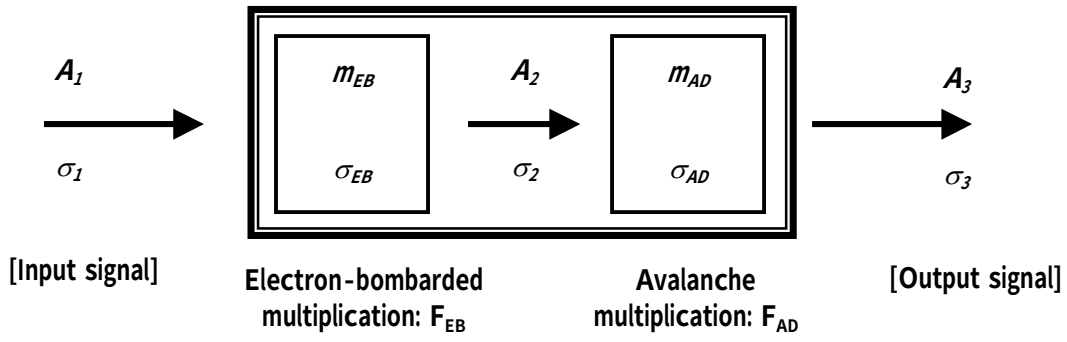

Fig. A3.1: Schematic drawing of the cascade multiplication process in an HPD.

Appendix 4

Estimation of the transit time between a photocathode and an avalanche diode

The transit time of electrons between the photocathode and the avalanche diode (AD) is calculated to check the validity of the result given in section 6.3.2. The transit time (Tt [s]) of an electron emitted perpendicular to the photocathode at an initial velocity (v_0 [m/s]) can be calculated by the following equation:

$$Tt = \frac{-v_0 + \sqrt{{v_0}^2 + 2 \times a \times W}}{a}, \qquad \text{(A4.1)}$$

where a [m/s^2] is the acceleration determined by the gap (W [m]) and the potential difference (V [V]) between the photocathode and the AD. The initial velocity (v_0) can be expressed in terms of the initial energy (V_0 [eV]) as

$$v_0 = \sqrt{\frac{2 \times e \times V_0}{m}}, \qquad \text{(A4.2)}$$

where e is the charge and m is the mass of the electron. If the voltage between the photocathode and the AD is 8 kV with a distance of 2.5 mm, the transit time is calculated to be 94 ps for electrons with an initial velocity of 0. The transit-time difference between the initial energies of 0 and 1.2 eV is 1.2 ps, and is negligibly small. Since the initial energy of 1.2 eV represents the highest part of the energy distribution for multi-alkali photocathode, as shown in Fig. 5.2, the timing resolution shown in Fig. 6.23 is not dominated by the spread of the transit time between the photocathode and the AD.

Appendix 5

Electron trajectory in a magnetic field

The electron trajectory in a magnetic field is derived to check the experimental result given in section 6.5.1. The equation of electron motion in an electric field (***E*** *(E_x, E_y, E_z)*) and a magnetic field (***B*** *(B_x, B_y, B_z)*) can be written as

$$\vec{a} = \frac{e \times (\vec{E} + \vec{v} \times \vec{B})}{m}, \tag{A5.1}$$

where ***a*** is the acceleration and ***v*** is the velocity of an electron; *e* and *m* are the charge and mass of an electron. With the proximity focused structure, it is assumed that the electric field is parallel to the *z* direction and the magnetic field is in the *x*-*z* plane, as shown in Fig. A5.1. Then, equation A5.1 can be written in each coordinate as follows:

$$\frac{d^2x}{dt^2} = -\frac{e}{m} B_z \times \frac{dy}{dt}, \tag{A5.2}$$

$$\frac{d^2y}{dt^2} = \frac{e}{m} \times (B_z \times \frac{dx}{dt} - B_x \times \frac{dz}{dt}), \tag{A5.3}$$

$$\frac{d^2z}{dt^2} = \frac{e}{m} \times (E_z + B_x \times \frac{dy}{dt}). \tag{A5.4}$$

If it is assumed that both the position and velocity are 0 and $d^2z/dt^2=(e\times E_z)/m$ at t=0 as an initial condition, equations A5.2 to A5.4 are solved as follows:

$$x = \frac{m}{e} \times \frac{B_x \times B_z \times E_z}{B^4} \times \left\{ \cos(\frac{e}{m} \times B \times t) - 1 \right\} + 0.5 \times \frac{e}{m} \times \frac{B_x \times B_z \times E_z}{B^2} \times t^2, \tag{A5.5}$$

$$y = \frac{B_x \times E_z}{B^2} \times \left\{ \frac{m}{e \times B} \times \sin(\frac{e}{m} \times B \times t) - t \right\}, \tag{A5.6}$$

$$z = \frac{m}{e} \times \frac{B_x{}^2 \times E_z}{B^4} \left\{ 1 - \cos(\frac{e}{m} \times B \times t) \right\} + 0.5 \times \frac{e}{m} \times \frac{B_z{}^2 \times E_z}{B^2} \times t^2. \tag{A5.7}$$

These equations give the position of an electron at given time *t*. At time t_1 for *z*=2.5 mm, the

electron reaches the AD. The shift in the *x* direction can be calculated just by setting $t = t_1$ in equation A5.5. For example, if it is assumed that the voltage between the photocathode and the AD is 8 kV, the distance between them 2.5 mm, the magnetic field 1.5 T and 30 degrees to the tube axis, then t_1 is 109 ps and the shift in the *x* direction is 1.43 mm. The shift in the *x* direction as a function of *z* is shown in Fig. 6.35.

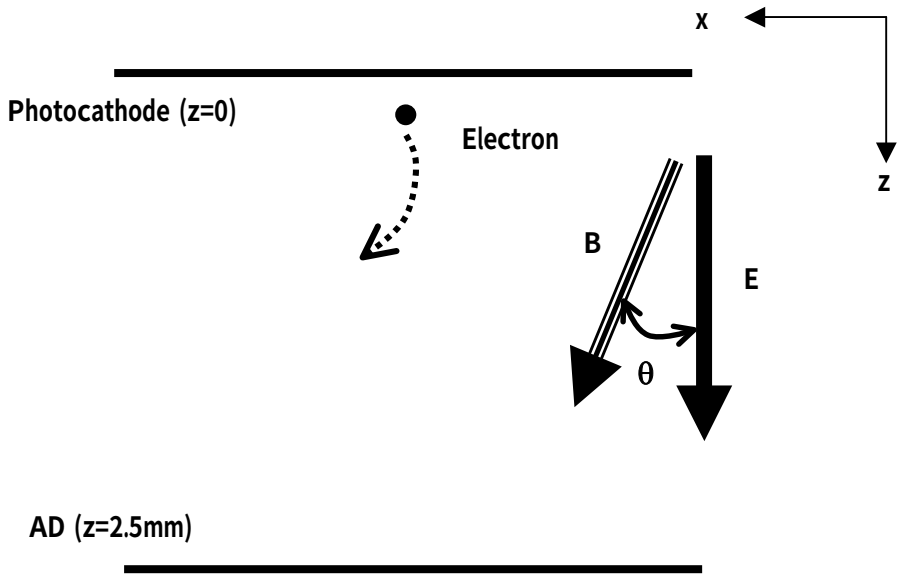

Fig. A5.1: Geometry to derive the equations for the electron trajectory in a magnetic field.